FACULTY OF SCIENCE AND TECHNOLOGY
DEPARTMENT OF GEOLOGY

Sand Waves and Sediment Transport on the SW Barents Sea Continental Slope

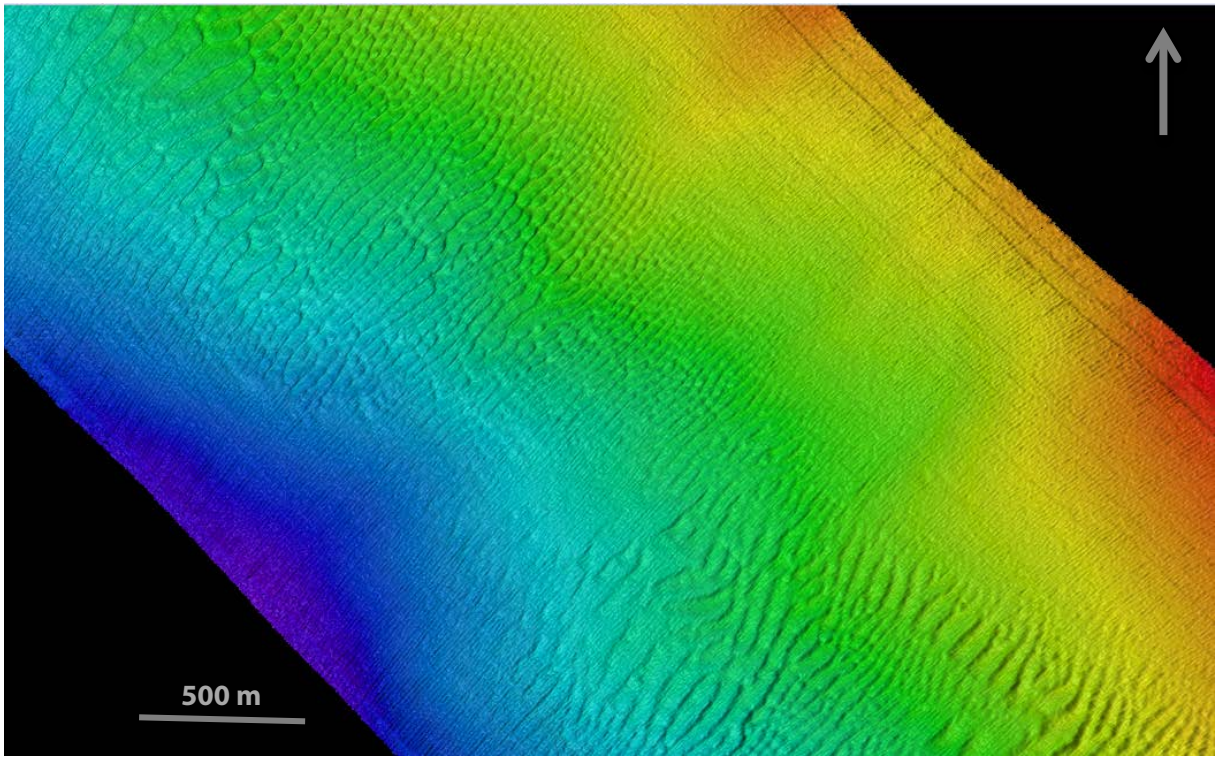

Malin Waage

GEO-3900 Master's Thesis in Geology

November, 2012

GEO-3900

MASTER'S THESIS IN GEOLOGY

Sand Waves and Sediment Transport on the SW Barents Sea Continental Slope

Malin Waage

November, 2012

Abstract

I study a sand-wave field in ~600 meters water depth on the continental slope offshore Northern Norway. Using multibeam bathymetry data from 2008 and 2011 and P-Cable high-resolution 3D seismic data from 2011, I characterize the field. Sand waves reach up to 6.6 m in height and have wavelengths as large as 140 m. They are mostly asymmetric in shape with the steepest side dipping to the northwest, indicating that current flow over the field is predominantly to the northwest. Larger sand waves (>2 m in height, >100 m wavelength) are observed on topographic highs in the sand-wave field, whereas smaller sand waves (<2 m in height, <100 m wavelength) are present in topographic lows. These topographic lows occur where three ~1-2-km-wide channels cut down the continental slope through the sand-wave field. Seismic data reveal that there are no buried sand waves beneath the seafloor, suggesting that the sand waves are being continually eroded and redeposit at the seabed.

Seismic data reveal that the depositional environment over the last ~1 Ma has been largely controlled by debris flows during the glaciations and melt-water plumes and channel formation during the glaciations. High-resolution imaging of the first few meters below the seabed shows that winnowing and associated sand-wave migration is currently the dominant sedimentary process. Data across the study area show that there are no buried sand waves beneath the seafloor. This suggests that the sand waves are being continually eroded and redeposited at the seabed.

By measuring the offset of the crest of sand waves in the 2008 and 2011 bathymetry data, I calculate that sand waves migrate from 0 to 3.3 m/yr and have an average migration rate of 1.6 m/yr to the northwest. This migration direction which I directly observe in the bathymetry data is in agreement with the migration direction that I infer from the asymmetry of the sand waves. Integrating these migration rates over the cross section of the sand-wave field, I estimate that sand is transported along the continental slope at a rate of 22.3-118x10^6 m^3/yr.

These results provide hard constraints for numerical sand-wave migration models trying to identify the link between ocean currents and sand-wave migration. Furthermore, I show that sand-wave migration has the potential to rapidly move large volumes of sand across the deep water. This movement of sand can complicate drilling and production procedures in the energy industry and may affect slope stability on continental margins around the world.

Νοῦς ὑγιὴς ἐν σώματι ὑγιεῖ.

A sound mind in a sound body.

Thales, 600 BC

Acknowledgements

Det er mange som fortener takk og en god klem for å ha både motivert meg, hold humøret mitt oppe og hjulpet meg underveis med både språk, faglig vegleidning og tekniske problema.

Handledarane mine, Stefan Bünz og Jürgen Mienert, har gjedd meg moglegheita til å få ei interessant oppgåve, motivert meg undervegs og gjedd meg nødvendig og god vegleidning no på slutten mens de trongst. Samtidig har dei gjett meg spelerom og fridom for egen utfolding og utforming av oppgåva, noko eg trur eg har lært mykje av. Sergey Polyanov har stått for prosesseringa av dataene, som viste seg å vera ein langtekkelig prosess.

Å delta på sand bølgje-møta i Tromsø har også gjett meg mogeligheit til å være ein del av det aktive forskings-miljøet på temaet I Norge og eg har fått sjanse til å diskutere meg andre dyktige forskarar på ulike fag-felt i relevans til sand bølgjer. Blant anna har eg vert i diskusjon med Jofrid Skardhamar som også gjett meg tilgang til upubliserte strøm-data over området.

Andrew Smith, Liselott Wilin og Jaap Rijckevorsel har bistått med gjennomlesing og retting av engelsk i oppgåva. Andrew Smith, fortener en ekstra takk som har brukt uendelig mange timer på å rette engelsk. Færre og færre språk feil blei gjort naturlig nok gjort etter kvart, og han har også på den måten også hjelpt meg og forbetra dei engelsk språklege kunnskapane mine!

Sjølv om eg ofte har sotte einsam på bøttekottet i seine kveldstimar og helger, har det vert morosamt og hatt Torgeir og Julie rundt seg som også har levert masteren no. Frustrasjonar, diskusjonar og glade stunder er blitt delt oss i mellom. Elles skal også mine tidlegere kontor-kamerater David, Kenneth og noverande Espen ha ein spesiell takk; me har hatt ei kjekk tid på bøttekottet! Og elles alle tidlegare og noverande studentar på blå-brakka som har gjort det til ein kjekk plass og vera i pausane!

Elles har eg mange gode venner her i Tromsø og familie i Samnanger som har støtta, motivert meg og gjort tilværinga mi elles lys og livlig! Eg vil spesielt nemne Liselott Wilin, Carine Johansen, Camilla Heggøy, Anita Finne, Ole Mathis Hætta, Marte Gaupholm Samnøy, Mamma, Pappa og søstera mi Melissa. Takk for at dykk er til!!

No gleder eg meg til å komme ut i arbeidslivet og få utfordra meg på nye plan. Eit godt støtte-team bak seg, en positiv sinnstilling og gode opplevingar undervegs må være oppskrifta til suksess både på fritida og i arbeidslivet. Eg kan ikkje vente med å finne ut kva livet har å by i neste etappe!

Malin Waage

Tromsø, november 2012

Table of Contents

Chapter 1- Introduction of thesis

1. 1. Objectives

The overall aim of this thesis is to obtain a better understanding of the occurrence of sand waves and sediment transport processes on the upper continental slope of the south-western Barents Sea. The specific objectives of this thesis associated with this aim are:

The main objectives in this thesis have been:

- Map the 3D architecture, areal distribution and varying characteristics of the sand waves on the seabed
- Quantify the variability of geometric properties as sand wave length, sand wave height, steepness and sand-wave asymmetry
- Compare the geometric variability and areal extent of sand waves with factors that may control it, such as, local bathymetry, water depth, current regime, grain-size and migration of sand waves.
- Understand the subsurface setting and depositional environment
- Investigate possible occurrence of relict sand wave horizons in the subsurface deposited during previous interglacial times

1.2 Importance of sand waves

Sand waves are of interest as they are representing a direct link to the bottom-current regime in water masses. They are also of special importance as the can cause problems concerning seafloor installations such as pipelines and cables (Morelissen et al., 2003, Németh et al., 2002). Buried pipelines and cables can that way be exposed with time and cause slack, or breakage due to dredging. In head of planning installations over such field it is important to know the nature of the sand waves and thickness of the mobile sediment layer. Continuously monitoring and echo sounding can often be essential above such dynamic sand fields (Németh et al., 2002, Nemeth, 2003).

1.3 Project Affiliation

This study was carried out between September 2011 and November 2012. The project has been supported and partly funded by the Norwegian Deepwater Programme within the Seabed Project. The project is also associated with the MAREANO Programme, a co-operation between NGU, the marine research institute and others to gain more knowledge about the seabed on the Norwegian Continental Shelf.

High-resolution P-cable three- dimensional seismic data and multibeam echosounder data has been collected by the University of Tromsø in July 2011 and was used in this work for detailed study of the sand waves and the stratigraphy beneath them.

1.4 Structure of the thesis

The thesis is divided into eight chapters. The first chapter is a short preface where the main objectives, project affiliation and the structure of the thesis are presented. An introduction to the project, basics of sand waves and sedimentary processes active on continental slopes and oceanography (physical settings) will be given in the second chapter. In the third chapter, the study area is presented, including geology, geomorphology and ocean current regime. Data, methods and tools for the work are described in the chapter four. In chapter five the results are presented. Chapter six compares and discusses the quality and resolution of the different data sets, while chapter seven provides the main discussions. Finally, conclusions of the study are drawn in chapter eight.

The thesis is generally divided into two parts: the seabed and the sand wave geometry on the seabed based on bathymetry data and the shallow seismic stratigraphy beneath the seabed based on the interpretation of high-resolution 3D seismic data.

1.5 Introduction of thesis

Scientists have studied sand waves since the 1930s. Sandy seabeds are often characterized by dynamic bedforms of different spatial scale as sand waves, ripples, mega-ripples and sandbanks (van Dijk et al., 2008). In accordance with terminology from Belderson et al. (1982), sand waves are defined as subaqueous, lower flow regime, transverse bed forms of sand with larger wavelength than ripples.

The classification of sand waves by size is not consistent among different sources. Ashley (1990) claims sand waves are rhythmic bedforms with wavelength of 100 – 1000 meters and wave-height between 0, 5 and 18 meters. Nemeth et al. (2003) on the other hand present the classification listed in figure 1.1, which gives a good indication of the relative size according to time of development of the bedforms. However, Allen (1980), Amos and King (1984), and Ashley (1990) states that where several sizes of sand waves occur together it should be convenient to refer to them all as sand waves, in categories of small sand waves and large sand waves, since the genetics behind them likely are the same.

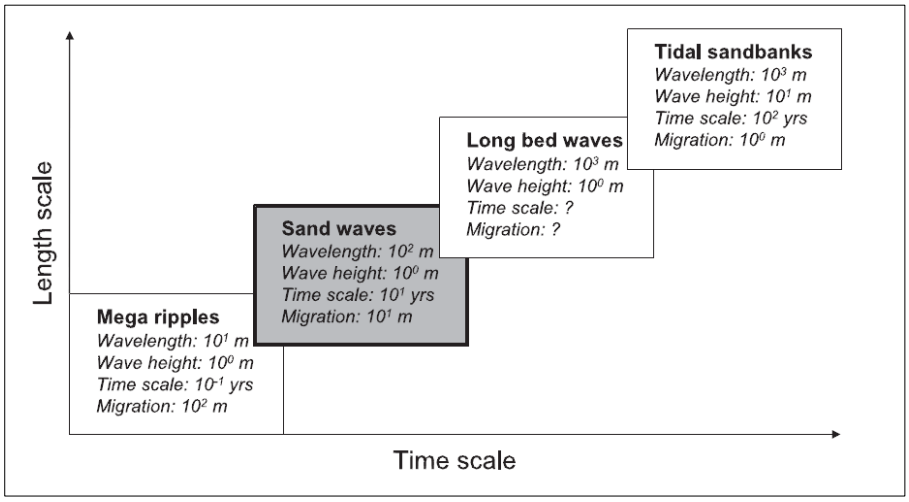

Figure 1.1: Nomenclature of Ripples, sand waves, and sandbanks (Nemeth, 2003)

Sand waves are common on the seabed worldwide and are providing important information about the strength and directions of bottom currents e.g. (Kenyon, 1986). Sand waves are also of special interest as they can cause problems concerning navigation and sea-bottom installation due to their dynamic behaviour. Buried pipelines can be exposed and damaged by dredging (Morelissen et al., 2003). In areas where sand waves are present it is therefore important to gain knowledge about their dynamic behaviour before planning installations on the seabed. Many experimental models show how sand waves develop over time. Huschler et al. (2001) presented a numerical model that showed good agreement with real observations. The model was based on morphological patterns versus different physical parameters such as water level, tidal velocity amplitude, and viscosity of water.

Sand waves are common structures in tide-dominated seas and seaways, for example the seas around the British Isles (VanVeen, 1938), Calais-Dover Strait (Besio et al., 2008) , and the North Sea (Caston, 1972, Houbolt, 1968, McCave, 1971, Dingle, 1965). Although they are less common in open shelf waters and slopes where the tidal currents are weak, there are a few examples of deep-water sand waves in the Argentine Basin (Flood and Shor, 1988), the Northern Bearing Sea (Field et al., 1981), Gulf of Gadiz, NE Atlantic (Habgood et al., 2003) and the Hola Trough, outside Vesterålen (Bøe et al., 2009b). The sand-wave fields along the continental slope of the South-Western Barents Sea are located in water-depths between 470 and 750 meter. Two major sand-wave fields are located along the continental slope. The northern- most field (N-2) (located between 550 – 650 m.b.s.l) are studied in this thesis. Location of the field and video-transects of sand waves are illustrated in figure 1.2 and 1.3.

The main topic of this master thesis concerns the superimposed sand waves in the study area; therefore, a natural focus for the P-Cable 3D seismic data has been the seismic expression of the sand waves, potential identification of internal structures and buried relict sand waves, locating the base of the exposed sand layer and defining the depositional environment before formation of sand waves. The detailed study of slope sediments deposited during middle – late Pleistocene time on the Barents Sea Continental Slope was conducted in 1996 (Laberg and Vorren, 1996) by using 2D seismic sparker data along the Bear Island Trough Mouth Fan. The new (2011) P-Cable high resolution 3D seismic data set allows a unique detailed 3D study of slope sediments on the southern margin of the Bear Island Trough Mouth Fan, providing new insights on sedimentary processes in this area. Horizons within the section where interpreted as part of an attempt to localize relict sand wave structures, and to reveal interesting structures within the middle – late Pleistocene succession in the study area.

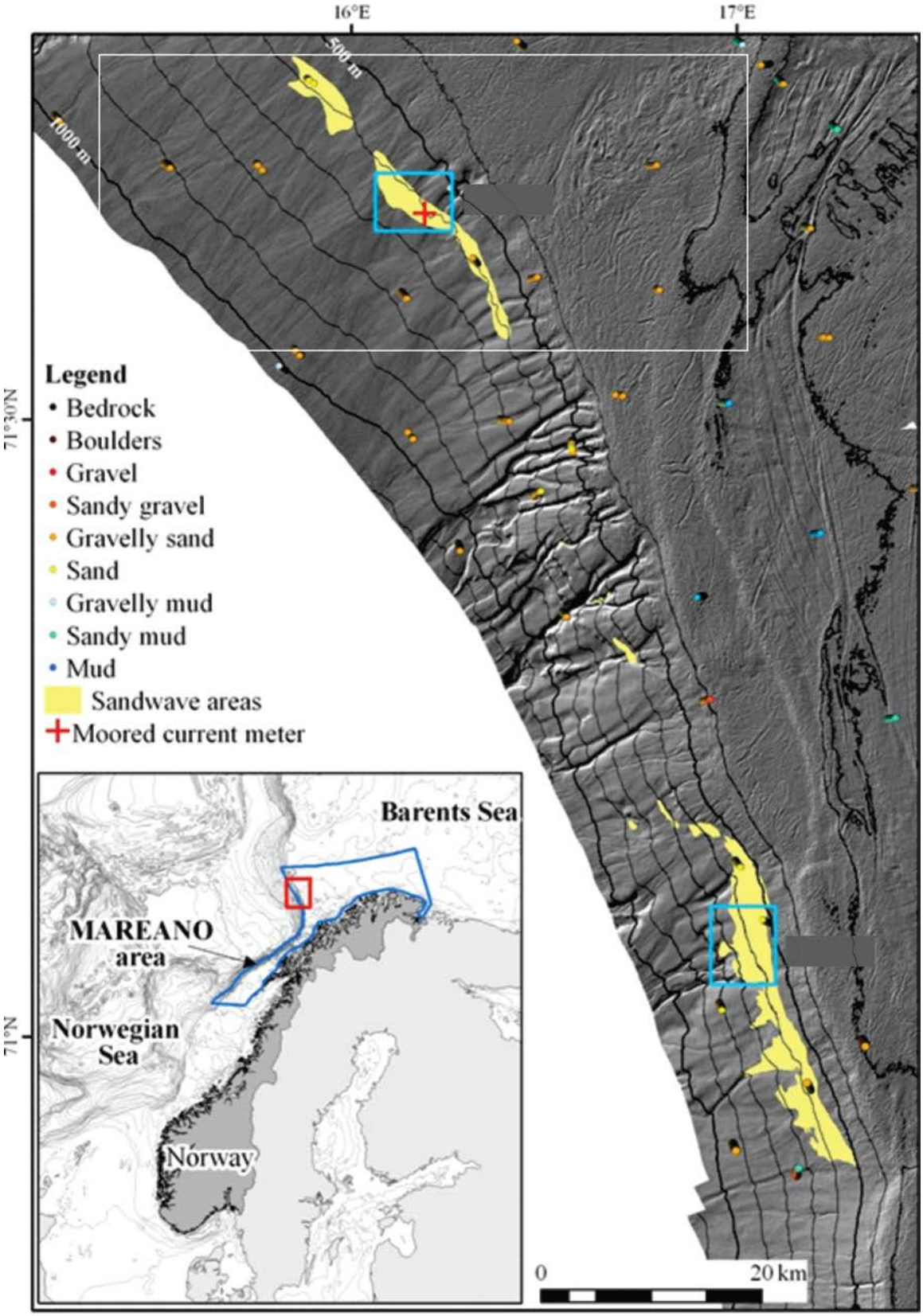

Figure 1.2: Location of the two major sand-wave fields located on the South Western Barents Sea, Continental Slope. The northernmost field is studied in this thesis. Figure modified from King (not publ.).

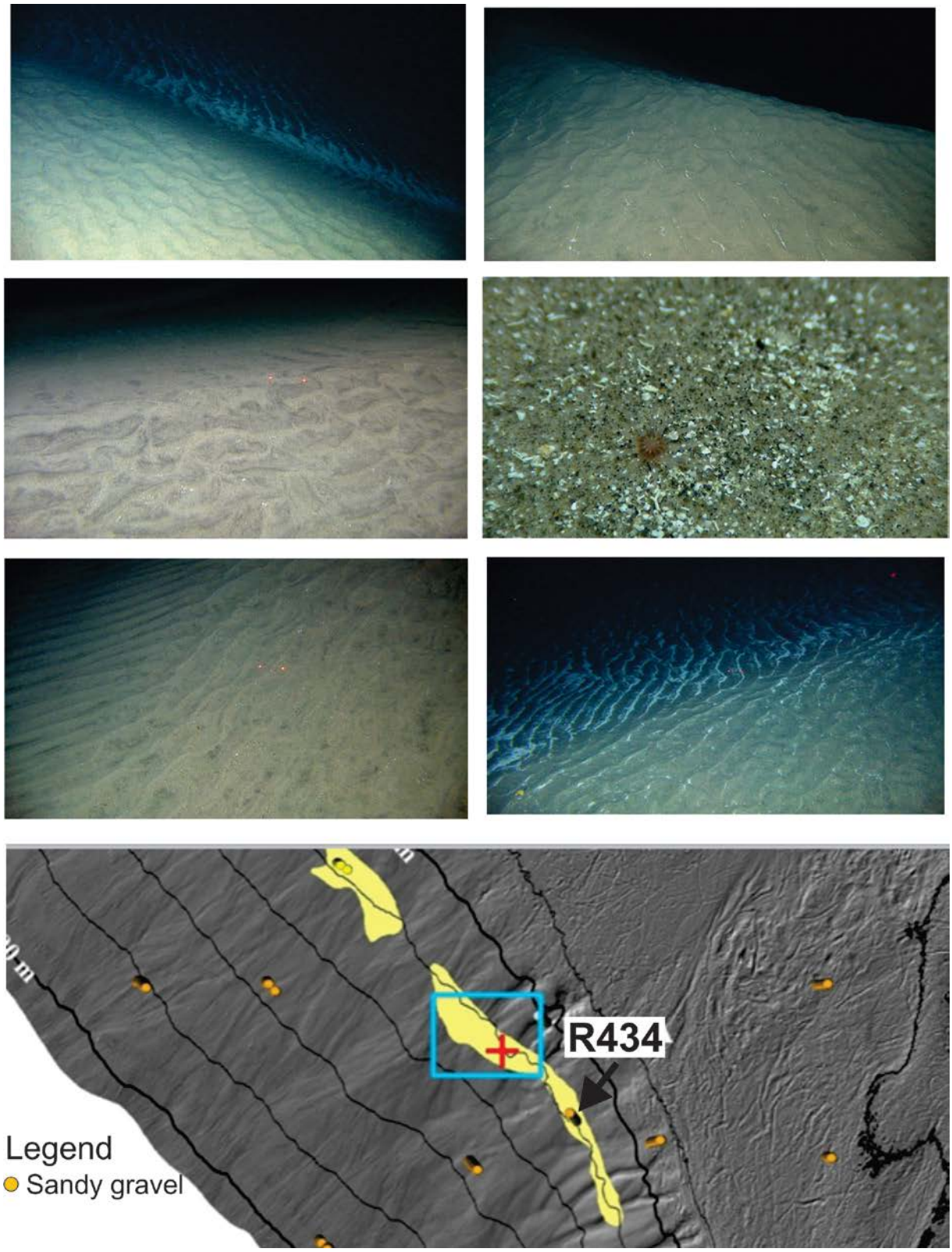

Figure 1.3: Video transects of area R434, indicated with an orange dot in the shaded bathymetric map. The video transects confirms a sandy gravel grain size in the sand-wave field. The video transects are gathered by NGU in 2008.

Chapter 2 - Basics of Sand waves and Continental Slope processes

2.1 Formation of sand waves

Mud, - sand, - or gravel waves, in addition to ripples and dunes are all elongated ridges forming perpendicular to the current direction. The type of bedform that evolves on the seabed is mainly a function of current strength, water depth, and grain-size (fig. 2.1). Sand waves can be generated by flow velocities of ~0.4-0.9 meter per second if enough sand is available (0.2-2.1 mm grain size), as seen in figure 2.1. Smaller current velocities will create ripples (linguid) while stronger current velocities create along-current structures such as barchans dunes. A smaller median grain size will generate ripples, whereas a larger grain size may create occasional scours (Stow et al., 2008).

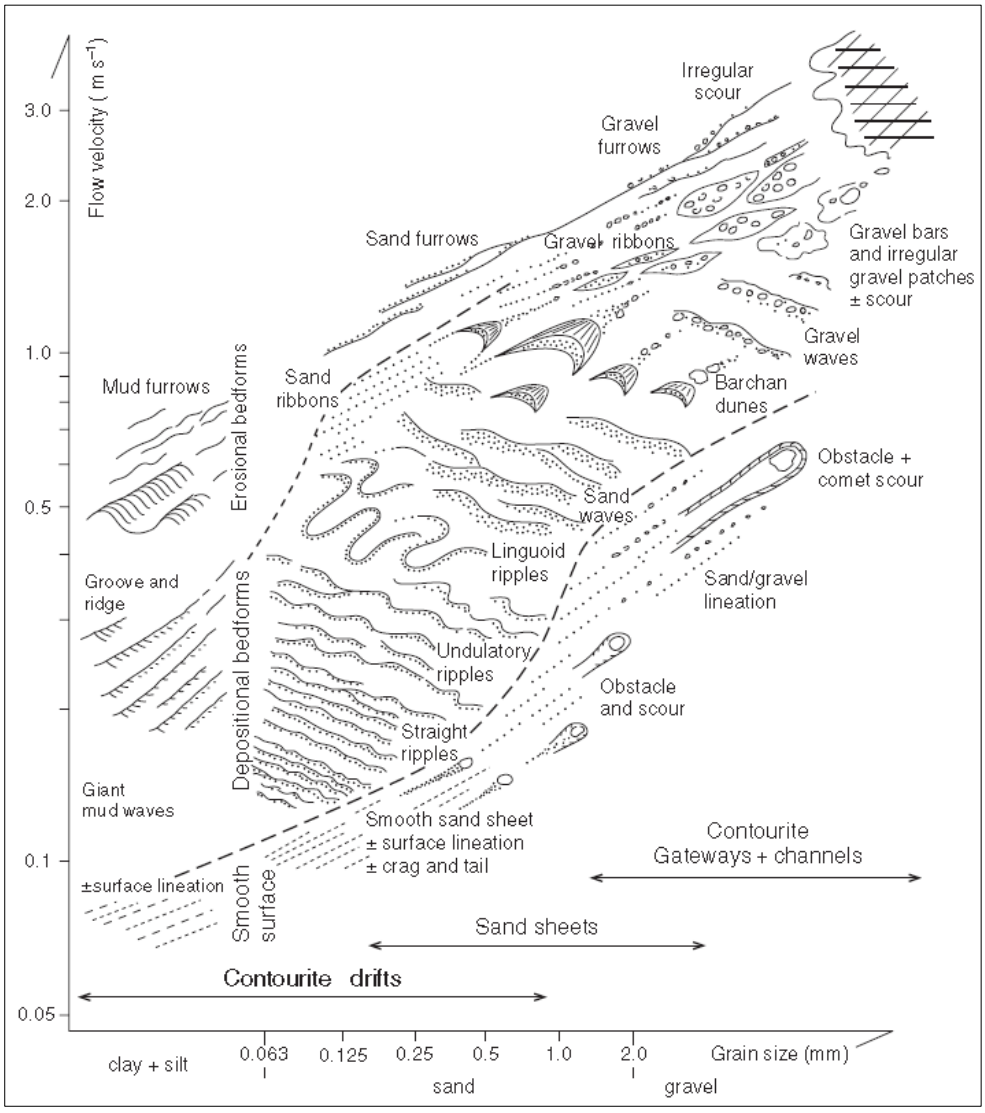

Figure 2.1: Schematic distribution of bedforms as a function of flow velocity and grain size. Figure from Stow et al., 2008.

Allen (1965) describes how sand grains move across a typical sand wave; the sand particles propagate upslope the stoss side of a sand wave, where the current velocity allows the sand to move. Crossing the crest, the current velocity drops, and the sand grains accumulate at the steeper leeside, either by avalanching or from settling by suspension down the lee-face. Coarser grains settle closer to the crest top while finer grains become deposited towards the toe. Erosion also tend to occur on the stoss side upstream, - a reason why the top of the stoss-face is rarely preserved on sand waves. Figure 2.2 presents the process.

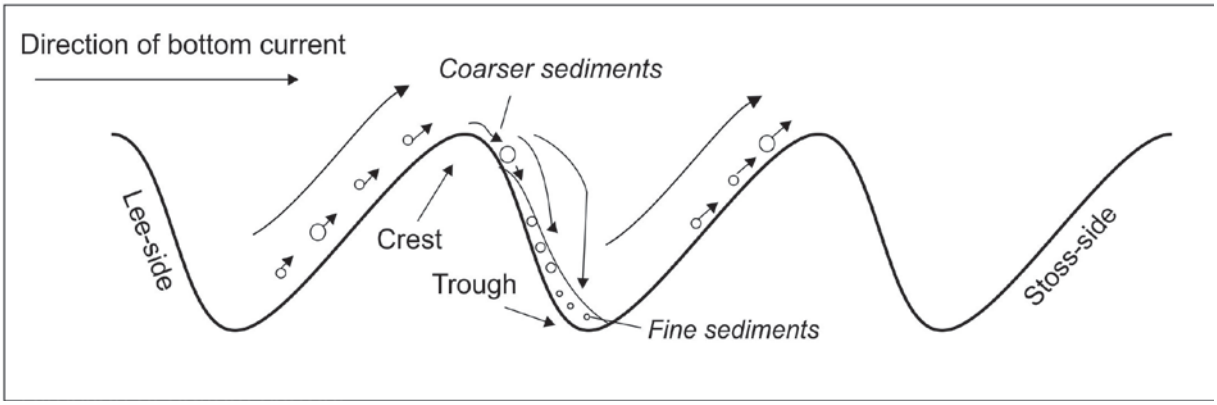

Figure 2.2: Settling of sandgrains on lee-slopes. The figure is modified from Allen (1965)

2.2 Definition of geometric properties of sand waves

Geometric properties such as wave-length, wave-heights, crest-length, dip on the lee and stoss-sides, and asymmetry of the waves are defined in this subchapter. These properties can vary largely within a sand-wave field and from field to field. Water depth and current velocity seem to be the most important factor influencing sand wave geometry (Sterilini et al., 2009), but sand wave geometry properties may also provide information about the current direction, migration rate and thickness of the sand layer. As mentioned in the introduction, sand waves can vary in wavelength from tens to hundreds of meters, and grow up to 25 meters in height. In shallow seas the water depth is the main controlling factor of wave height, since waves cannot be greater than 30% of the water depth (Allen, 1980, Hulscher, 1996). In deeper water, sand waves can potentially grow tens of meters. The height becomes a function of other factors such as grain size, wavelength and sand wave formation time. Figure 2.3 show the sand wave geometry terms used in this thesis, and will further be discussed in the next part. The terms and equations used during this work is from the work of (Knaapen, 2005).

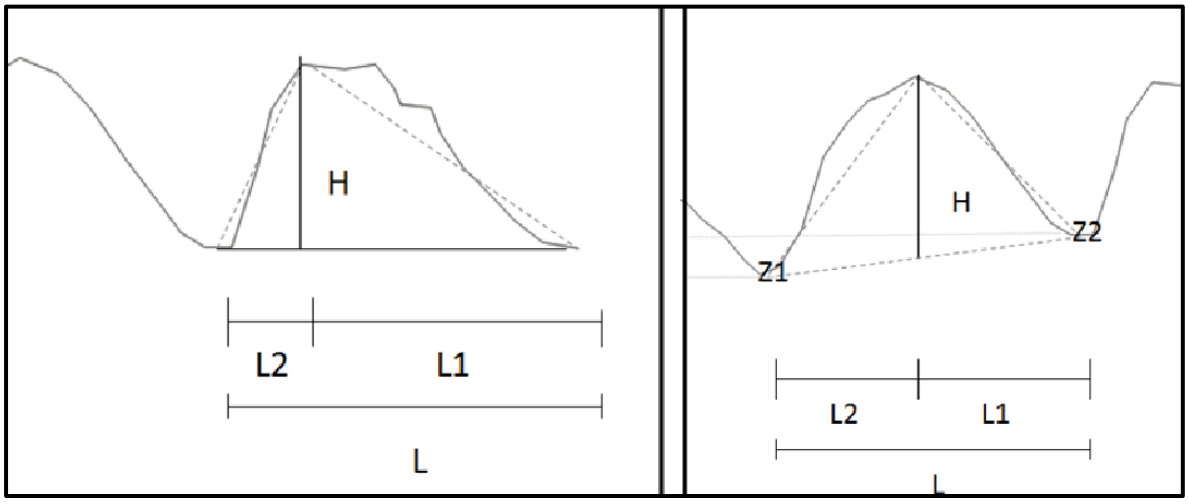

Figur 2.3: Two principal sand wave examples with the terms used in this thesis; H = wave-height, L = wavelength, L2 = length of lee-side, L1 = length of stoss-side, Z1 and Z2 = the different crest levels.

The difference between the crest levels (Zcrest) and the neighbouring trough levels (Z1,Z2) is defined as the **wave height (H)**;

$$H = Zcrest - (Z1L2 + Z2L1)/L \quad \text{(eq. 1)}$$

The equation describes an envelope from the linear interpolation between the crest and the neighbouring trough levels.

The wavelength (L) of sand waves is the horizontal distance between the trough positions on both sides of the crest:

$$L = Zcrest - (Z1L2 + Z2L1)/H = Z2x - Z1x \quad \text{(eq. 2)}$$

Experiments and observations have shown a distinct connection between wave height and wavelength for shallow water sand waves by formula of Flemming (1988):

$$H=0.0677L^{0.8098}$$

Crests of sand waves are commonly slightly sinuous to straight.

The dip of sand waves can vary depending on height, flow regime and grain size. The structures mostly have an asymmetric shape, with the steepest side oriented with the residual current direction (Houbolt, 1968, Cloet, 1963, Caston, 1972). A symmetric shape is indicating the same current strengths in both directions. **The lee-stoss asymmetry** of a sand wave can be expressed by;

$$A = (L1 - L2)/L \quad \text{(eq. 3)}$$

Where L1 is the horizontal distance between the crest and neighbouring trough south of the crest and L2 is the distance between the crest and trough north of the crest. A perfectly symmetric wave, where L1 = L2, gives an asymmetry value of 0. A negative asymmetry value indicates a reversed symmetry, where the lee side, defined after the regional migration direction, is the steepest side of the crest (Knaapen, 2005). When sand waves seem to migrate opposite to the asymmetrical shape, it is called reversed sand-wave migration (Van Landeghem et al., 2012). Furthermore, sand waves are assumed to grow larger and more asymmetric in shape with increasing velocity and time (Allen, 1980).

2.3 Sedimentary processes on continental slopes related to glacial margins

This subchapter is an overview of the processes leading to the erosion, deposition, and redistribution of sediments on the slope of a passive continental margin.

Continental slopes are defined as the seaward border of continental shelves, by origin located on the transition between continental crust and oceanic crust at ocean margins. Glaciations modify the continental shelves and cause advance of margins, creating hundreds of km of broad continental shelves. The Norwegian continental shelf is one of the broadest in the world, which makes it far from discrete sources of sediment supply.

Continental slopes are relatively steep (~4*) and often interspersed with canyons and mounds. They border the less steep continental shelves (~0,005*) landwards and the continental rises (~1*) seawards. The steepness of continental slopes gives rise to redistribution of sediments, which occurs via **down-slope processes (1)** such as submarine slides, slumps, debris flows, and turbidites(Pinet, 2009). Ocean currents tend to flow along continental slopes, causing erosion, transport, and deposition of sediments along the slope(Pinet, 2009). These processes are known as **along-slope processes (2)**. Along-slope processes and down-slope processes can either be constructive in that they contribute to building out the margin or destructive in that they redistribute sediments already on the slope. The last main process causing sedimentation on continental slopes is the settling of fine-grained material from the water column, called **vertical flux (3)** (Pinet, 2009).

2.3.1. Down-slope processes

High sedimentation rates and build-up of excess pore pressure is one of the main mechanism behind release of slides and other gravity flow related processes on the continental slopes (Vorren et al., 1989). Through mouth fans, gullies, channels, slide scars, and corresponding accumulations are the main large-scale morphological elements on continental slopes (Vorren et al., 1989, Vorren et al., 1978). Downslope processes on continental slopes are normally more active in the canyons and channels (Yoon et al., 1991); that might have formed by cold water currents from nearby ice caps during glacial periods (Bugge, 1983) or by the flow of cold dense water during interglacial periods (Vorren et al., 1989).

Debris flows, turbidity currents, slumps, slides, melt-water plumes, and streams are typical processes active on continental slopes during maximum glaciations e.g. (Vorren et al., 1989, Lucchi et al., 2002, Vorren, 2003). The melt-water plumes appear when the ice cover melts, often in an early stage of a deglaciation. Glacigenic debris flow is especially related to maximum glaciations. The features are also said to be the Trough Mouth Fan building blocks (TMF) (Rise et al., 2005) , - characterized as lense-shaped fans up to 100s of km-wide that are deposited at the base of channels or canyons

(Laberg and Vorren, 1996). In seismic data, such lenses can be separated by high-amplitude reflections, which distinguish them from periods of low sediment input and erosion during interglacial times (Vorren, 2003). An example of a large TMF, about 400 km wide, is the Bear Island TMF located at the base of the Bear Island Trough (BIT) (Laberg and Vorren, 1996). Figure 2.4 is a figure from Vorren et al., (1989), presenting the main down-slope processes on continental margins during glacial and interglacial periods.

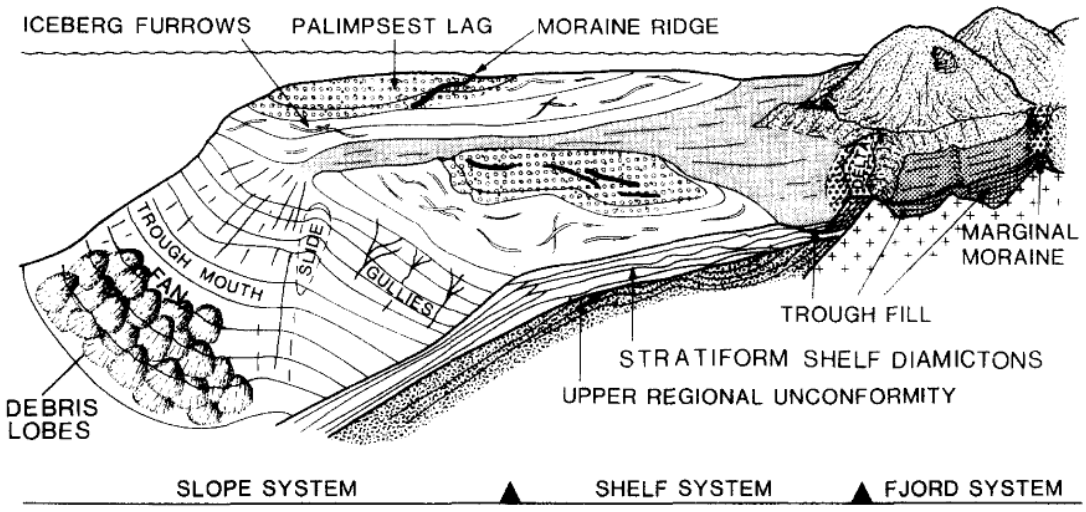

Figure 2.4: The model shows the main glacigenic morphological elements and downslope processes on the passive continental margin of northern Norway (Vorren et al., 1989)

2.3.2 Along-slope processes

The mechanisms behind the along-slope processes on the continental slopes are water mass flow and circulation on the seafloor. In high latitudes, seafloor topography significantly affects currents, often forcing water masses to propagate parallel to bathymetric contours along the shelf break of continental shelves (Rumohr et al., 2001). Finer sediment tends to be eroded and transported away by currents, while coarser material stays in place. Deposits of such along-slope processes are mud and sand drifts, conturites, and sand waves. Contourites and sediment drifts are often made up of fine-grained mud and are structure-less; while sand waves often have cross-bedded internal structures. The distribution of the different deposits is determined by bathymetry, current strength, type and amount of sediment available. Commonly, the along-slope deposits are more sorted than deposits of the down-slope processes.

2.4 Oceanic currents related to sand wave formation

Oceanic currents are continuous and directed movement of water generated and controlled by forces such as tides, breaking waves, wind, coriolies force, and density differences (Pinet, 2009).

Surface based movement of water as tidal currents, storm induced currents and geostrophic currents exert the conditions of regional flow velocities of 0.4 to 0.9 meters per second. **Deep-water currents (termohaline circulation)** are currents driven by density differences caused by variations in salinity and temperature of the water masses (Pinet, 2009). These currents originate in the cold arctic and Antarctic and flow North and South along the bottom of the world oceans (Pinet, 2009). Deep-water circulation is however a slow process (Pinet, 2009), as such; it is unlikely that these currents transport sandy sediments.

S**urface currents** are mainly dependent on temperature and wind (Pinet, 2009). Large-scale geostrophic surface currents are flowing in gyres, caused by the large-scale wind system, coriolies force and the distribution of continents. The continental shelf outside Norway is located on the northern corner of the westerly wind belt where strong and deep surface water moves northwards across the continental slope as the North-Atlantic Current (NAC) (Pinet, 2009).

Sand waves are often explained as a result of strong tidal currents. The rise and fall of **tides**, which creates tidal currents, are driven by gravitational attractions between the sun and moon on the Earth. Tidal currents are especially strong in the macro-tidal environments, such as on high latitudes, and where the water level is low or the cross-sectional area of flow is small, as in shallow oceans, near the coastlines, inlets, straits and estuaries along the coast (Allen, 1980).

Internal tides or waves are underwater waves that pulsate with the period of a tide up and down between the continental slope and halocline. Experiments have shown that they can cause erosion of the slope and also sediment movement upslope (Cacchione and Drake, 1986).

2.5 Occurrence of Sand waves

Since sand waves mostly originate from various types of surface currents, sand waves may occur in relatively shallow water (30-40 m); as in coastal environments, shallow seas and along continental margins (Stride and Stride, 1982). Large parts of the North Sea are for example covered by sand waves (Németh et al., 2002). Shallow water sand waves also occur for example around the British Isles (Kenyon, 1970), in the San Francisco Bay (Sterilini et al., 2009, Gibson, 1951), and number of other places.

In deeper water, sand waves commonly occur in settings where water masses flow through a smaller cross-sectional area due to the higher flow velocity through these areas (Jarrett, 1976). Excellent examples of such morphological features exist in the Argentine Basin (Flood and Shor, 1988). Internal-wave currents is suggested to be the most reasonable mechanism behind formation of the up-slope asymmetric sand waves at 175 – 490 m depth (Karl, 1986). A deep water example is the sand-wave fields in the Gulf of Cadiz, North Eastern Atlantic that occur in ~700-875 meters depth in channels along the continental slope (Habgood et al., 2003). Habgood et al., (2003) shows evidence of sand-wave migration down the channels as a cause of downslope thermo-haline bottom currents and contourites by the salty Mediterranean water.

Kenyon and Stride (1968) were one of the first to report sand waves in open deep water (200-800 meters); along the upper continental slope west of Scotland and Northern Norway by use of side-scan sonar. Newer studies by Bøe et al. (2009) reveal sand waves in water depths of 200 – 260 meters in the Hola Trough, outside Vesterålen, while this study and the ongoing Mareano project focus on sand-wave fields along the Continental Slope of the SW Barents Sea. The main mechanism behind these sand waves is assumed to be a complex current regime on the bottom by a combination of geostrophic surface currents, tidal forces and internal tides (Bøe et al., 2009b). Large subaqueous sand dunes (amplitude exceeding 16 meters, and wavelengths exceeding 350 meters) have also been reported in open water along the upper continental slope in the South China Sea (in water depths between 160 – 600 meters), indicated to be a cause of internal waves (Reeder et al., 2011).

2.6 Prediction models of sand waves

Huschler and Brink (2001) provided a prediction model of regular morphological patterns on the seafloor tested with observations of variation in sand waves and sandbanks appearance. The model presented by Huschler (1996) supported on underlying hypothesis that large-scale bed features are free instabilities of the morphodynamic system. The results showed that the most important factor of occurrence of sand waves seemed to be water depth. With use of variable depth, they were able to predict the contours where sand waves would be expected.

Sterilini et al., (2009) did a similar case study in Golden Gate, San Francisco Bay. Previous numerical models based on stability analyses where used in the modeling from the work of Huschler and Van den Brink, 2001; Besio et al., 2003a, 2004 and Van der Ven et al., 2006. The current strength and water depth seem both to be the most important factors controlling sand wave characteristics. Knappen (2005) also show how sand wave height correlates with water-depth and local bathymetry in a sand-wave field in the North Sea.

Oyen and Blondeux (2009) on the other hand, studied the variation in sand waves characteristics on a heterogenic grain size distributed seabed based on flow-topography interactions in the North Sea. By developing a local model, they found some interesting results; - a finer mean grain size on the seafloor would create longer sediment wavelengths than a coarser mean grain size on the seabed. This variation was evidently strongly affected by graded sorting of the sediment waves.

Chapter 3 - Study Area

3.1 The Barents Sea

The study area is located on the continental slope of the South-Western Barents Sea. The Barents Sea is a shallow epicontinental sea with an average depth of 230 meter situated at the north-western part of the Eurasian Continent (fig. 3.1). The shallow shelf area connects to the Arctic Ocean to the North and Eurasia to the South, while the Norwegian Sea and the Kara Sea are to the east and west, respectively.

The Barents Sea has been an area of exploration for as long as there have been Arctic expeditions, going back as far as the research expeditions of William Barents in the 16th century and Fritjof Nansen in the 1880s. Nansen contributed important information concerning sea current directions. He was also the first researcher to suggest that the South Western Barents Sea had experienced late Tertiary uplift and erosion, based on bathymetry data and existing geological information of surrounding land areas. A Russian marine geologist named Maria Klenova in 1933 completed the first full seabed map. In 1970, oil and gas exploration started in the Barents Sea. Since then, more and more detailed maps of the seabed and the stratigraphy beneath the Barents Sea have been processed. The extensive mapping programme Mareano by NGU has been going on since 2005 (Buhl-Mortensen et al., 2010). One of the goals of the program is to understand if there is an ecological and/or biological imbalance in the Barents Sea. The program also seeks to oversee the extraction of resources from the region while at the same time preserving the wildlife and biodiversity in the ocean. To do this, the Mareano Program has mapped the shelf and outer shelf of the SW Barents Sea and compiled detailed information about the biological life, geology, and physical conditions that are present offshore Norway (http://www.mareano.no/).

Figure 3.1: Map showing the location of the Barents Sea and the adjunct areas around.

3.2 Geological and hydro-physical setting

3.2.1 Morphological setting

The study area is located on the upper continental slope of the South Western Barents Sea in 550 to 650 meters water depth (fig. 3.2). The shelf break in the area occurs at about 400 meters depth, and the continental slope is broadly striking NNW to SSE.

The study area is located outside an earlier glaciated shelf (Vorren et al., 1989, Andreassen et al., 2004). 100 km north of the area occurs the largest glacial erosion valley in the Barents Sea, the Bear Island Trough. The trough is incising the continental slope and the outer shelf by an area of about 100 000km^2. On the continental shelf and east of the study area lies Tromsøflaket, a narrow (160 – 350 m water depth) 25 000 km^2 plateau consisting of morain sediments.

Channels, gullies, mass flows, screed deposits and glacially fed chutes in addition to moraine ridges, ploughmarks, glacial lineation's and sand waves characterize the slope and marginal shelf in the area (Buhl-Mortensen et al., 2010). The two major sand-wave fields are interrupted by a dense area of large glacial chutes and channels (fig. 3.3).

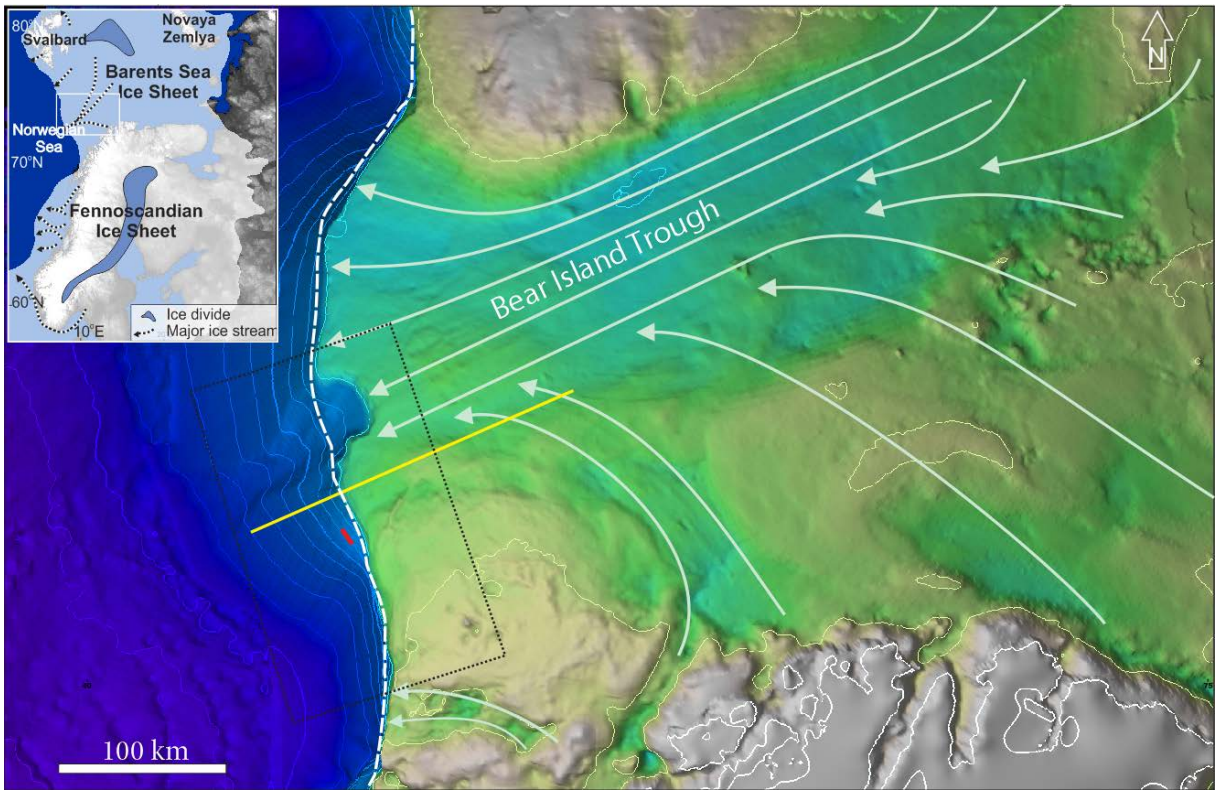

Figur 3.2: Shaded relief map of the South Western Barents Sea with the major ice stream directions indicated by the white arrows. The white stippled line indicates the location of the Fennoscandian ice sheet during max glaciations. The yellow line shows the location of the seismic cross section in figure 3.5, and the red line show the study area of this thesis. The black stippled square indicates the area of figure 3.3 showing the morphological features on the slope. Figure modified after Deryabin (2012)

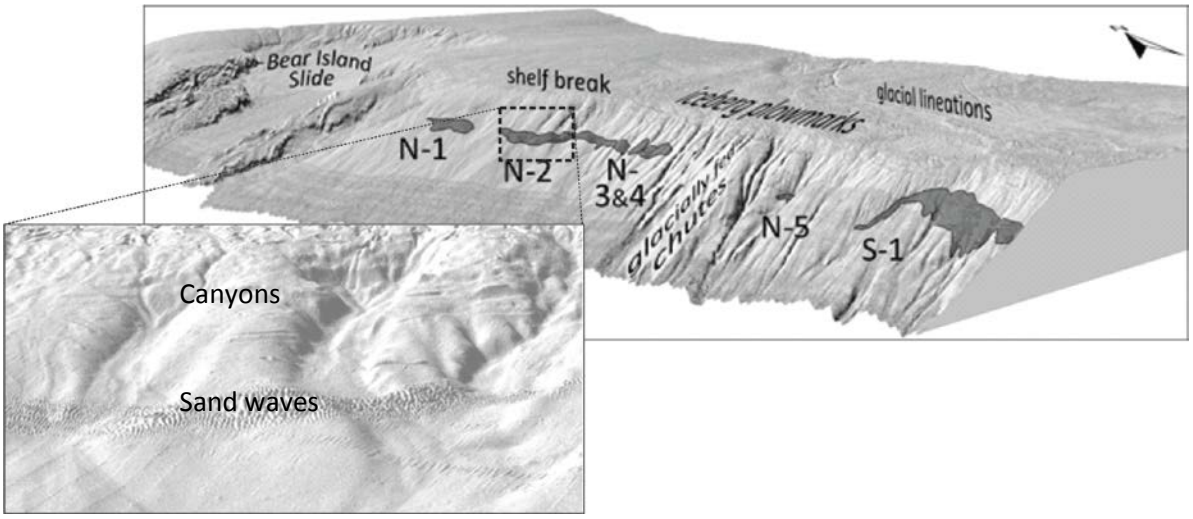

Figure 3.3: Morphological setting in the study area. The dark areas are sand-wave fields along the continental slope. The square indicates the study area of this thesis where sand waves occur on top of a channelized bed (canyons). Figure modified from King (NGU, unpbl.)

3.2.2 Hydrophysical setting on the seafloor

The shelf break and slope along the continental shelf are commonly exposed to two main oceanic currents, the North Atlantic Current (NAC) and The Norwegian Coastal Currents (NCC).

The North Atlantic Current (NAC) is a continuation of the Gulf Stream (westerly boundary current) and flows northwards along the continental slope, until it splits in two parts north of Northern Norway, south of Tromsøflaket. One branch follows the continental slope northwards towards Svalbard, while the other branch flows into the Barents Sea as the North Cape Current (NCC) (fig. 3.5). The North Atlantic Current flows in a meandering pattern, as shown in the figure below. This can cause eddies and turbulence in the water around.

Powerful currents flow between NAC and the Norwegian Coastline. These currents are called **Norwegian Coastal Currents (NCC)**. They originate as freshwater from the fjords along Norway, and subsequently sweep northwards in an edge-shaped low-salinity current. Along the way, the water masses mix with water from the North Sea, Baltic Sea, and the North Atlantic Ocean. NAC are more saline water masses than the coastal waters, and thereby the overall salinity of the mix decreases northwards. The current is mostly driven by its density difference. The topography on the bottom is an important factor for this mixing. The water flows has a tendency of following the depth contours along its way north.

Tidal currents also propagate in the same direction as the NAC and NCC and can be a contributor to current forces acting on the slope.

No detailed bottom current-map has yet been published in the sand wave area, but a 160 meters grid is in preparation by the Institute of Marine Research (IMR). IMR has analyzed current meter-data 20 meters above the seafloor in the study area, where the maximum current speed detected by the current meter was 0.4 m/s to the North and South during the two months of recording (Skagseth, pers.com). However, bottom-current modeling results show a maximum current speed of 1.2 m/s during a year period (Skardhamar, pers.com).

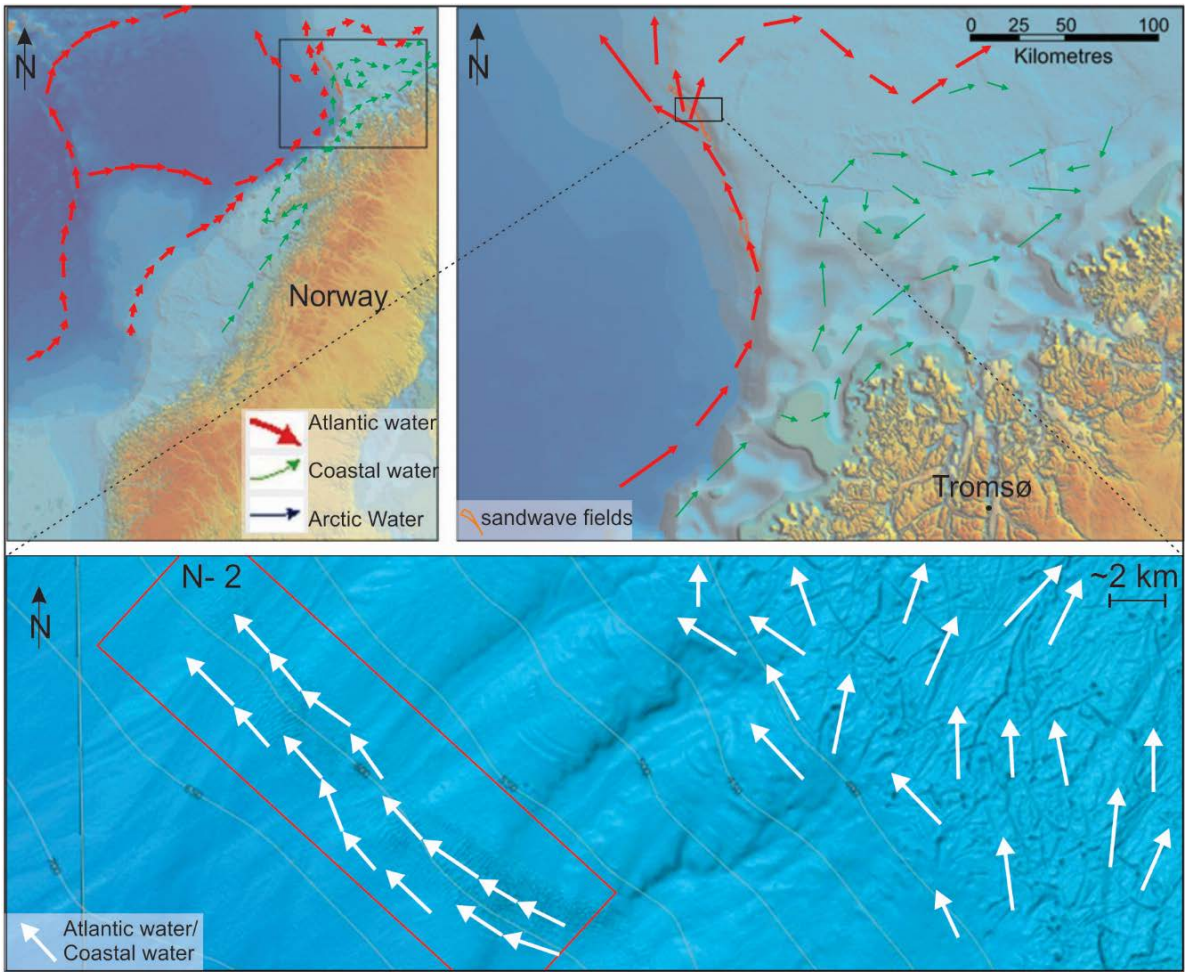

Figure 3.4: Hydrophysical conditions and related sediment type on the seabed in the South Western Barents Sea. The study area is indicated by the black square.

3.3.3 Stratigraphy

The glacigenic sequence of SW Barents Sea has been described by many authors as a sequence of several prograding units e.g. (Vorren et al., 1991, B. Rafaelsen, 2002, Sættem et al., 1994, Sættem et al., 1992, Laberg and Vorren, 1995, Faleide et al., 1996, Andreassen et al., 2004). A seismic stratigraphic framework of the western part of the Barents Sea margins has been established and modified by Faleide et al., (1996), Butt et al., (2000), Ryseth et al., (2003), Sejrup et al., (2005), Andreassen et al., (2007) and Knies et al., (2009).

The three main sequences, GI, GII and GIII and seven reflectors, R7-R1 (defined by Faleide et al. (1996)) have been described. Fig. 3.5 show a geo-seismic profile made by Deryabin (2012) based on such previous interpretation. The deepest reflector, R7, marks the base of the glacigenic deposits, and is estimated to be 2,3-2,5 Ma (Sættem et al., 1992, 1994; Eidvin et al., 1993; Mørk and Duncan, 1993; Channell et al., 1999; Eidvin and Nagy, 1999; Smelror, 1999; Butt et al., 2000). The base of the GII unit, represented by reflector R5 is estimated to be 1,3-1,5 Ma based on biostratigraphic and Sr. data (Butt et al., 2000) and is interpreted to represent a hiatus as a result of erosion due to increased glacial activity on the shelf (Faleide et al., 1996). Different ages have been suggested for the R1 reflector, the base of unit GIII. Vorren et al., (1990) concludes an age of 0.8 Ma, Sættem et al., (1992) and Faleide et al., (1996) indicates an age of 0.44 Ma, while one of the latest reconstruction indicates an age of 0.2 Ma (Knies et al., 2009). The reflector (R1) represents the upper regional unconformity (URU). An overview of a correlation of sequences and the different nomenclature along the South Western Barents Sea is also presented in table 1.

Previous regional mapping together with well data (Ryseth et al., 2003; thereafter modified by Andreassen et al., 2004 and Deryabin, 2012), indicate that the middle-late Pleistocene succession of the study area is located approximatly 1500 ms TWT below sealevel (~600 m below seabed assuming an acoustic water velocity of 1500 m/s and an acoustic sediment velocity of 2000 m/s). Since the interpreted seismic section of the SandWaveNorth_3D survey also exists within the uppermost ~1500 (*400 m* below seabed assuming the same velocities) it is assumed that the study area is located within the GIII unit.

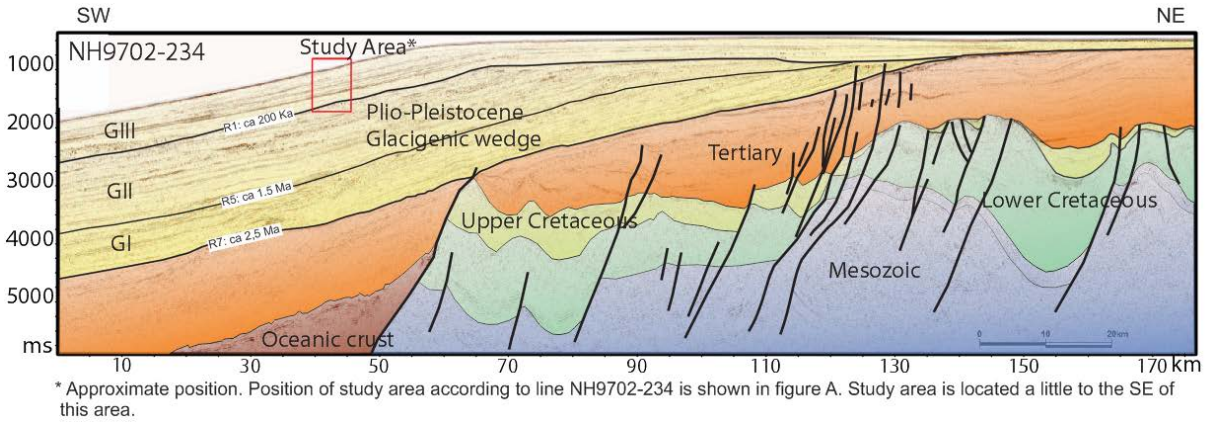

Figure 3.5: The figure shows a geo-seismic profile of across the Southwestern Barents Sea based on the 2D seismic line NH9702-234. The reflectors are regionally correlated within the glacigenic wedge. The red rectangle indicates approximate position of the study area. Figure modified from Deryabin (2012).

Table 1: Overview of seismic sequenses and suggested ages of the Barents Sea – Svalbard margin presented by different authors (Larsen 2003)

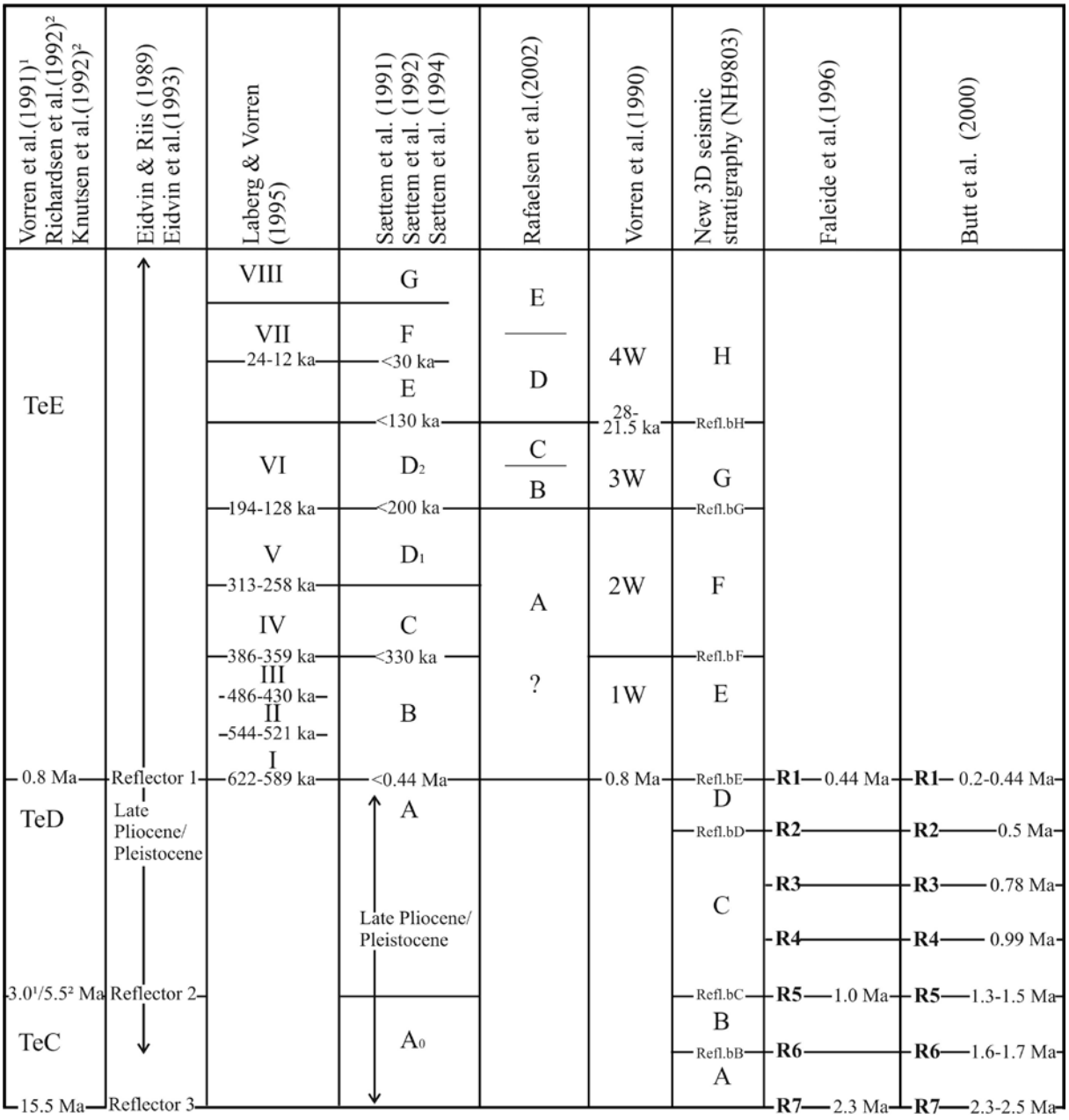

3.3 Geological and glacial history

The SW Barents Sea formed through 5 main stages of rifting from the Carboniferous to the final breakup of the North Atlantic during Tertiary. During the rifting phases, sediments were deposited in river systems, floodplains, alluvial fans and shallow marine environments. Spreading started first during the Palaeocene, and sediments accumulated on a developing continental shelf. As a cause of the large scale plate movements, the Western Barents Sea experienced uplift and erosion in Neogene age. A major unconformity called URU exists between Tertiary and overlaying glacial sediments. The Northern Hemisphere Glaciation started ~3.5 million years ago and the glacial history is divided into a three-phase model, the early phase, ~3.5 – ~2.5 Ma, the middle phase, ~2.5 – ~1 Ma, and the Late phase, <1 Ma (Knies et al., 2009)(Fig. 3.6). During the early phase the glaciers were restricted to mountain areas in the highland of Norway, Svalbard and Novaya Zemlya. During the middle phase, the ice sheets expanded out to the Barents Sea region. The Scandinavian and the Barents Sea Ice Sheet were probably not connected during this phase, and parts of the Barents Sea where still ice free (Knies et al., 2009). A change in the depositional environment happened within this period, 1.5-1.3 Ma BP, a period where the Barents Sea went from being sub-areal to a sub-marine environment. The glaciers expanded all the way to the shelf margin. Thick accumulations of glacial sediments where transported from land and deposited on the slope in large wedges, fans, and channels, especially during proximal ice conditions (Eidvin et al., 2000, Sejrup et al., 2005). The large amount of sediments deposited contributed to expansion of the shelf westwards to where it caused erosion on the shelf where the ice was grounded.

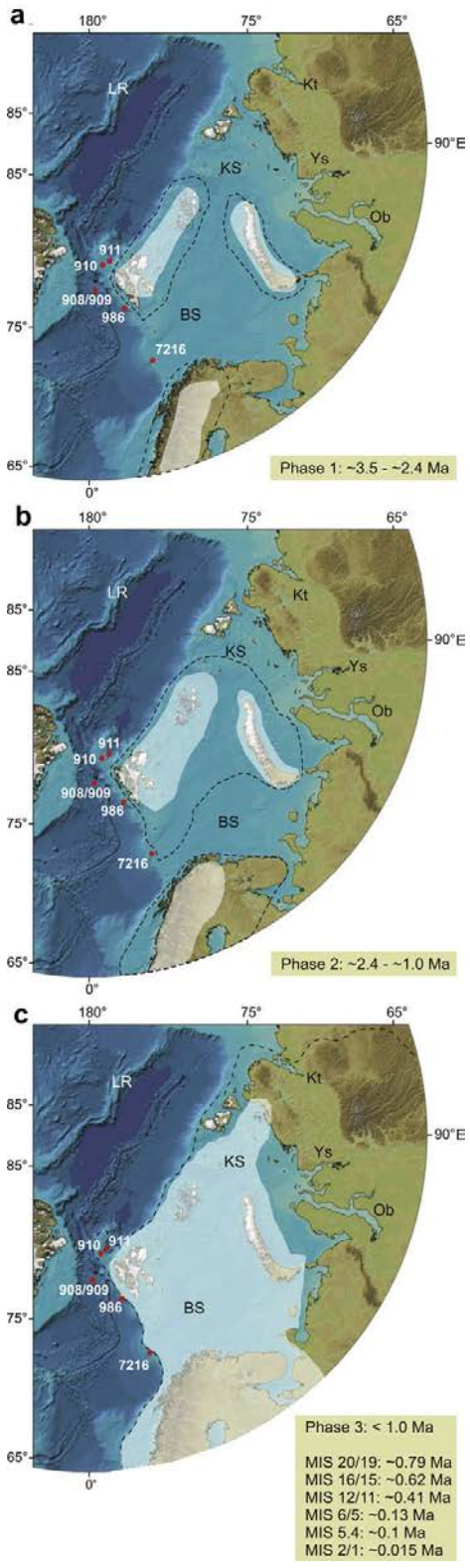

Figure 3.6: Maximum ice sheet expansion during the three stages of Plio-Pleistocene time. Within the three phases the glaciers have varied several times from being at the maximum extent to completely absent. Figure from Knies et al. (2009)

The Bear Island Trough (and other glacial submarine

valleys in the Barents Sea) reflects an area where the ice moved fast during glaciations. This caused a larger amount of erosion of the upper slope and shelf margin and deposition of sediments into a large, up to 4 km thick, fan on the lower continental slope and abyssal plain. The fan is called the Bear Island TMF (Laberg and Vorren, 1996).

Noteworthy, during the three phases, large variations in ice sheet extent existed from being completely absent during interglacial periods to maximum size for the phase during glacial times. Fig. 3.7 presents the late Plio-Pleistocene period with paleomagnetic zones, oxygen isotopes and temperature estimates.

The result of the temperature estimates show 9 interglacials during the last 0.78 Ma, and close to 20 glacial-interglacial cycles the last 2.5 Ma. Solheim (1996) suggested at least sixteen glacial advances along the northwestern margin over the last 1 Ma. In contrast, Sættem (1992) and Laberg and Vorren (1996a) indicated eight major ice advances during the last 0.44 Ma which is in agreement with Andreassen (2007), who suggested the same number. She also suggested the presence of grounded ice at a depth of 500 meters in the Bear Island Trough at the beginning of this period.

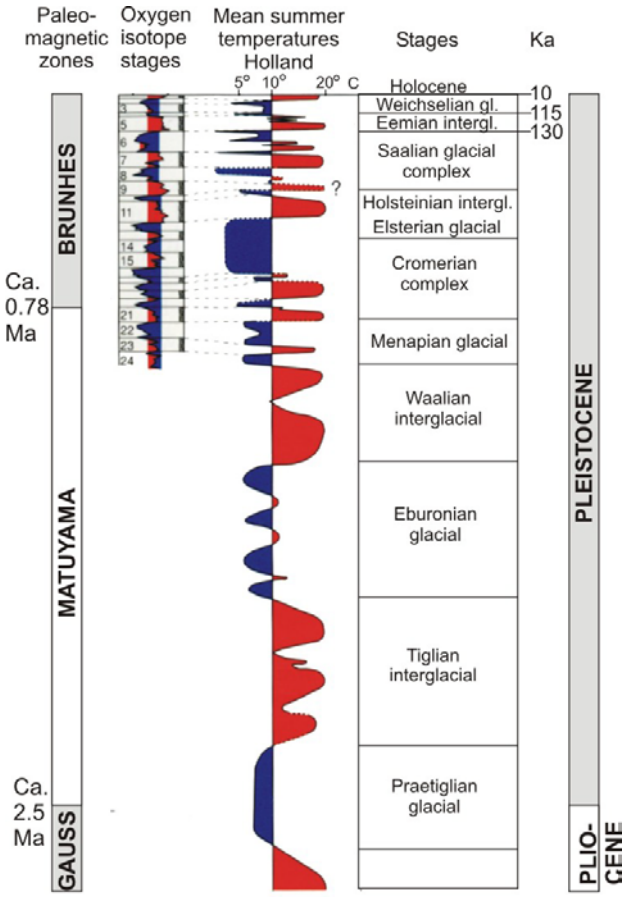

Figure 3.7: late plio-pleistocene period with paleomagnetic zones, oxygen isotopes, temperature estimates from Holland and related glacial and interglacial stages in the European stratigraphy (Larsen (2003), modified from Andersen and Borns (1997))

11 000 years have passed since the last ice age and the sea level has slowly transgressed up to the present day level. During Holocene the warm Atlantic water flooded the shelf and slope, changing the fauna from arctic to boreal (Vorren et al., 1989). Winnowing on the shallow shelf caused lag deposits of calcareous sand on the banks and in the troughs (Vorren et al., 1989). The process behind erosion and movement of sediments on the deeper continental shelf and slope started to be dominated by the two main ocean currents acting along the slope, the North Atlantic current and the Norwegian Costal Current. Sand waves may have developed during this time period and started to migrate on the continental slope in areas with high abundances of sand and strong currents flowing along slope.

Chapter 4 - Data, Methods and Tools

4.1 Data

The University of Tromsø acquired the 3D seismic dataset "SandWaveNorth_3D" in July 2011 using the new P-Cable high-resolution system(Petersen et al., 2010). Simultaneously, SIMRAD EM300 high-resolution multibeam data where acquired. An area of ~30km^2 was covered in July 2011 by the seismic vessel R/V Jan Mayen (now called Helmer Hansen). Not all planned seismic lines were accomplished due to bad weather. The acquired area, however, still covers the entire sand-wave field. Multibeam bathymetry data acquired by NGU in 2008 over the same area have also been used for this master thesis. 9 CTD stations were carried out during the cruise.

Further, the 2D seismic data sets NH-8401-Troms1, NH-9702-Sørvestnages and NPD-BJV1-86 have been used for stratigraphic correlation in the study area. Figure 4.1 show the location of the studied (3D) cube and the (2D) reference lines that were used for stratigraphic correlation.

3D seismic analysis, visualization and interpretation of the sand-wave field were done using the seismic interpretation program Petrel 2011. Bathymetric measurement and analysis were done using Fledermaus and DMagic.

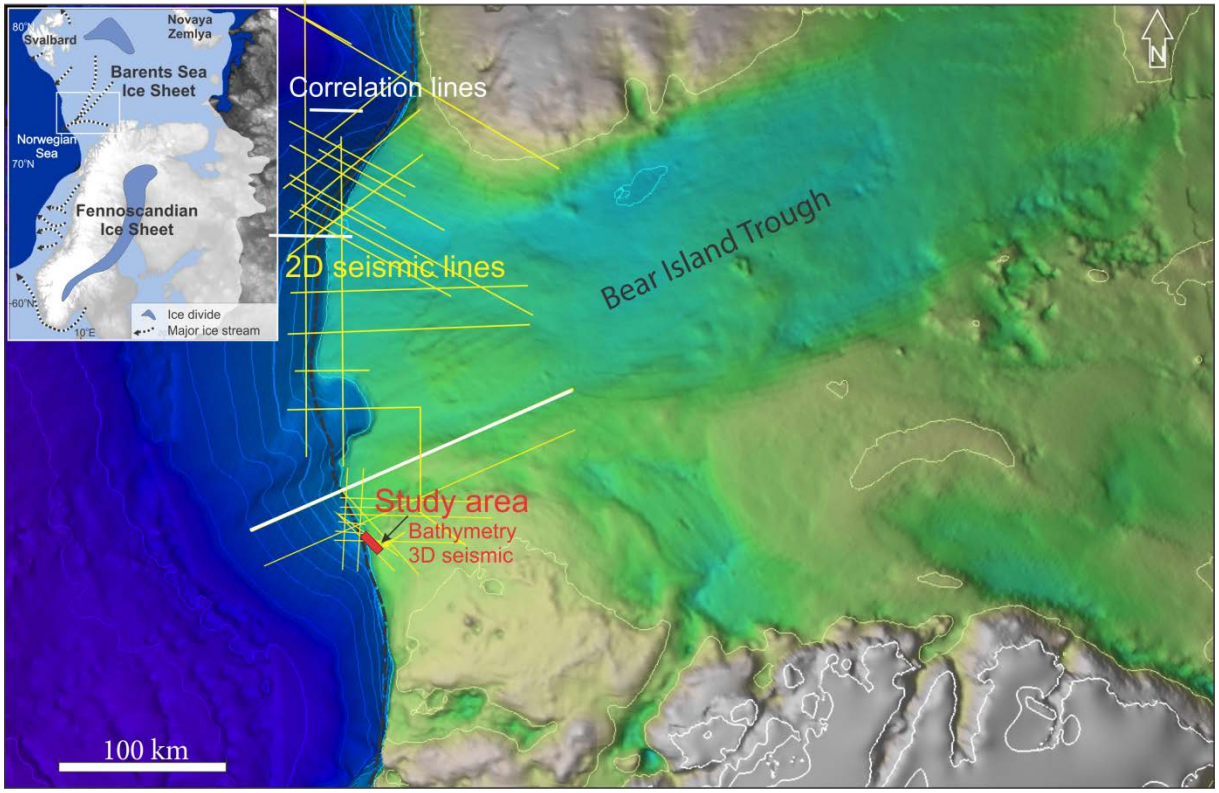

Figure 4.1: The map show the 3D seismic cube of the study area (red rectangle) and 2D seismic lines (yellow – NH9702, grey – NH8402) used for stratigraphic correlation.

4.1.1 P-Cable system

The P-Cable 3D seismic technology is a new acquisition method, first used in 2001(http://www.pcable.com/). Volcanic Basin Petroleum Research AS (VBPR) in cooperation with the National Oceanography Centre, Southampton (NOCS); Fugro Survey, Oslo (Fugro) and the University of Tromsø (UiT) developed this technology (http://www.pcable.com/).

The P-Cable system differs from conventional industrial 3D systems by shorter streamers (25 meters), short distance between them (12.5 meters), and a cross-cable that is towed behind the ship perpendicular to the steaming direction. A wire and a door on each side of the system hold up the cross-cable. The wires and doors are also responsible for controlling the direction and keeping an equal distance between the up to 16 streamers connected to the cross-cable. Each streamer consists of 32 hydrophones distributed in 8 channels. The distance between each hydrophone is 0.78 meters, and separation between the channels is 3.125 meters. The GI gun array is towed ~75 meters behind the ship and is fired every 3-4 seconds. Fig. 4.2 shows an illustration of the system. The system is preferable used for shallow high-resolution mapping of the upper 1.5 s TWT of the seabed.

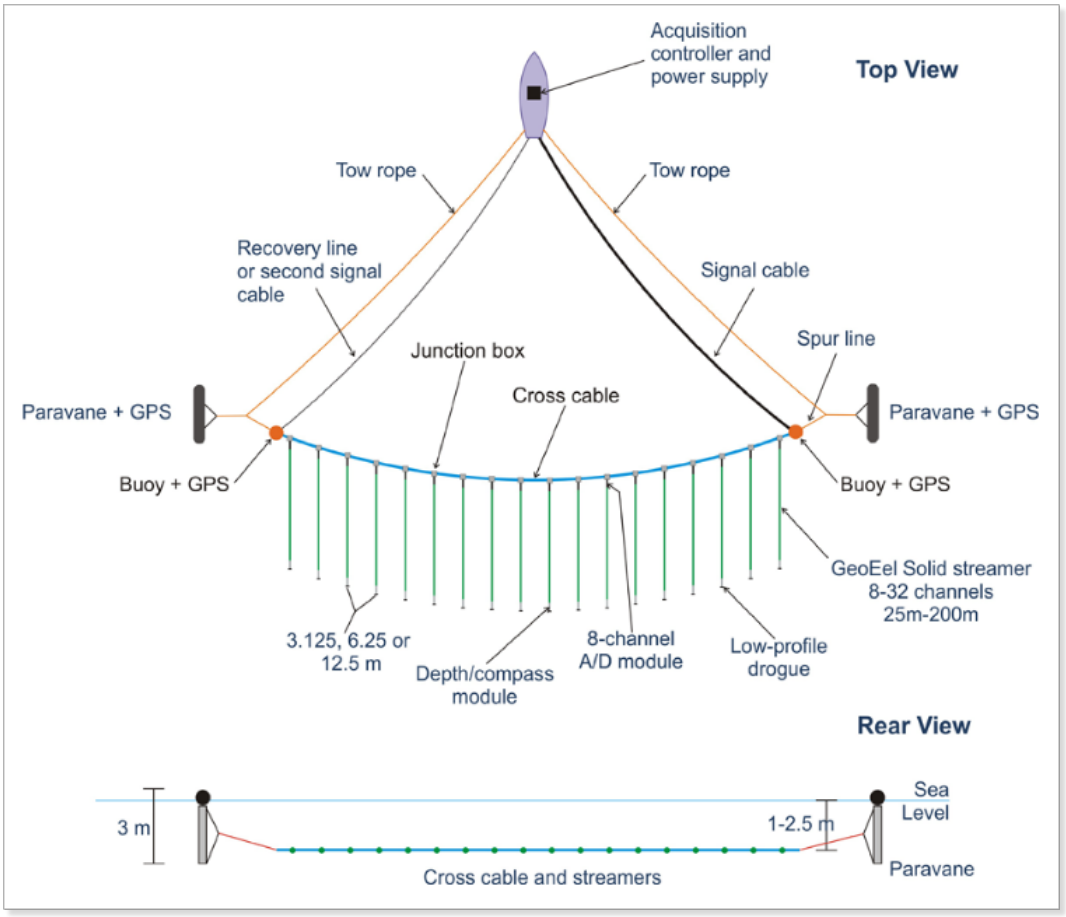

Figure 4.2: Basic system layout of the P-Cable System.

4.1.1.1 Seismic resolution

The resolution of the seismic data depends on the depth and velocity of subsurface strata. Greater depth and higher velocity results in a decrease in vertical resolution.

The horizontal resolution after migration is defined as the Fresnel zone = V/4*F. From an instantaneous frequency volume of the 3D seismic the average frequency is observed to be 200 Hz. Assuming a velocity of the sediments of 2000 m/s the horizontal resolution is 2000 m/s /(4*200) = 2,5 meter in average for the seismic cube. By assuming an uppermost velocity of 1600 m/s in the uppermost subseabed sediments, the resolution decreases to 2 meters. The vertical resolution is calculated to be 2.5 meter on average for the entire seismic cube. Figure 4.3 presents a comparison of conventional 3D seismic, single streamer high-resolution and the P-Cable 3D seismic data from the same area.

Data processing was done using the RadExPro 2011 software package. It consisted of navigational correction, trace editing, 3D binning, static and tidal correction, bandpass filtering, amplitude correction, normal move out, 3D stack and 3D stolt migration (velocity 1500 m/s). The bin size of the processed data is 6.25 m.

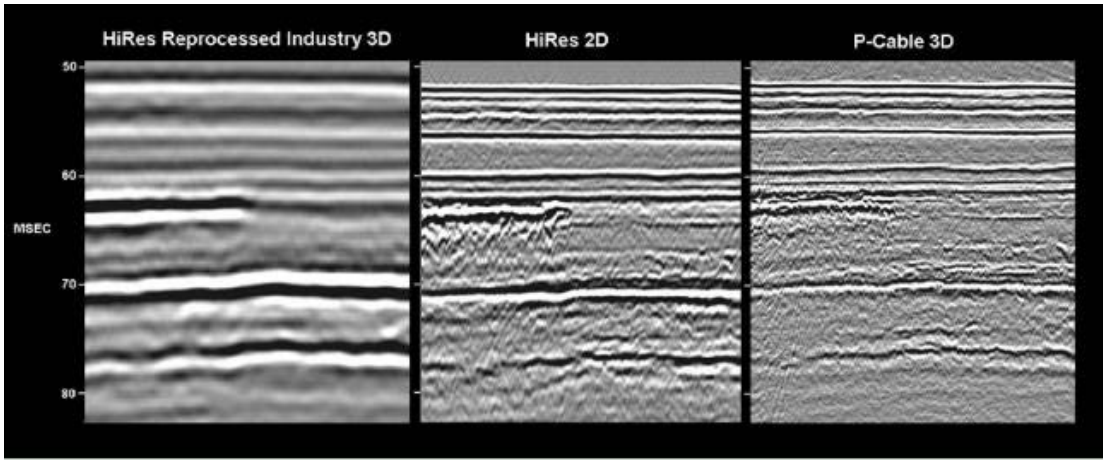

Figure 4.3: Comparison of industry 3D, single streamer high-resolution 2D and P-cable 3D data.

4.1.2 SIMRAD EM300 (multibeam echosounder)

The multibeam echosounder is used for seabed mapping (www.km.kongsberg.com). The device includes sensor interfaces, quality control display, sensor calibration, seabed visualization, data logging and integrated acoustic imaging for the seabed. It is suitable for mapping all water-depths, denoting 10 to 5000 meters below sea level. The systems swath width depends on the water depth, in great depth it can reach up to 5000 meters but decreases with decreasing water-depth. The resolution becomes higher with a denser grid and shallower water (JM Cruse report 2011). Since the device was operating during the entire 3D seismic survey the resolution is very high; the data where gridded by 5x5 meter (horizontal resolution is 5 meter).

4.1.3 CTD profiles

CTD (Conductivity, Temperature, Density) is a device for determining physical properties (TgS) of oceanic water masses.

4.1.4 Artefacts

Artefacts can appear in both bathymetric and seismic data due to for example acquisition noise. In the bathymetry data, artefacts are oriented perpendicular to the acquisition direction as straight parallel stripes (fig. 4.4a).

In the seismic data, migration noise, such as hyperbolic events are frequently appearing (fig 4.4b). The events become more dominant with an increase in depth. Stripes of different amplitude seem parallel to the inline direction and are also some kind of coherent noise (fig 4.4c).

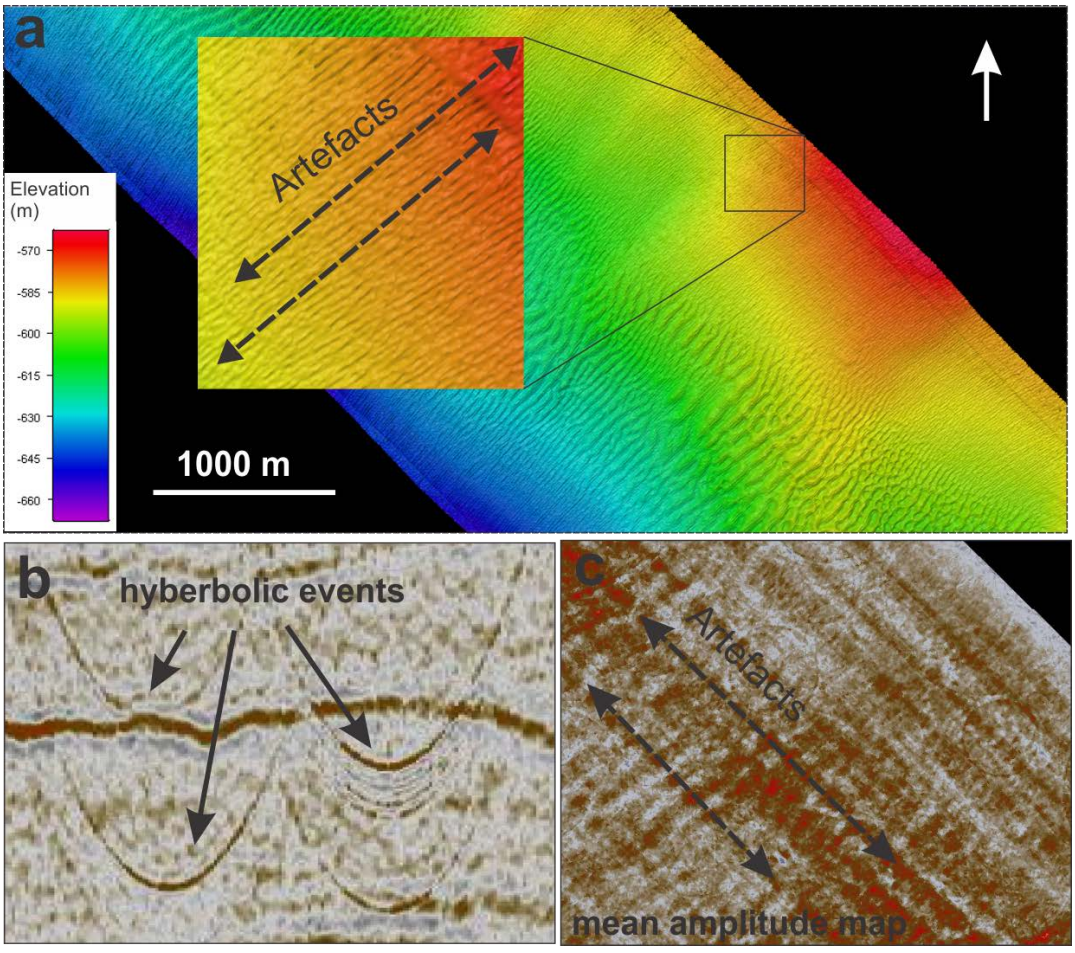

Figure 4.4: Artefacts, in the bathymetry data a) as parallel stripes perpendicular to the acquisition direction, and in the seismic data b) as hyperbolic events and c) as stripes of different amplitude parallel to the inline direction.

4.2 Petrel functionalities and tools

Petrel 2011 by Schlumberger has been used as an interpretation and visualisation tool for the 3D seismic and bathymetric data. The program includes 2D and 3D visualization, a diversity of visualization and interpretation tools, and classical as well as attribute functions. The data were imported in Petrel as SEG-Y files.

A blue colour in the seismic data indicates negative amplitude values or troughs, while red colours indicate positive amplitude values or peaks (fig. 4.5). The reflector of the seabed has a clear zero phase trough amplitude. Since the sea bottom always represents an increase in acoustic impedance (at the water sediment interface) one can confirm that a zero phase trough value in the dataset represents an increase in acoustic impedance (z*(rho)), and a zero phase peak value reflects a decrease in acoustic impedance. The 3D seismic data is presented as normal polarity display according to Badley (1985) and a reversed polarity display according to the SEG (Society of Exploration Geophysics). An example of a seismic trace with a trough (negative amplitude value) and peak (positive amplitude value) and corresponding colour scale is given in fig. 4.5. It shows the sea bottom reflector with overlapping wiggle traces.

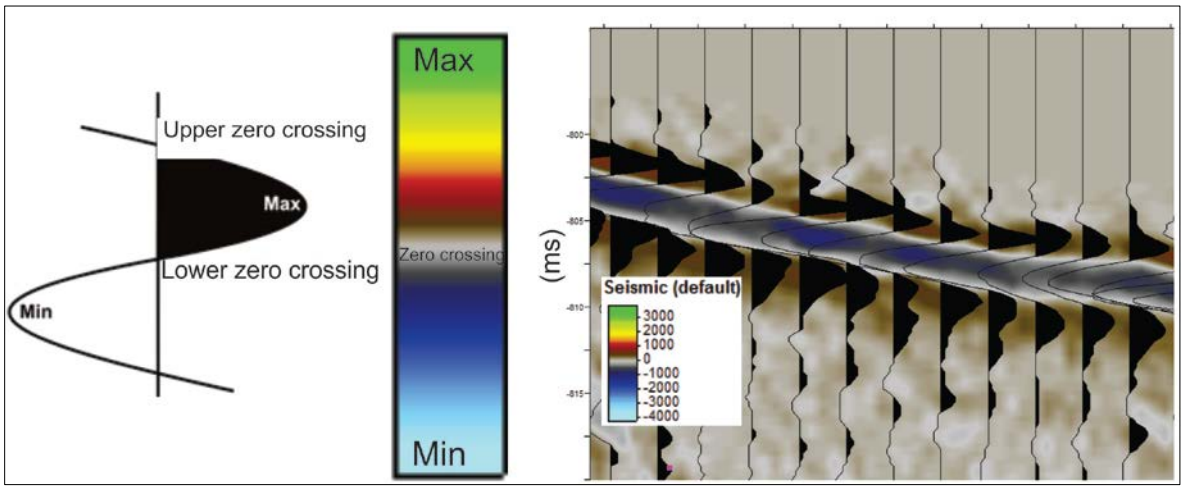

Figure 4.4: A seismic trace with corresponding colour scale used for this thesis. To the right is an example of the negative amplitude sea bottom reflector.

4.5.1 Seismic mapping techniques

2D and 3D windows have been used during the interpretation of horizons, structural elements and anomalies. Different mapping techniques such as 2D guided, 3D auto tracking, seeded auto tracking and manual tracking have all been used for horizon interpretation.

Auto tracking allows one to follow the extreme amplitude values on a reflector between two points (guided auto tracking) or from a "seeded" point (seeded auto tracking) to wherever the horizon becomes discontinuous or changes in amplitude values (2D and 3D seeded auto tracking). Manual tracking is used when the reflector becomes too blurry or discontinuous to follow with auto tracking. The paintbrush auto tracking function has been used after different densities of interpretation for within cross-lines and in-lines, depending on how easy the horizon is to interpret (how continuous and clear it is). The Paint Brush function that will track from the seed points within a specific 2D area.

Seismic cropped volumes **as smoothed volume, TraceAGC and variance** have been used as a help for interpretation within deeper horizons.

The help of structural smoothed volumes has interpreted some horizons or areas. This is a function that makes the reflectors appear more continuous and easier to autotrack by adding a gaussian weighted filter. The disadvantage using this function is poorer resolution on the surface.

Deeper horizons have been interpreted in traceAGC volumes (Amplitudal Gain Control). The attribute volume will enhance the instantaneous amplitudes with the normalized RMS amplitude over a specific window.

Variance volume has also been used for visualizing and recognition of horizons and trends in the seismic.

Volume rendering is a simple method for discovering"hidden" amplitude features. The method has been used in this study for visualizing the high amplitude sand waves and the channel features in the seismic cube. In settings for a seismic volume (cropped or not cropped) under the opacity function a curve can be drawn to partly make the volume opaque and transparent. All amplitudes around zero can for instance be made transparent, and the high amplitudes within the volume are the only visible data.

4.5.2 Surface attribute maps

To extract more information from the data and to localize and emphasize new features, attribute maps were used extensively. The most important attribute maps that have been used during this work are Isochron thickness maps, amplitude maps, curvature maps, and dip and azimuth maps:

- **Isochron thickness** - generates the time thickness between two reference surfaces.
- **Maximum/Minimum/Mena amplitude** - gives the maximum/minimum/mean values of amplitudes within a defined area around the surface, important for detection of high or amplitudes.
- **RMS amplitude** (Root Means Square) – is defined as the root of the sum of the squared amplitudes, divided by the number of samples (Shlumberger, 2010). The attribute map is used to isolate features laterally.
- **3D max curvature** – is a function that enhances values of curvature on the surface, and has been important for crest detection of the sand wave horizon.
- **Dip Azimuth map** – generates the perpendicular orientation of a surface in a 360 degrees scale – gives the strike. The lee-stoss asymmetry of the waves could be calculated with use of two colours on the dip azimuth scale, one for the northwest oriented flanks and another for the southeast oriented flanks.
- **Dip map** – calculates the dip of the surface. This map has been important for observing the dip of the sand waves on the seabed.

4.5.3 Specific techniques regarding visualising of sand wave geometry

A Dip azimuth map was used to determine the Lee-Stoss asymmetry: one colour (red) was used on the slopes directed to the Northwest and one colour (yellow) for the slopes directed South West. The relation between the horizontal lengths of the Lee-and Stoss sides could be observed and calculated from map view. Straight lines were drawn perpendicular to the crest-lines with a similar distance between, and the measurements where made following these lines (fig. 4.6).

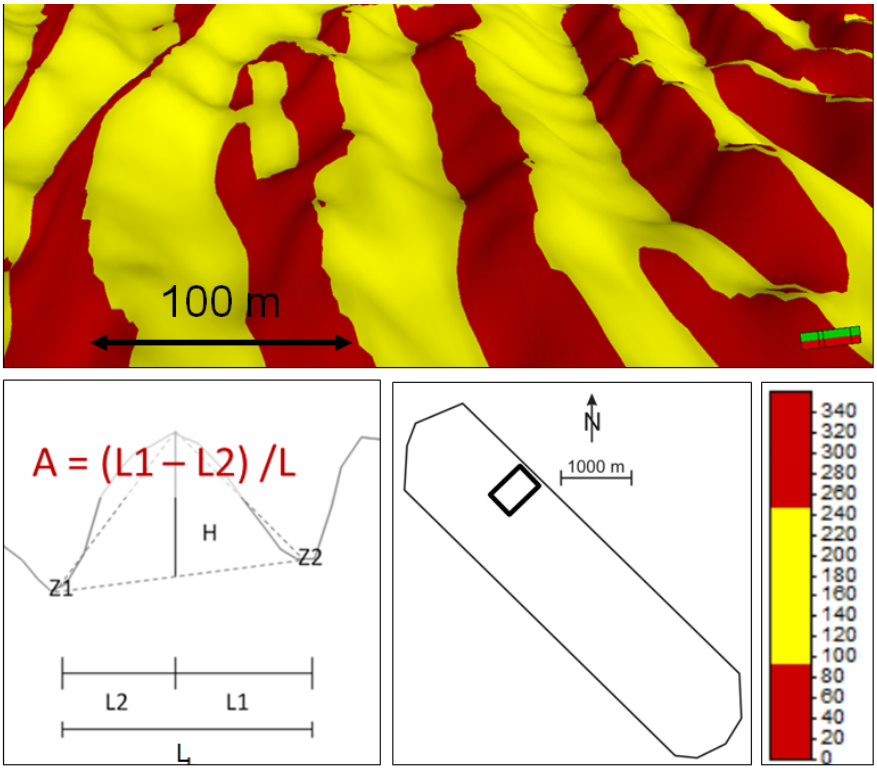

Figure 4.6: Dip azimuth map of the seabed, indicating the difference in length between the stoss,- and lee-sides. The lee-stoss-asymmetry was calculated from an overview map of this attribute map.

A smoothed surface of the sand wave horizon and an isochron map between this horizon and the real sand wave horizon has been made to determine the heights of the sand waves. The values of the attribute map are the vertical distance between the overall median seabed surface and the trough and peak positions. The downwards distance is represented by negative values, while the upwards distance to shallower depths is represented by positive values (fig. 4.7).

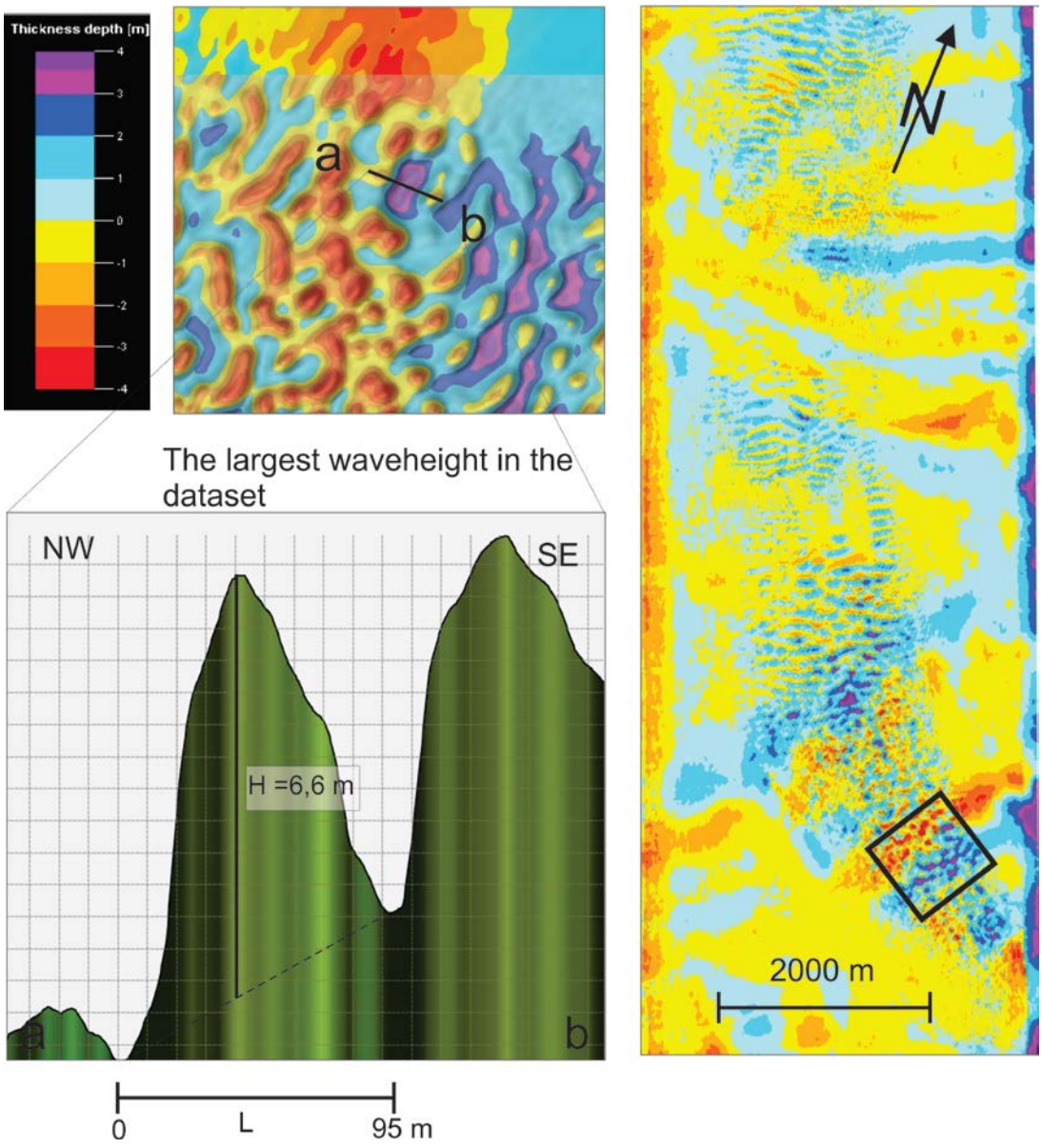

Figure 4.7: Thickness map of a smoothed surface of the seabed and the unsmoothed seabed, indicating the wave-height of the sand waves- The largest wave-height in the area is the area on the map with a largest range in colours across the single sand waves.

Profiles of the same coordinates from the two bathymetrical datasets (2008 and 2011) were compared to reconstruct potential migration rates for the three years period (fig. 4.8). First, the 2011 dataset was smoothed in order to increase coherence with the 2008 dataset. The relative migration rates were thereafter calculated by comparing the crest positions of the two datasets in Petrel, where a **max curvature and opaque function** was used to make only the crest lines visible. The approach remains with uncertainties but appears to be the most straight forward one.

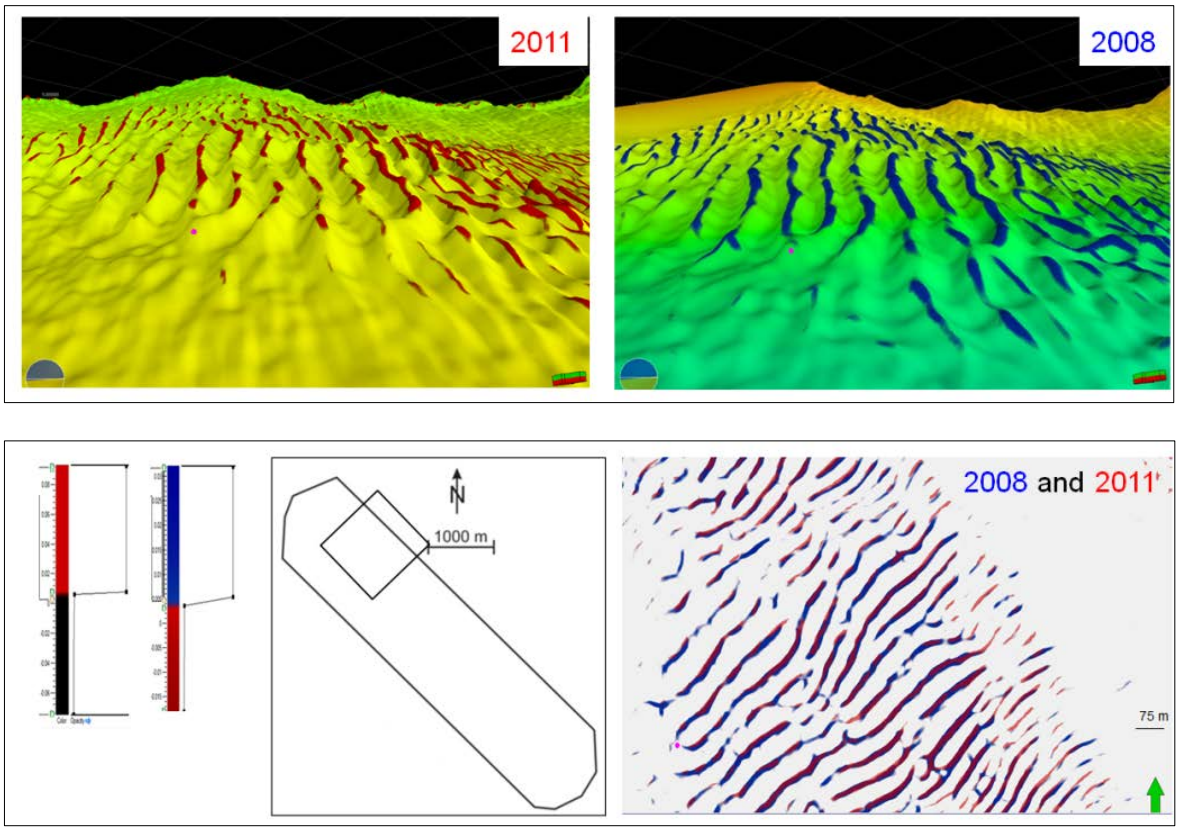

Figure 4.8: The red (2011 data) and blue (2008 data) crest-lines are presented by max curvature maps. They are laid on top of each other in the lowermost figure. The distribution of relative migration rates is thereby visible.

Chapter 5 - Results

5.1 CTD results and speculations of current-regime

The different water-masses are obvious in the cross section. The cross section indicates mainly three water masses, the NSAIW, the NAC and the NCC (fig. 5.1). The location of the CTD-stations that were used is indicated by white lines in the plot. The temperature of the water is given in the coloured column to the right of the figure, and the salinity is indicated by contour lines. According to the plot the transition between the two surface water-masses (NCC and NAC) and the deeper intermediate water (NSAIW) is located between 620 – 640 m.b.s.l.

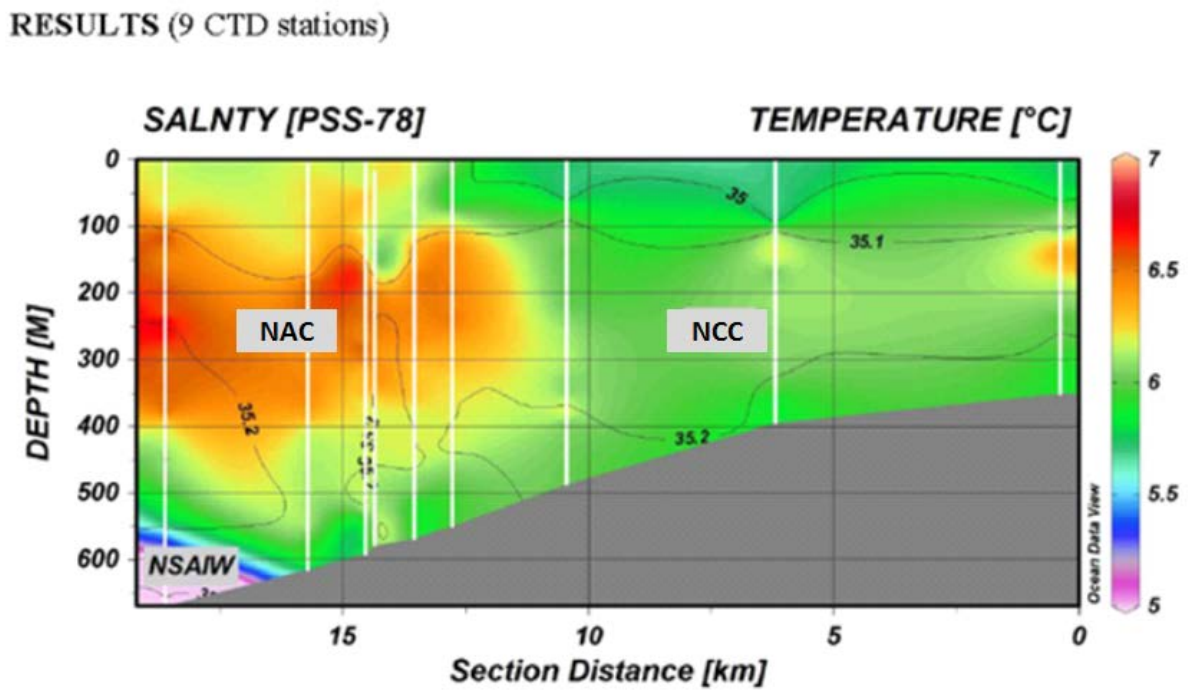

Figure 5.1: The integration plot of the nine CTD stations indicate the three major water masses across the sediment wave field, the NSAIW, NAC and NCC. According to the plot, the boundary between the two surface water-masses and the deeper intermediate water mass is located at 620 – 640 m.b.s.l. Recent studies, however, show that the boundary migrates up and down in a meandering pattern some hundreds of meters over the year (Skardhamar, Institute of Marine Research, pers.com.)

5.2 Bathymetric results

5.1.1 Geomorphology

Multibeam bathymetric data was used to study the geomorphic nature of the seabed in the study area. The area is located on the upper continental slope within 570 and 660 meters below sea level (m.b.s.l) (fig. 5.2). The seabed is on average dipping 0-4 degrees in an S-SW direction, which is also the direction of the continental slope in the area. The sand-wave field is situated on top of a channelized seabed (fig. 52). As seen from figure 5.2, the bathymetry data of 2008 covers a larger area on the slope and thereby also a larger area of these channels; three main channels are 1-2 km wide and 10-20 meters deep. The shape of the channels is straight to sinuous and directed NW-SE and N-S. Lightly defined topographic ridges are apparent inside the two northernmost channels.

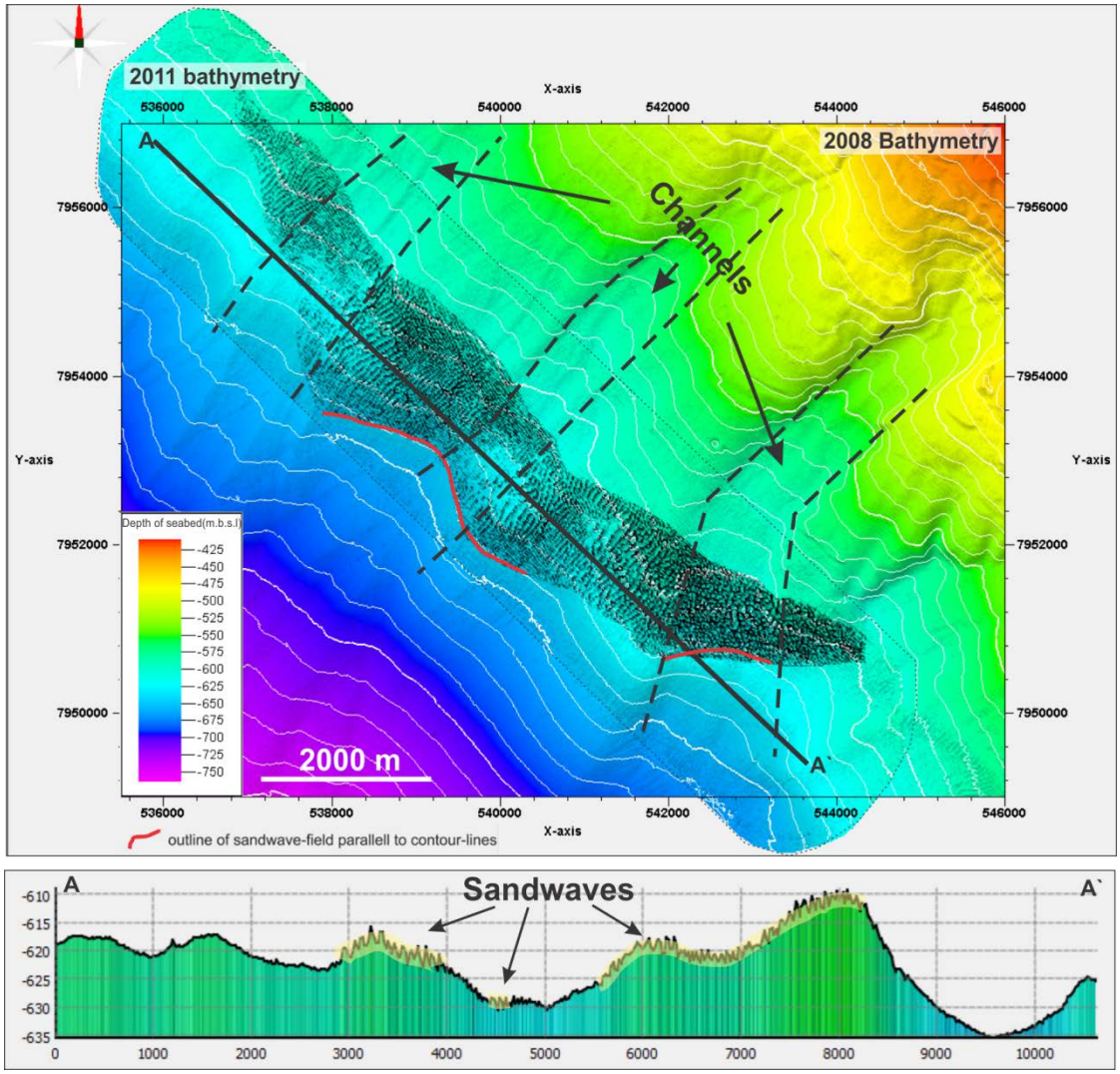

Figure 5.2: The bathymetry data of the sand-wave field N-2 acquired in July 2011 and 2008 are overlain by a max curvature map that highlights the crest-lines of the sand waves. The red lines indicate where the outline of the sand-wave field is parallel to the white contour-lines. The superimposed sand waves gives the seabed a rough signature compared to distal parts of the study area.

5.1.2 Area extent and shape of sand-wave field

The sand waves, located between 564 and 635 meters water depth, are clearly visible in the multibeam bathymetry data acquired in the 2008 and 2011 cruises (fig. 5.2). In map view, the sand-wave field is ~10 km in length, up to 2 km wide, and the entire area is calculated to be 12km² when drawing a polygon around the sand-wave field. Taking sinuosity and topography into account the sand waves migrate on a surface calculated to be ~22 km long.

The sand-wave field has a concave shape with the thickest part in the middle. The concave side faces the shelf edge. The width of the field or the length of the sand waves appears to be locally longer at the shallow banks between the channels (fig. 5.2).

5.1.2 Sand wave Geometry

5.1.2.1 Crest lines

The crest-lines of the sand waves are highlighted from a max curvature map, visualized in fig. 5.3. The crest-lengths in the bathymetry data are observed to vary form 60 m - 2000 m. Length of the crest-lines is in most places also related to the width of the sand-wave field, which means that where the width of the sand-wave field increases, as on the topographic highs, the crest-lengths also tend to increase. However, on the margins of the sand-wave field small sand waves exist, that are not attached to larger sand waves which lie closer to the core of the sand-wave field. This makes the sand-wave field wider than the crest-lengths in those core areas.

The sand waves show slightly sinuous crest-shapes, with the exception of an area in the southern part where the crests of the sand waves appear more as barchan-type sand waves. Barchan-type sand waves are usually shorter-crested with horns pointing in the direction of net transport (Belderson et al., 1982). For this case, the horns are observed to point in a SE direction, indicating a net transport to the SE (fig 5.3).

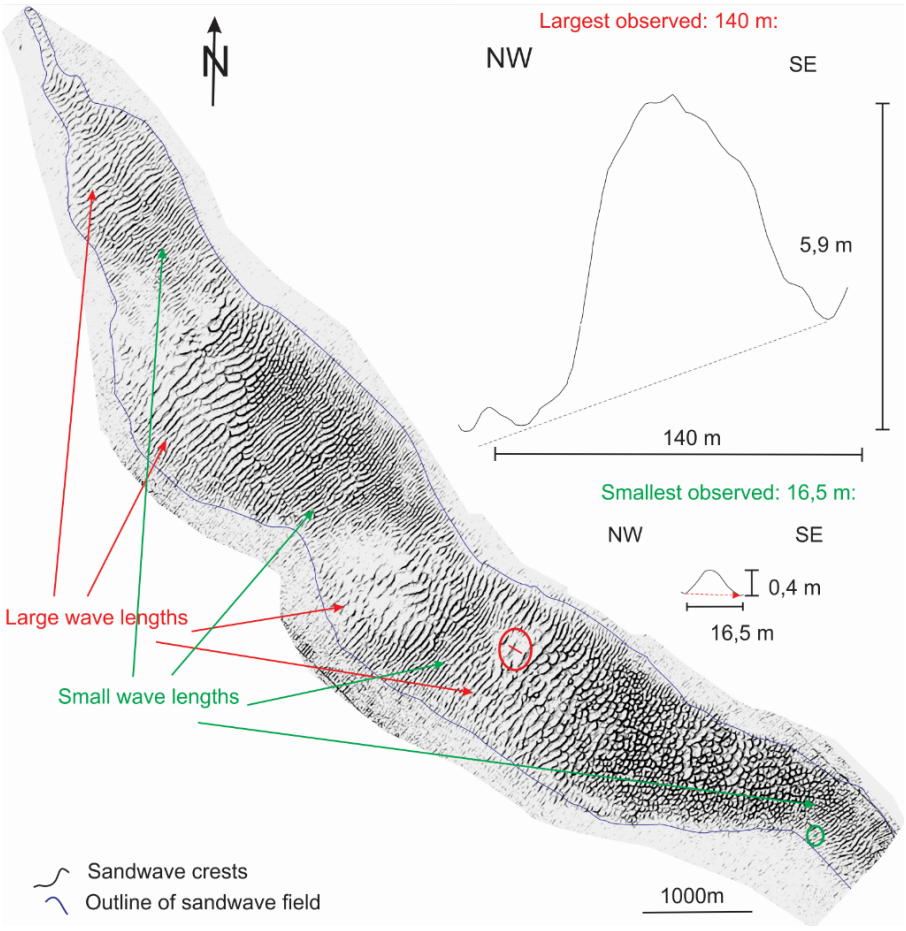

Figure 5.3: Interpretation of sand wave crests and examples of the largest and smallest wavelength found in the area.

5.1.2.2Wavelength

The crest map of figure 5.3 also gives the distribution of wavelengths since a wavelength is defined as the horizontal distance between the neighbouring crest-lines. The wavelengths observed in profiles are calculated from eq. 1 (chap. 2). Wavelengths are observed to vary form ~16.5 - 140 meters in the study area, but seem to have an average of 70-80 meters. Wavelengths smaller than 10 meters should not be apparent in the bathymetry data due to the resolution of the data (5x5m). From video-transects, however, we know that mega-ripples and ripples with wavelengths up to ~ 10 meters exist on top of the sand waves (fig. 1.3).

An example of one of the smallest and largest wavelengths from the bathymetry data is shown in figure 5.3. The largest wavelengths (>100m) are also the sand waves with the longest crest-lines (~2km) located on highs between the channels, while smaller wavelengths (<100 m) and crest lengths (~0.5 km) occur most frequently inside the channels (fig. 5.4). In addition, wavelength tends to increase towards the centre of the sand wave – field. An example is given in figure 5.5, where a single sand wave can be followed towards the inner part of the sand-wave field.

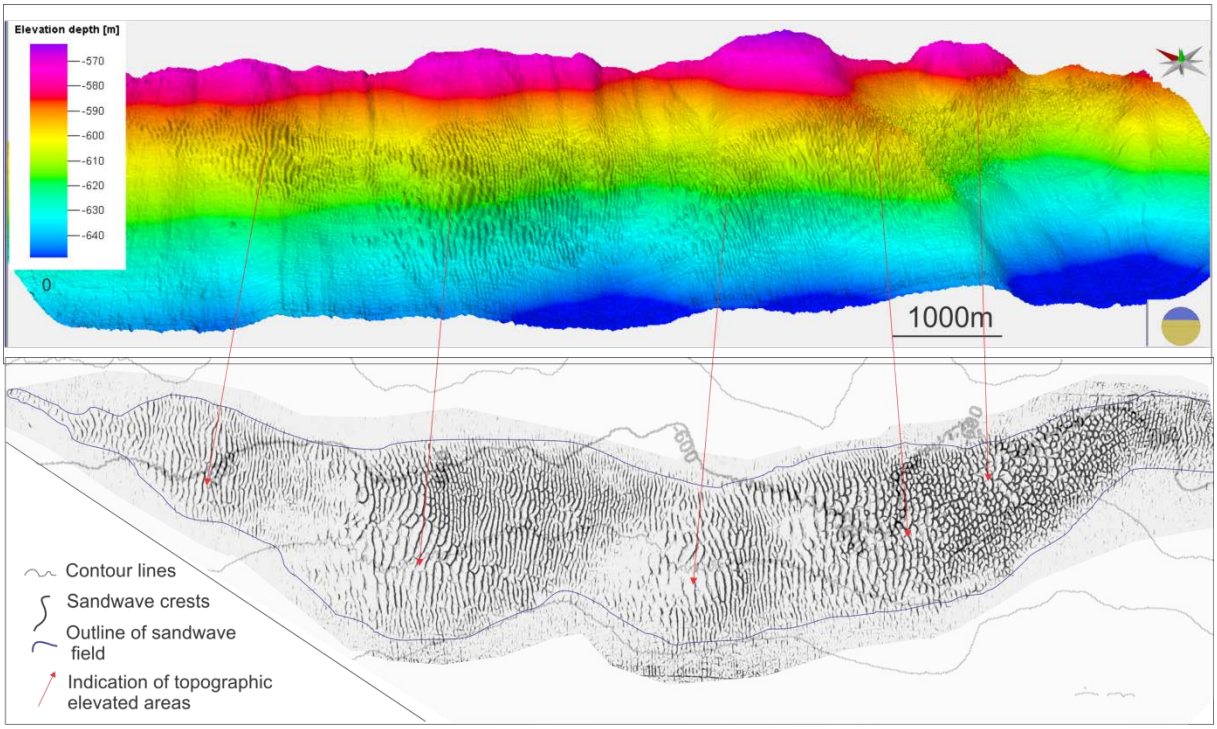

Figure 5.4: Shows the relation between the distribution of wavelengths and seabed elevation. As seen from the figure; on the highest elevated areas are where the largest wave-lengths and crest-lengths are located.

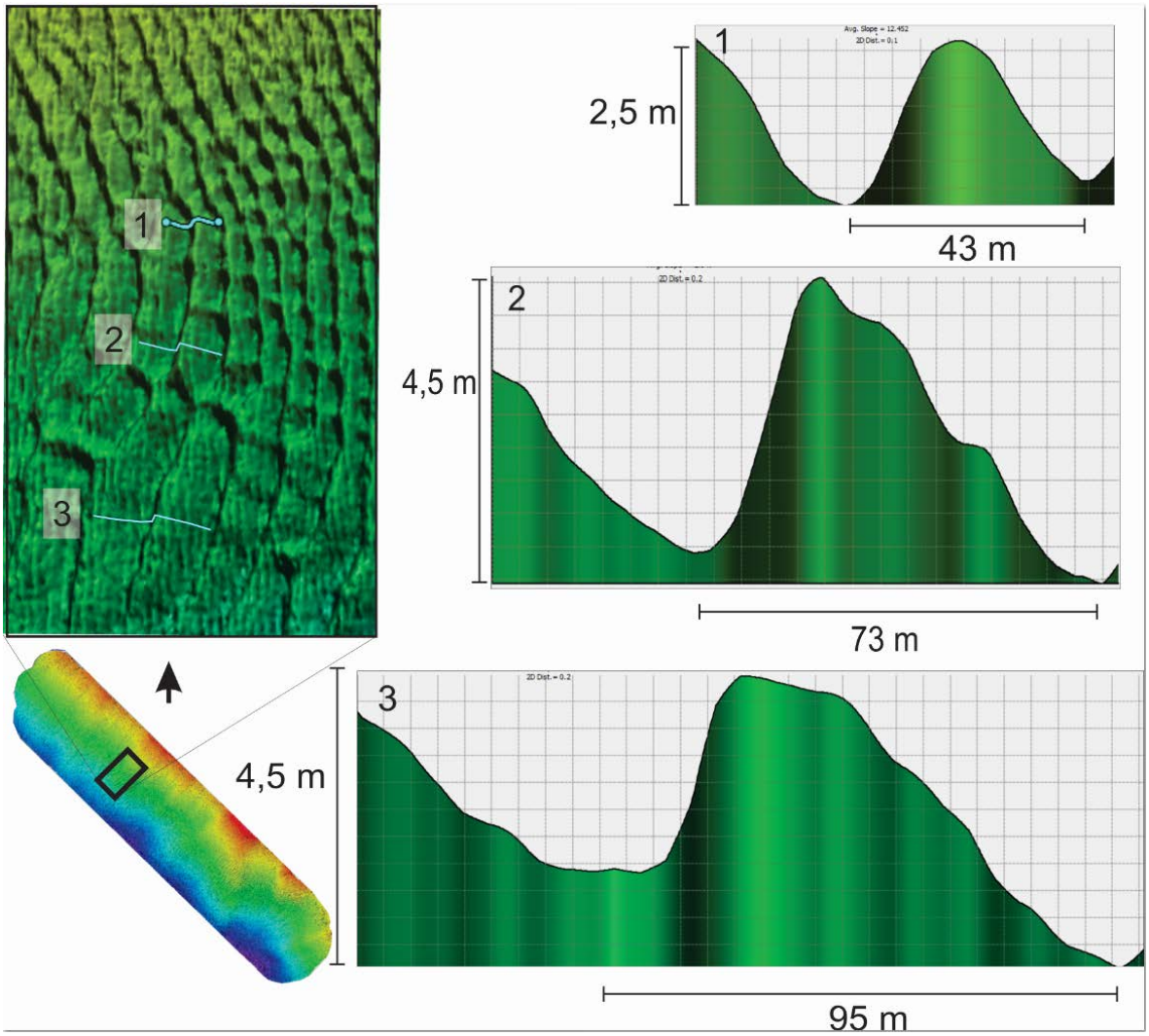

Figure 5.5: Following a single sand wave towards the middle of the sand-wave field, indicating larger wavelengths towards the middle. The figure also shows how the sand waves increase in asymmetry with larger wavelength.

5.1.2.3 Wave-height

The spread of wave-heights are observed from a thickness map between a smoothed seabed and the actual seabed, which is explained in chap. 4 (fig. 5.6 and 5.7), while the actual heights are calculated from eq. 2 (chap. 2). The results of these two integrated methods show that the wave-height of sand waves in the study area reaches up to 6.6 m. In average, the wave heights seem to be 1-2 meters (according to ta histogram for the thickness map). The smallest heights are located in the depressions and on the margins of the sand-wave field while the largest wave-heights are found in the southern part of the sand-wave field (fig. 5.6). On topographic highs however, the general wave-height is also greater, as seen from examples in figure 5.8. The wave-heights seem also to increase towards the middle of the field. The close-up showing the average sand wave-heights in figure 5.6 also demonstrates this observation. Another example is illustrated in figure 5.9, where one can follow a single sand wave towards the middle of the field. In this case the wavelength does not seem to increase noticeable towards the middle of the sand-wave field compared to the wave-height.

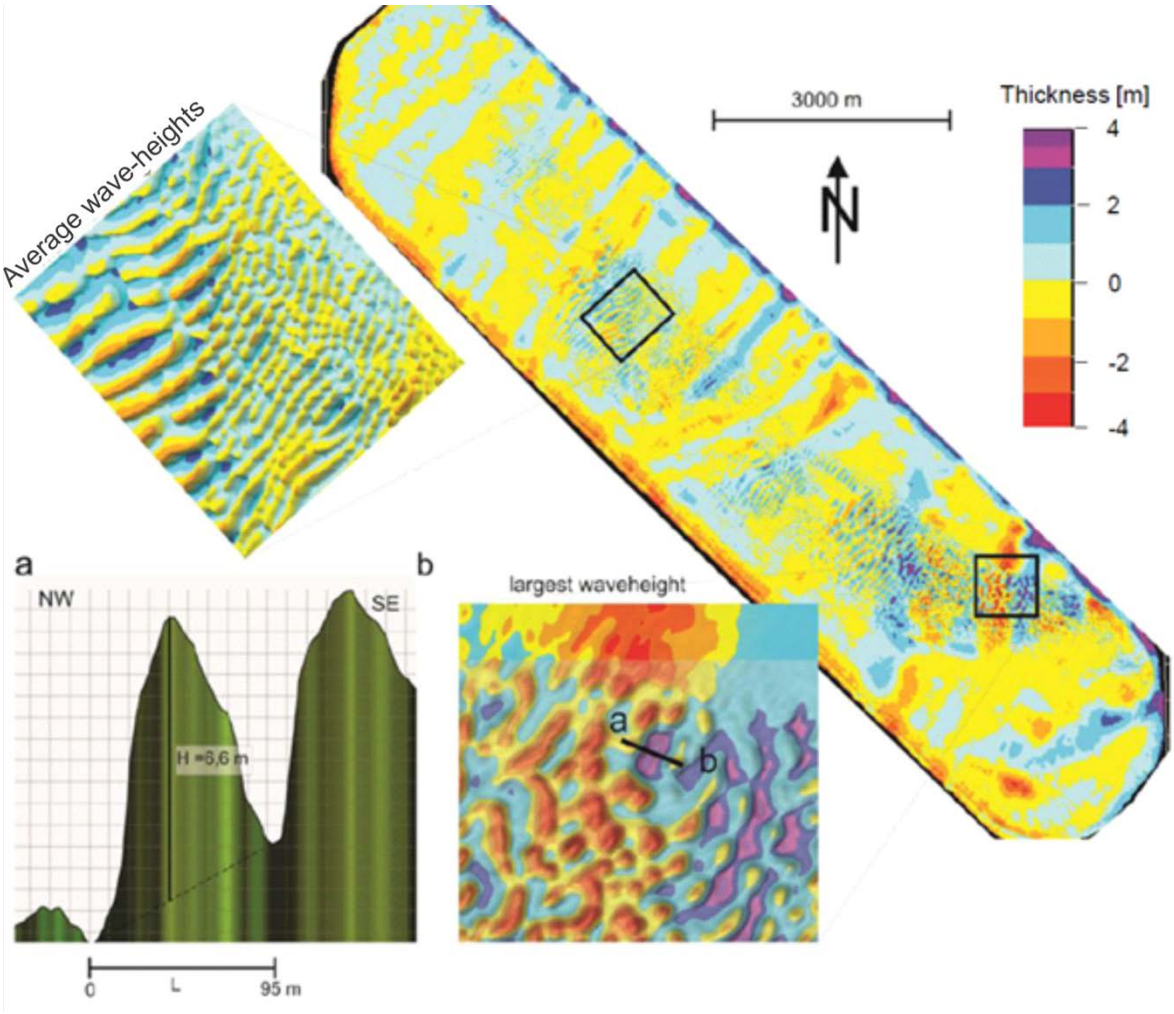

Figure 5.6: Thickness map of a smoothed surface of the seabed and the unsmoothed seabed, indicating the wave height of the sand waves. Transect a-b show the location and cross-section of the largest wave-height observed in the sand-wave field, while the snap-shot in the upper left corner labelled “average wave-heights” indicate the average sized wave-heights between 1-2 meters high.

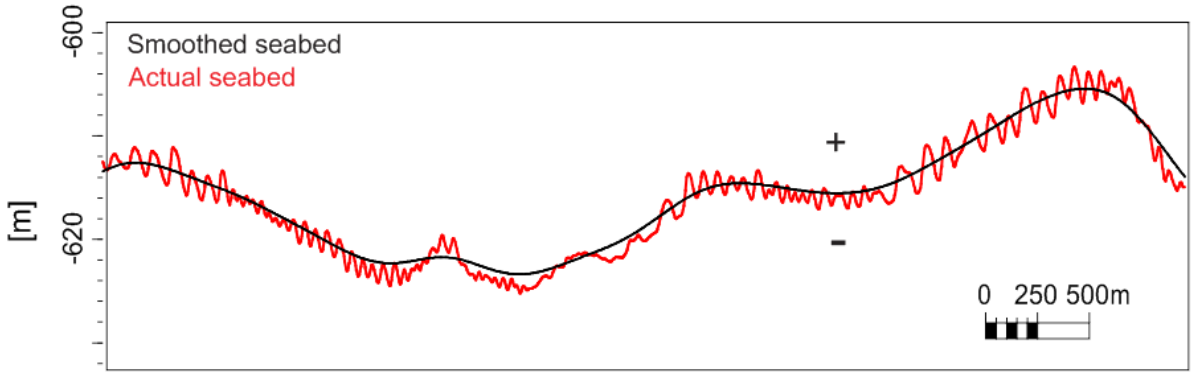

Figure 5.8: Cress-section example of the smoothed and the actual seabed used for generation of the wave-height map of the sand wavefield.

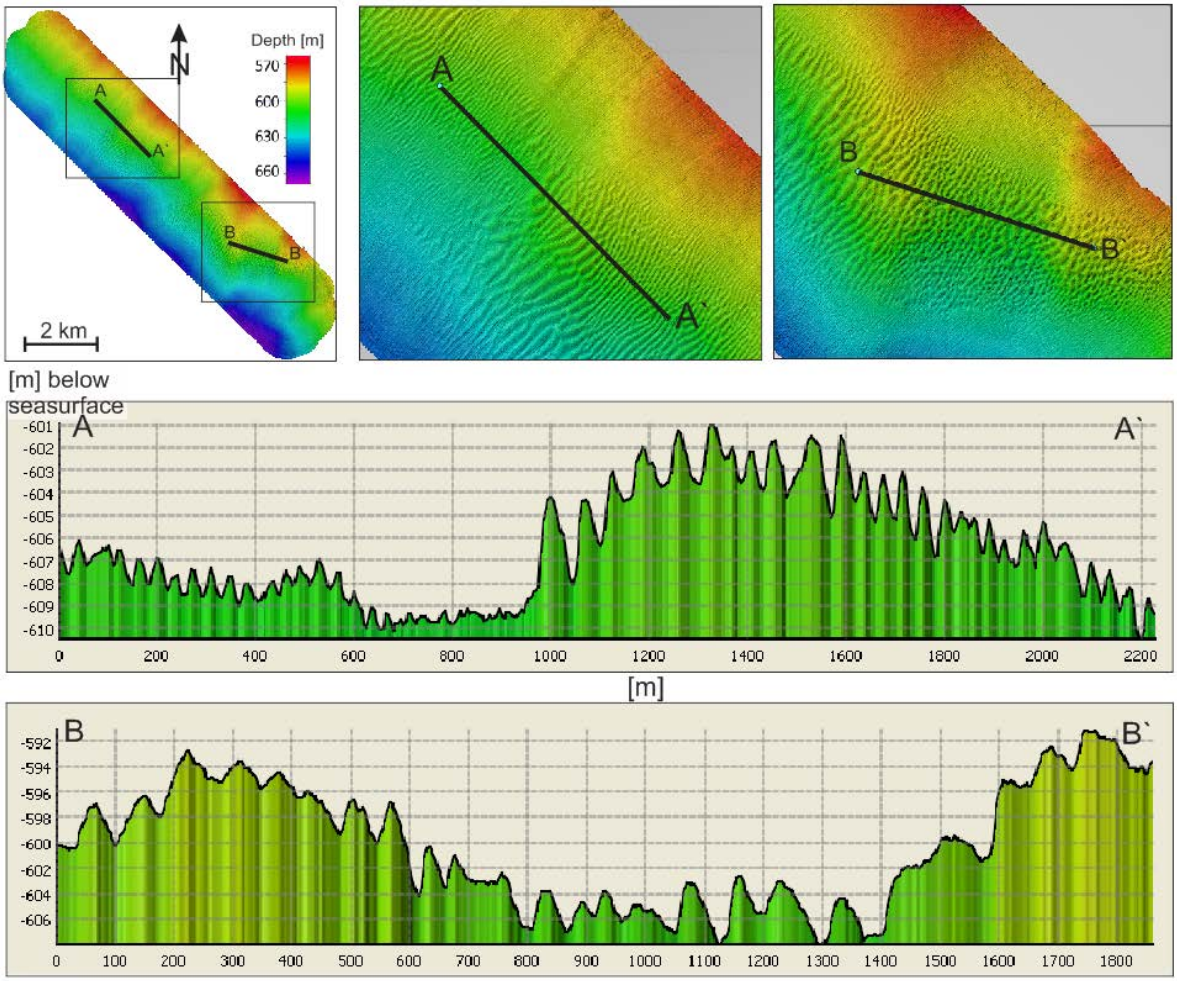

Figure 5.9: Two bathymetry and cross-section examples of the sand waves in N-2. The sand wave geometry (wavelength, height and asymmetry) seems to be a function of the underlying bathymetry in some areas, but that is not always the case. Profile A shows a better correlation between the bathymetry and sand wave geometry than profile B

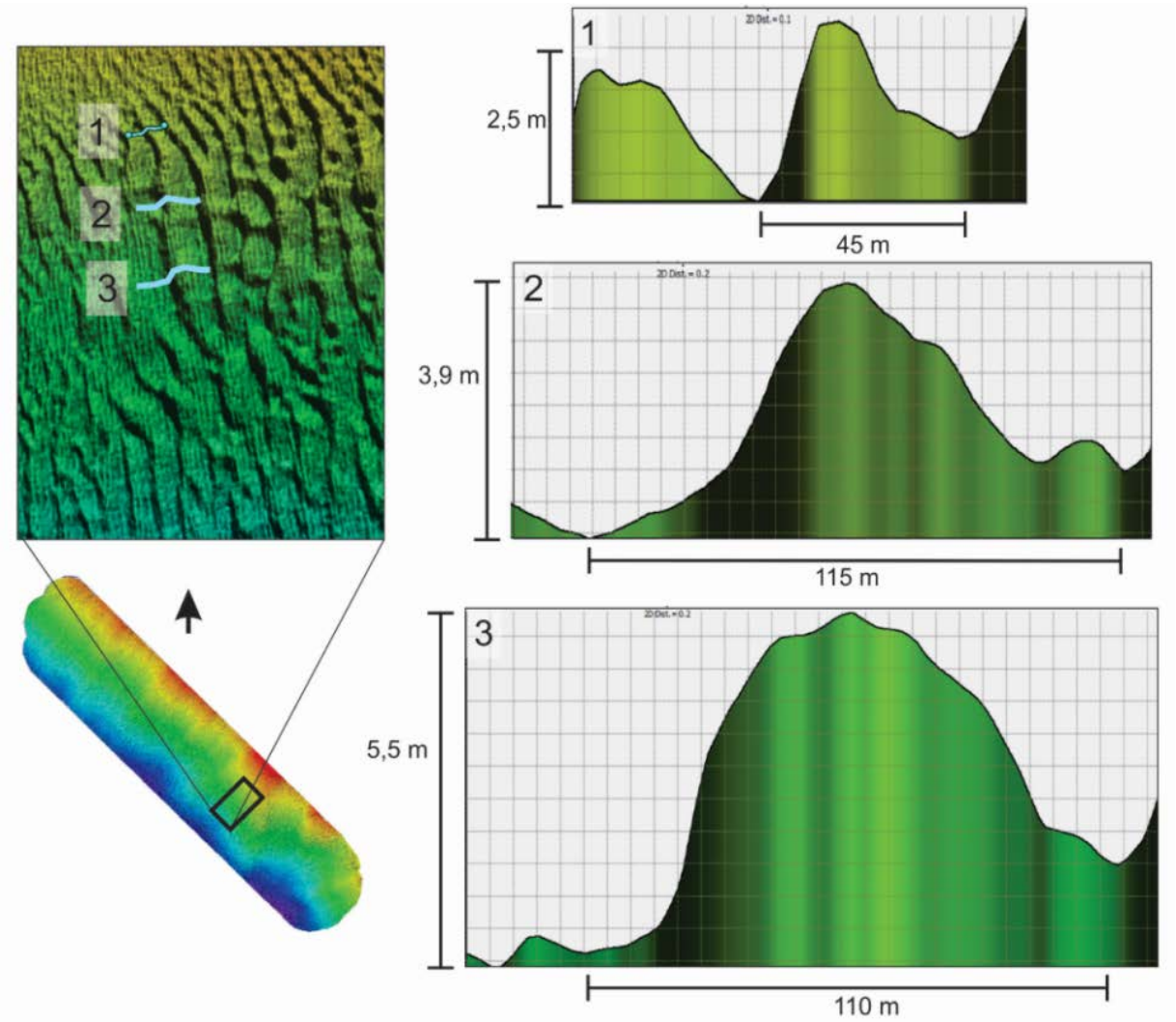

Figure 5.10: Following a single sand wave towards the middle of the sand-wave field, indicating larger wave height towards the middle. The figure also shows how the sand wave decreases in asymmetry with larger wave height.

5.1.2.4 Wave-height/Wave-length/Bathymetry plots

Figure 5.11 shows wave-height versus wave-length in two slightly different water depths (605 and 611.5 m.b.s.l) of a selected area within the sand-wave field. The results indicate a linear increase of wave-height with wave-length. However, there is also a high spread of between measurements; for example sand waves of a height of ~1.5 meters are observed to vary in wavelength from 20 to 70 meters, and wave-heights of ~3.5 meters appear to show varying wavelength from 65 to 115 meters. In the three lowermost plots of fig. 5.11, bathymetry is also taken into account, indicating that variations in wave-lengths are quite consistent with variation in bathymetry, while wave-height shows a slightly poorer correlation.

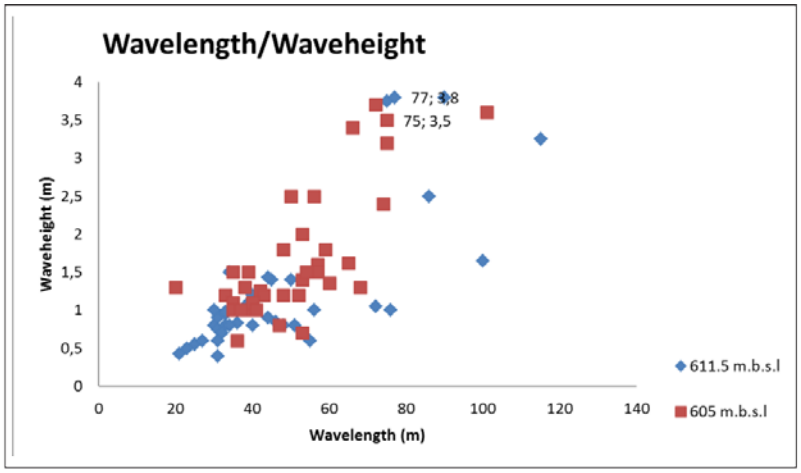

Waveheight [m]

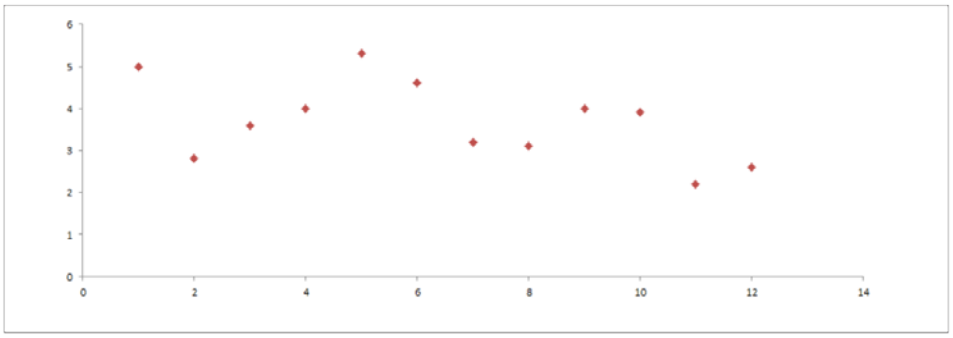

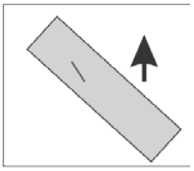

Wavelenght [m]

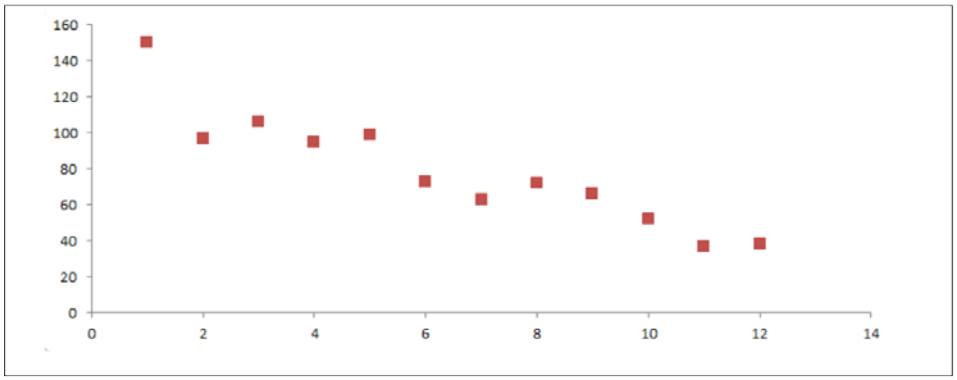

Underlaying bathymetry [m]

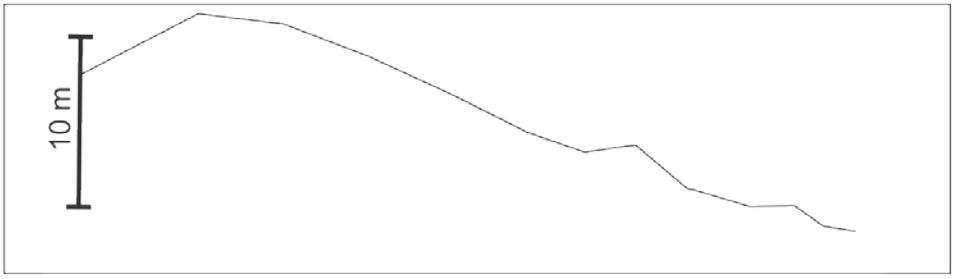

Figure 5.11: (uppermost figure) presents the relationship between wave-height and wave-length in two slightly different water-depths (605 and 611.5 m.b.s.l) of a selected area within the sand-wave field. The three lowermost plots compare wavelength, wave-height and bathymetry in the area given to the left.

5.1.2.4 Lee-and Stoss Side Dip

The sand waves show overall the steepest dip (lee-side) to the NW, an observation that indicates a regional migration direction in the same direction along the continental slope. This observation also correlates with the regional oceanic currents in the area (NAC and NCC) that propagates along the slope in a NW direction.

A dip map of the bathymetry shows a lee side dip of up to 16 degrees, and a general stoss side dip of up 10 degrees, with the exception of the disturbed southern part where the dip of the stoss sides also reaches up to 16 degrees (fig. 5.12). A general observation is that the dip of the sand waves increases with the increasing size of the sand waves. This observation is found on sand waves with wavelength that vary from ~30 to 140 m. Smaller sand waves are not represented by real dip since the resolution is too small to visualize the real shape of the sandwaves.

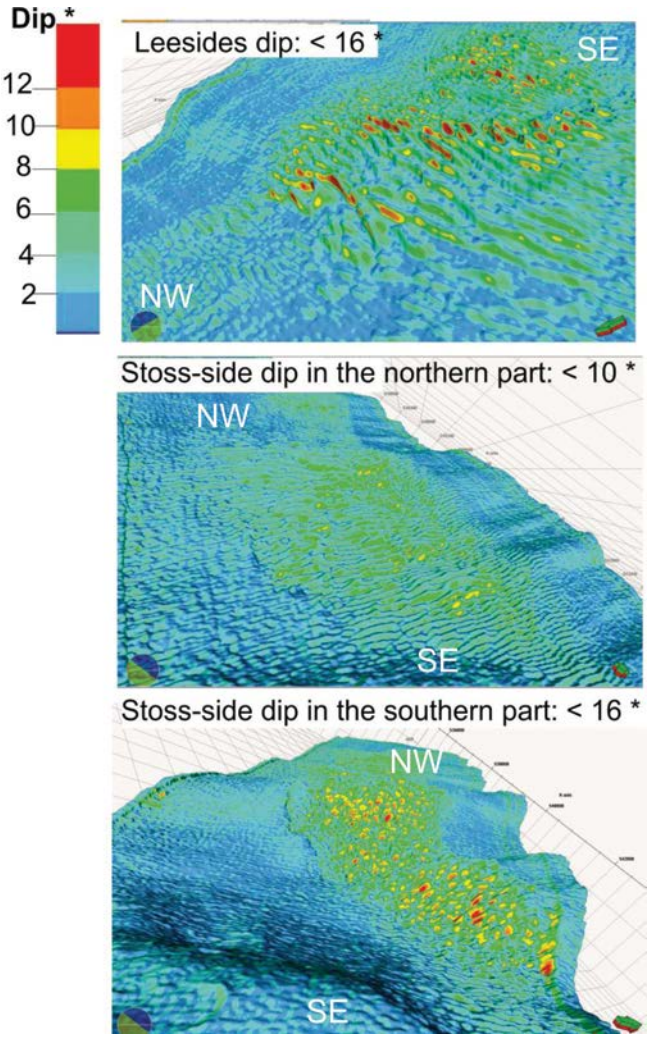

Figure 5.12: 3D windows visualized from NW and SE of dip-map of the bathymetry data, showing the general dip of the lee-, and stoss-sides of the sand waves.

5.1.2.5 Asymmetry

Asymmetry values in the sand-wave field are calculated by eq. 3 (chap. 2), - from a dip-azimuth map of the sand-wave field.

Asymmetry values are varying from -0.4 to as great as 0.67. Positive values of asymmetry are apparent where the steepest side is oriented to the NW and negative values where the steepest side is oriented opposite i.e. SE. In general, the asymmetry seems to vary with size of the sand waves, a larger asymmetry occurs on larger sand waves. The sand waves on elevated areas have been calculated which have the largest lee-stoss asymmetry, on average ~ 0.3-0.4, while in depressions where smaller sand waves occur the asymmetry values seem to be on average ~ 0.2-0.3. A good example of this observed correlation is presented in figure 5.13 (profile 1, the related asymmetry of the sand waves is seen from a map point of view in the subfigure labelled 1.1). The sand waves show distinctly larger values of asymmetry towards more elevated areas and larger sand wave size. An increase of asymmetry with size is also observed across several single sand waves that increase in size towards the middle of the field (example see figure 5.5). This is however not consistent across the sand-wave field. An example is on the margin of the barchans-type sand waves in the south where no particular pattern of geometry seems to exist (also seen in figure 5.13, profile 2). Within the barchans-type sand waves the asymmetry tends to be low even though the wave-height is mostly large here. An area of negative values of asymmetry is calculated in the southern tip of the sand-wave field, that is, further SE of the Barchan-type sand waves. Asymmetry values of - 0.3 and – 0.4 are present in this area.

Indication of migration direction based on asymmetry of the sand waves

One can indicate the directions of migration of sand waves based on the assumption that sand waves migrate in a direction perpendicular to the crest orientation in the direction i.e. in the direction from the stoss side- lee side of a sand wave. A map is presented in figure 5.14, and the arrows in the figure indicate the migration direction. A uniform migration direction is indicated in the northern 3/5 part of the sand-wave field where the shape of the crest-lines are slightly sinuous. Within the barchans-type sand waves, it was more challenging to locate the direction of migration; - a variety of directions was indicated. Negative values of asymmetry values indicate reversed sand-wave migration on the south eastern tip of the sand-wave field (fig. 5.14).

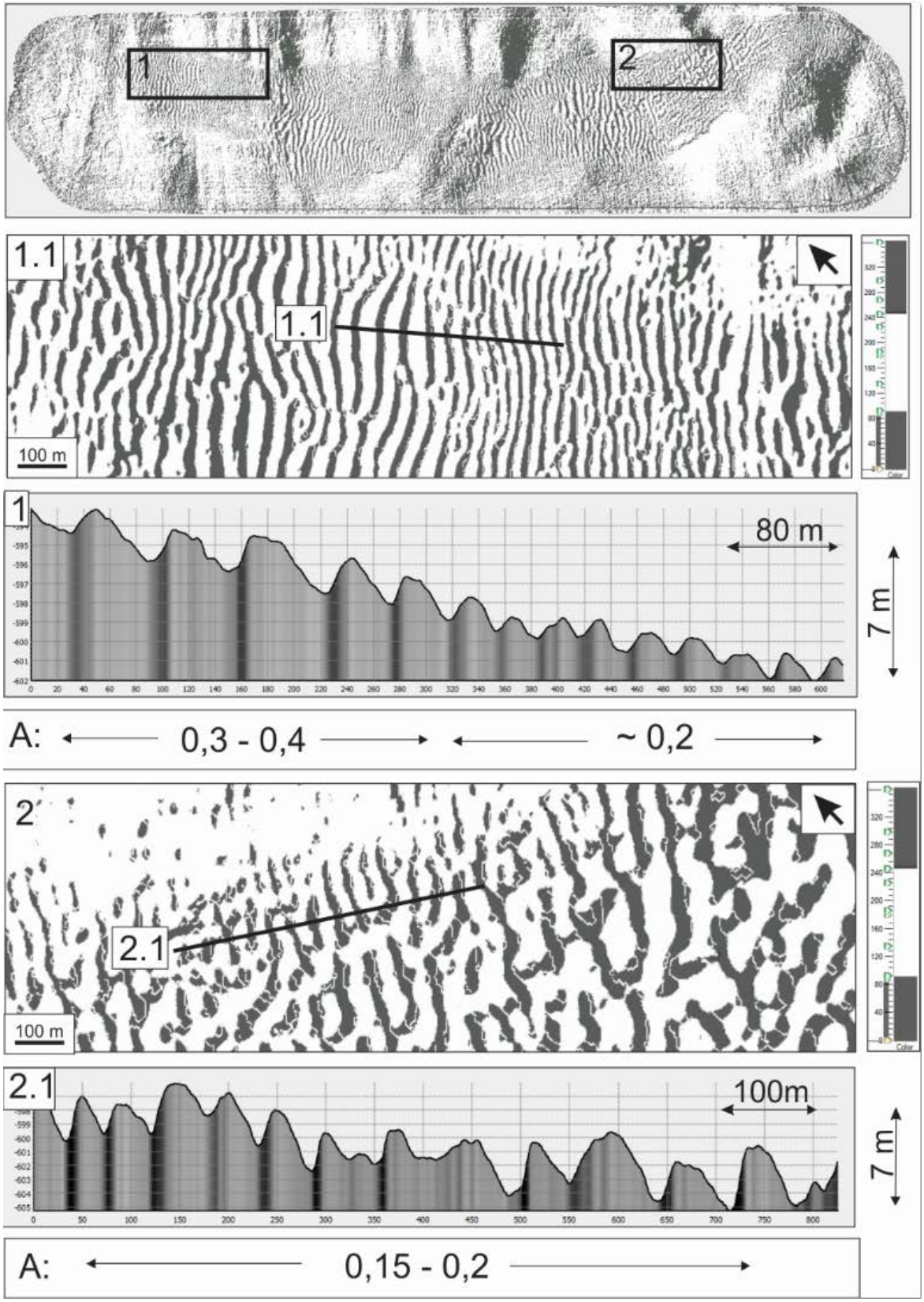

Figure 5.13: Dip azimuth map of the bathymetry showing the variation in asymmetry and sand wave size of two areas within the sand-wave field. There is an increase in wave height, wavelength and asymmetry towards the elevated area of figure 1, while figure 2 shows no correlation of sand wave geometry with elevation.

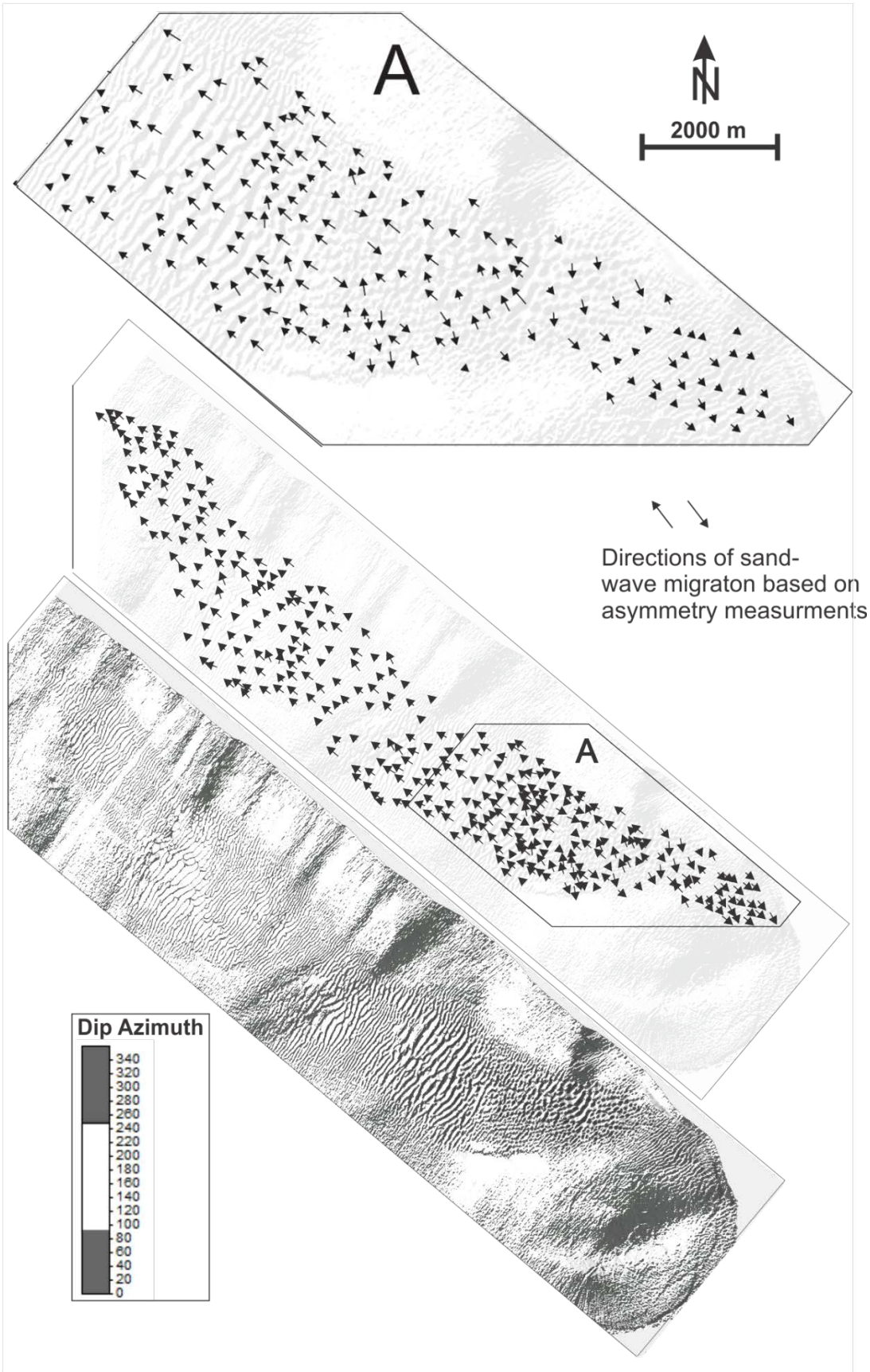

Figure 5.14: Interpreted directions of sand-wave migration based on asymmetry values (Dip Azimuth map, see also Figure 5.12), highlighting the large variation in asymmetry in the Southern part of the sand-wave field.

5.1.3 Migration rate of the sand waves

The three-year time period between the bathymetry surveys (2008 and 2011) made it possible to observe the actual displacement of the sand waves for this time period, and thereby attempt to calculate the real migration rates. These data also allowed comparing the migration with the inferred migration directions from the asymmetry map. A disadvantage of the bathymetry data in the programme Fledermaus was that the 2008 data were smoothed and the 2011 data were not. While I kept this in mind, I drew the lines from the two surveys in the middle of each sand wave. . Profiles of these data were prepared carefully and compared to each other (fig. 5.15). While exporting the data into Petrel, however, I was able to smooth the 2011 data as well so that the sand waves of the two datasets would get a more similar shape (fig. 5.16).

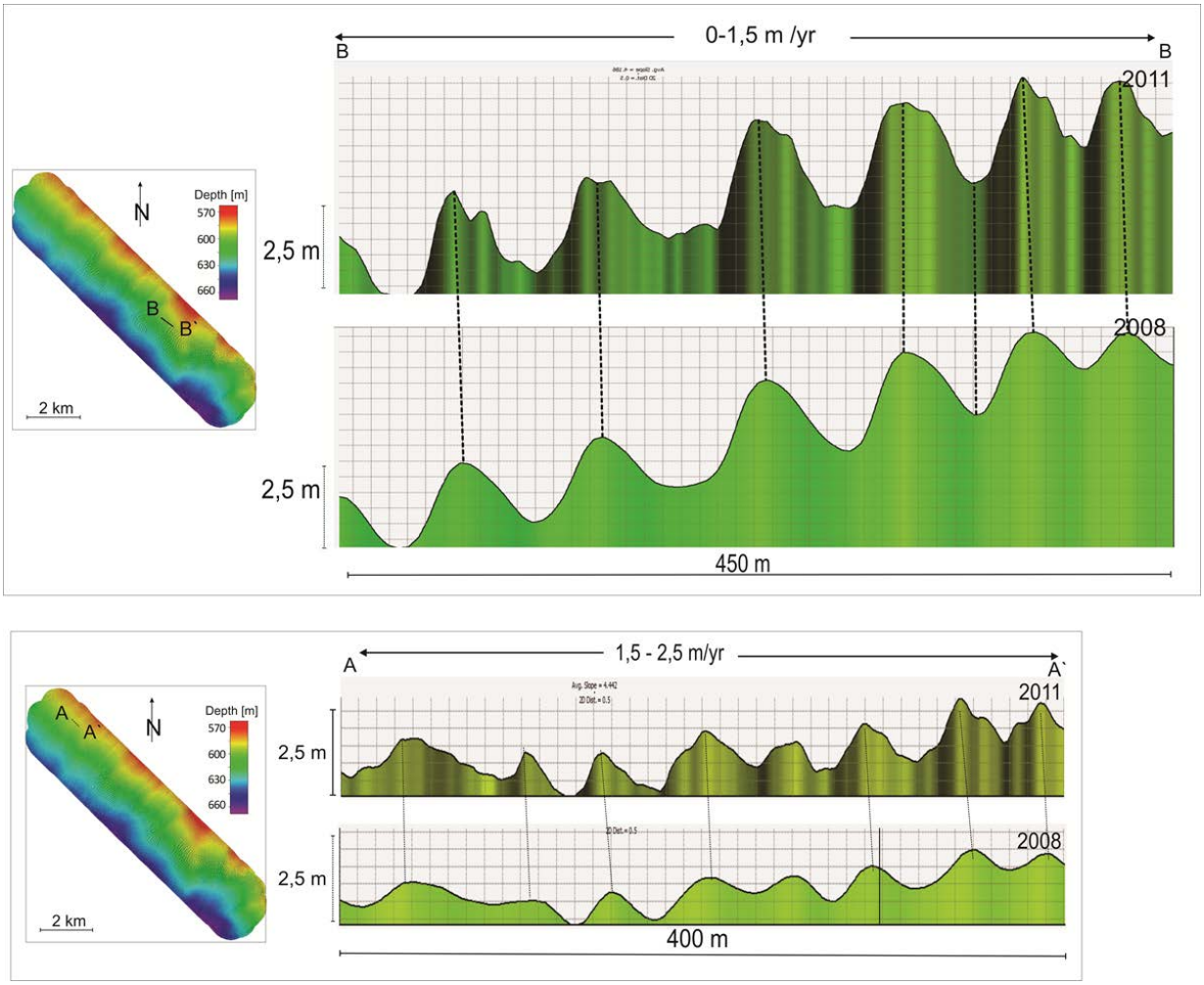

Figure 5.15: Migration of crest-lines of two different locations of the sand-wave field. The migration rates within the field are found to range from 0-3.3 m/year (0 – 10 meters for the three years' time period between the surveys).

Relative migration rates of the crest-lines were observed from overlapping max curvature maps for the two datasets (fig. 5.16). All curvature values except for those representing the crest-lines where made transparent by using the opacity function in Petrel. This generated an overview of the different migration rates across the sand-wave field. The map was later used to calculate the absolute migration rates by comparing the sand wave crest positions in a profile from the 2008 and 2011 bathymetric datasets.

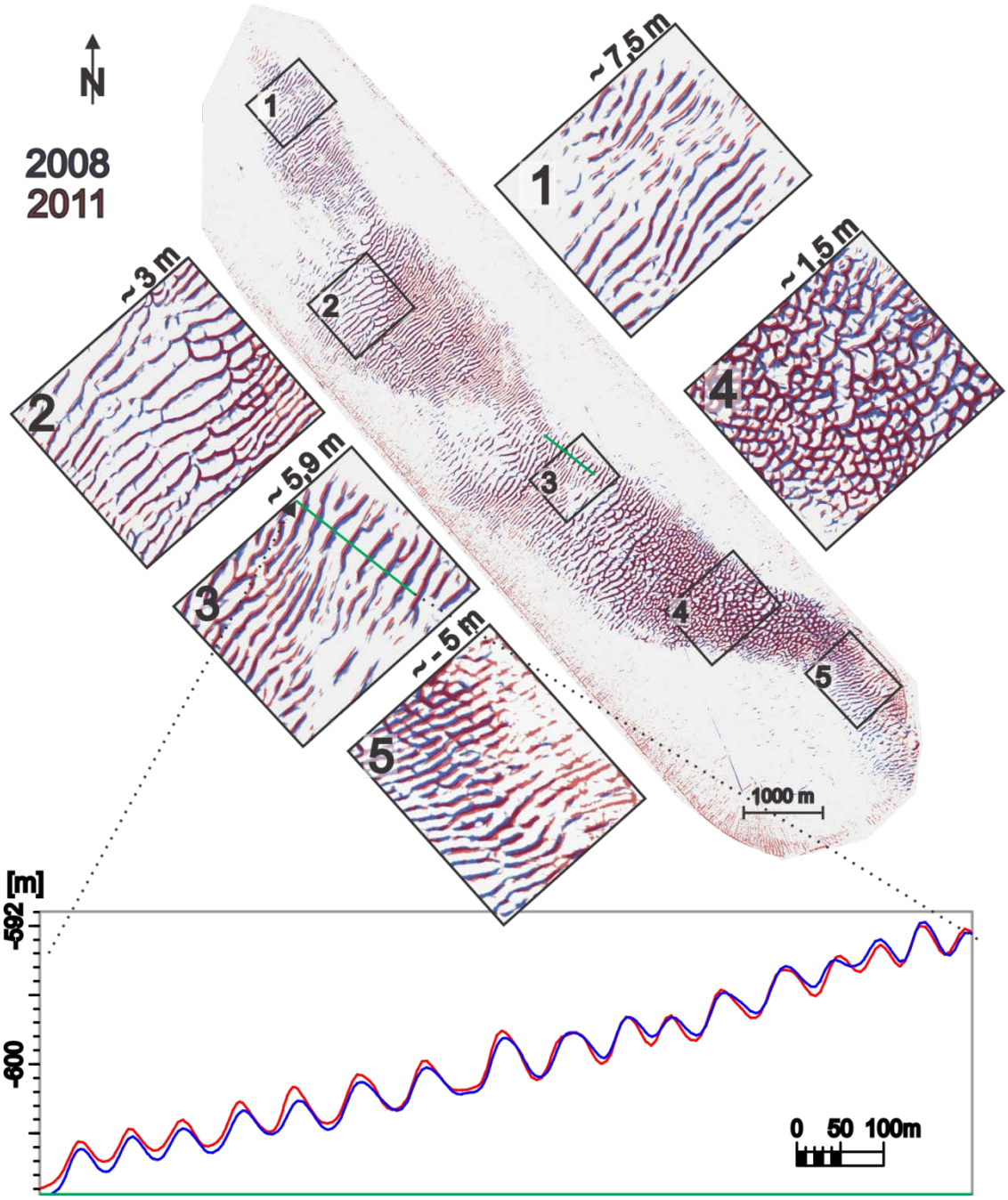

Figure 5.16: Displacements of crest-lines according to the two bathymetry sets from 2008 and 2011 over the study area (both surfaces are gridded with 5x5 m and smoothed to look as similar as possible). The lower figure is a profile of the two surfaces; the location of the line is indicated on the map above (close-up nr. 3).

The displacement of crest-lines of the sand waves according to the two maps (three year time gap) was largely 0 – 10 meters to the North West, indicating a migration rate of 0 – 3.3 meter/year in the same direction. On the southern tip of the sand-wave field, however, the displacement of the crest-lines were quite uniform to the South East. 1.8 – 7.5 meters displacement was measured, indicating a migration rate of 0.6 – 2.5 meter/year to the South East (ex. fig. 5.17).

None or only small migration rates in various directions are found within the Barchan-type sand waves in the South (just north of the southern tip) (fig.5.16). Especially, the largest barchans-type sand waves in south show an overall zero migration, while smaller sand waves on the margin of that field show a slight migration in various directions. In general, sand waves with smaller wavelength and wave-height seem to migrate faster than larger sand waves (ex. fig. 5.15).

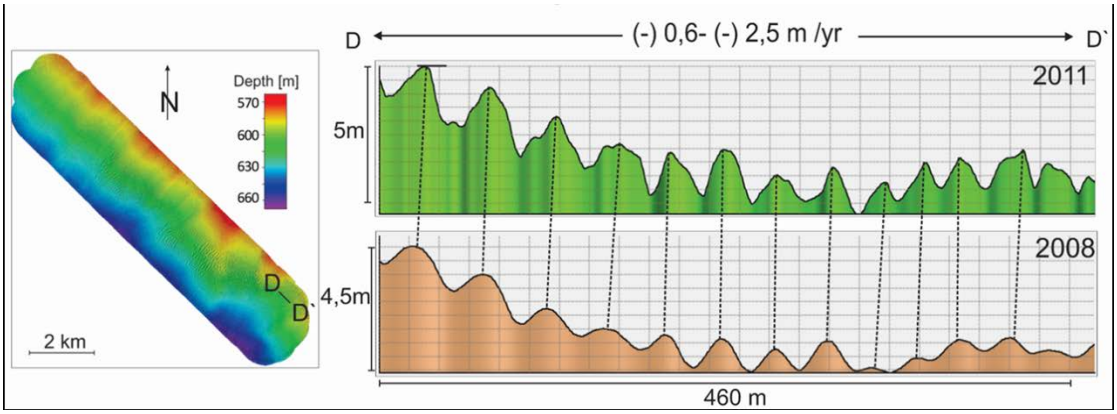

Figure 5.17: Example of "reversed migration" of crest-lines in the southern tip of the sand-wavefield. The migration rates within this area are found to range from -0.6-2.5 m/year.

It has been difficult to indicate the average migration rate for the sand waves since the displacement seems to be very variable both in the NW-SE and the NE-SW direction. However, I have indicated an average displacement value of the migration rates, i.e. 3-6 meters during the three year time period. This equals an average migration of 1.6 m/year, a value that has an uncertainty of ~ $\pm$ 0.2 m/year but provide the best attempt for further calculations (discussion chapter).

Unfortunately, depth shifts (due to different processing datum) of the two datasets in addition to smoothing of the 2008 dataset made it impossible to compare the height differences of the sand waves.

5.2 Seismic results

5.2.1 Stratigraphic correlation

The 3D seismic cube is located on the continental slope of SW Barents Sea, on the southern flank of the Bear Island Trough and within the middle-late Pleistocene succession.

In order to enable a stratigraphic correlation of the (3D) dataset, I linked the 3D seismic cube with a previously interpreted (2D) seismic line NH9702-234 (Deryabin, 2012), located ~20 km north of the seismic cube. This correlation was performed by tracking the R1 reflector, representing the base of the middle-late Pleistocene succession or unit GIII, to adjunct 2D seismic lines of dataset NH9702, NH8401 and in the direction of the study area (fig. 5.18). The clear reflector appears in the 2D seismic line at approximately 660 m below the seabed. A more transparent zone at ~100 ms is present above the reflector, and the underlying reflectors are truncating it. Further to West on the Continental Slope the reflectors underneath horizon R1 are more parallel with R1. The R1 reflector in the 3D seismic data appears as a weak reflector that is sporadically present in the 3D seismic cube.

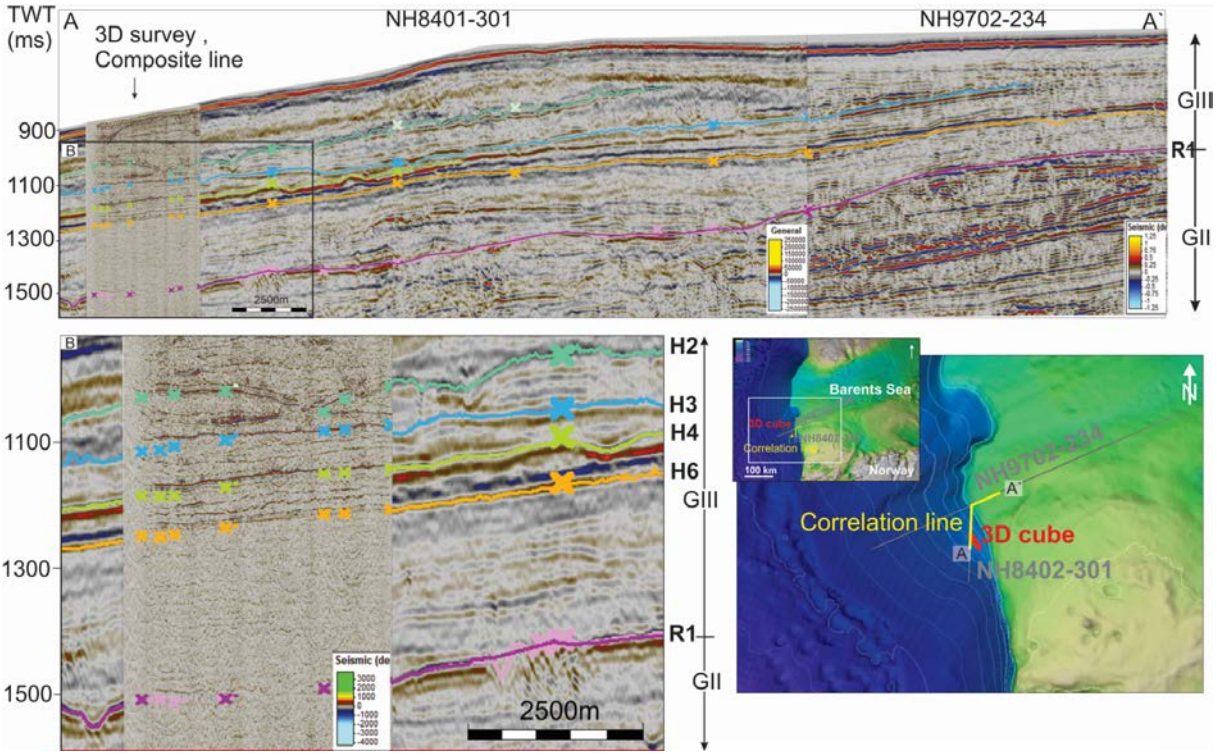

Figure 5.18: A) 2D seismic line (NH8401-301 and NH9702-234) from shelf to slope overlain on an equivalent seismic line of the 3D survey with interpreted horizons. B) Figure shows an enlarged area of (A) where the composite line of the 3D survey is located. Location of the line is seen in the depth map to the left of SW Barents Sea. The regional reflector R1 is previously interpreted by Ryseth (2003) and Andreassen (2004) in the area and used as a reference.

Above the regional R1 reflector, I interpreted seven of the most prominent and continuous reflectors in the 3D seismic cube (fig. 5.19). The seabed horizon is called SB, and the horizons below that are called H1-H6, from top to bottom. The units within the horizons are called U1-U6. Two semi-continuous reflectors within the unit U6 have also been interpreted, and called DBF1 and DBF2 (not visualised in the figure 5.19).

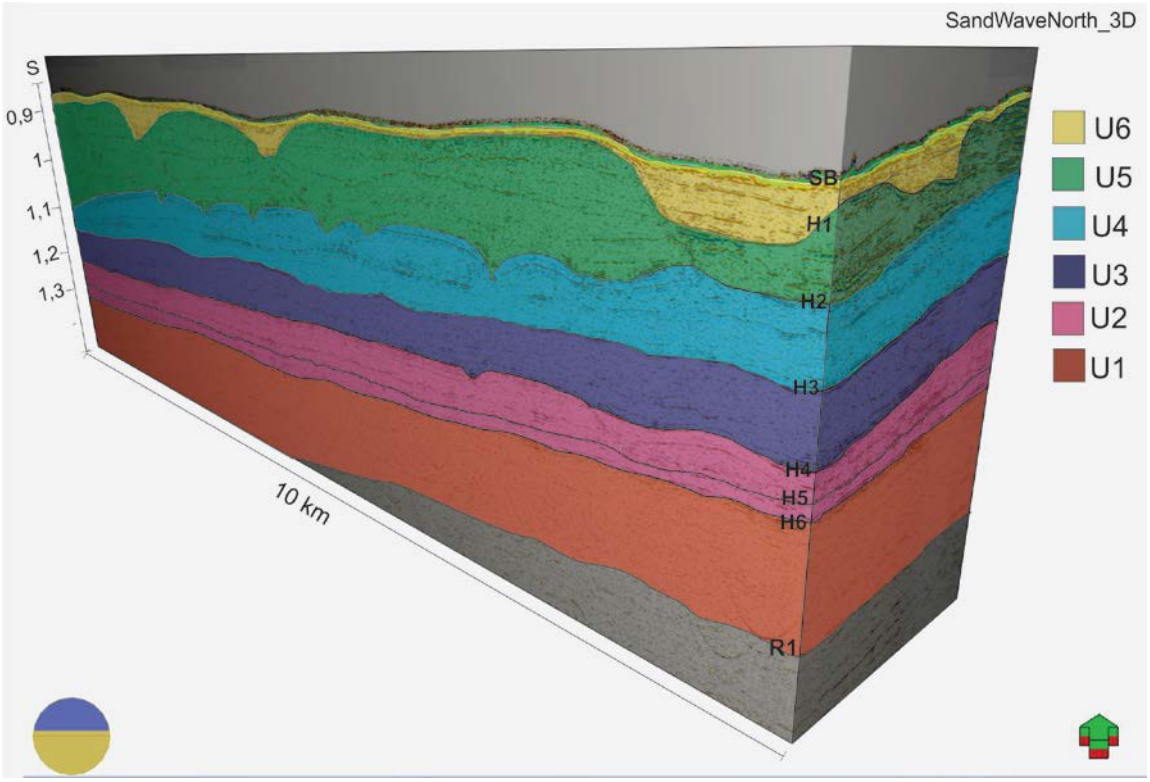

Figure 5.19: 3D-image of the 3D survey "SandWaveNorth_3D" seen from SW with interpreted horizons and units.

Some studies have described subunits within the GIII unit (Vorren et al., 1991, Sættem et al., 1994, Sættem et al., 1992, Vorren et al., 2011, Laberg and Vorren, 1996, Vorren and Laberg, 1997, Andreassen et al., 2007), but the study areas of these works are located either further east on the continental shelf or in deeper areas further NW, and therefore were influenced by a different depositional environment. Further east on the shelf, most of the GIII has been eroded away by the last ice sheet, or partly eroded away such that the subunits within the GIII unit are discontinuous (Vorren et al. 1991). Lack of (2D) seismic reference, - and correlation lines make it also difficult to correlate to other works further northwest on the slope. Sættem et al., (1992) and Laberg and Vorren (1995) focus on the Upper Cenozoic glacial geology of the outer Bear Island Trough and develop a stratigraphic age model. Although the study area of these works is to the NE of my study area, I use their interpretation as a first-order attempt to develop age assignment of the prominent horizons within my study area.

Laberg and Vorren (1995) use high-resolution seismic and sparker data across the entire upper part

of the Bear Island Trough Mouth Fan (TMF), from 71 – 75 degrees north and 10 – 18 degrees east to evaluate the evolution of the TMF. They identified several reflectors that seemed to run through the entire area. The reflectors are suggested to reflect interstadial/interglacial times when the ice cap and associated ice stream were not present, an assumption that is supported by most works regarding glacial sediments (Vorren et al., 1989, Sættem et al., 1994, Sættem et al., 1992, Laberg and Vorren, 1995, Sejrup et al., 2005, Vorren et al., 2011) . Although the thickness of the sediment package between different horizons varies significantly across the trough mouth fan (fig 5.20), it has been shown that these reflectors are continuous over areas > 300 km2 (cite).

By tracing 2D seismic lines from my study area to their study area (Laberg and Vorren 1995; Sættem et al. 1992), I have done an attempt to correlate my reflectors with relatively high uncertainties. Uncertainties exist north of my study area where a ~50 km wide slide-scar divides the stratigraphy between the North and South. Therefore, I had to follow reflectors from the slope to the shelf and back down to the slope in order to trace continuous reflectors. Figure 5.20 presents 5 snapshots of the interpretations (including one each of Laberg and Vorren (1995) and Sættem et al., 1992) with locations, to give an idea of how the correlation was established. The base horizon shown in the map window is the interpreted regional R1 reflector. Correlation close to the study area presented in figure 5.21 is highlighting the 2D seismic and 3D seismic expression of the unit. The suggested correlation is shown in table 2.

This work	Sættem et al. (1992)	Laberg and Vorren (1995)
U6	G	Isotope stage VIII 2
U5	F <30 ka <130 ka	VII 24-12 ka 2
	D2 <200 ka	VI 194-128 ka 6
U4	D1	V
U3		313-258 ka 8
U2	C <330 ka	IV 386 - 359 ka 10
U1	B <440 ka	III II I 622-589 ka 16

Table 2: Correlation of seismic stratigraphy done in this work.

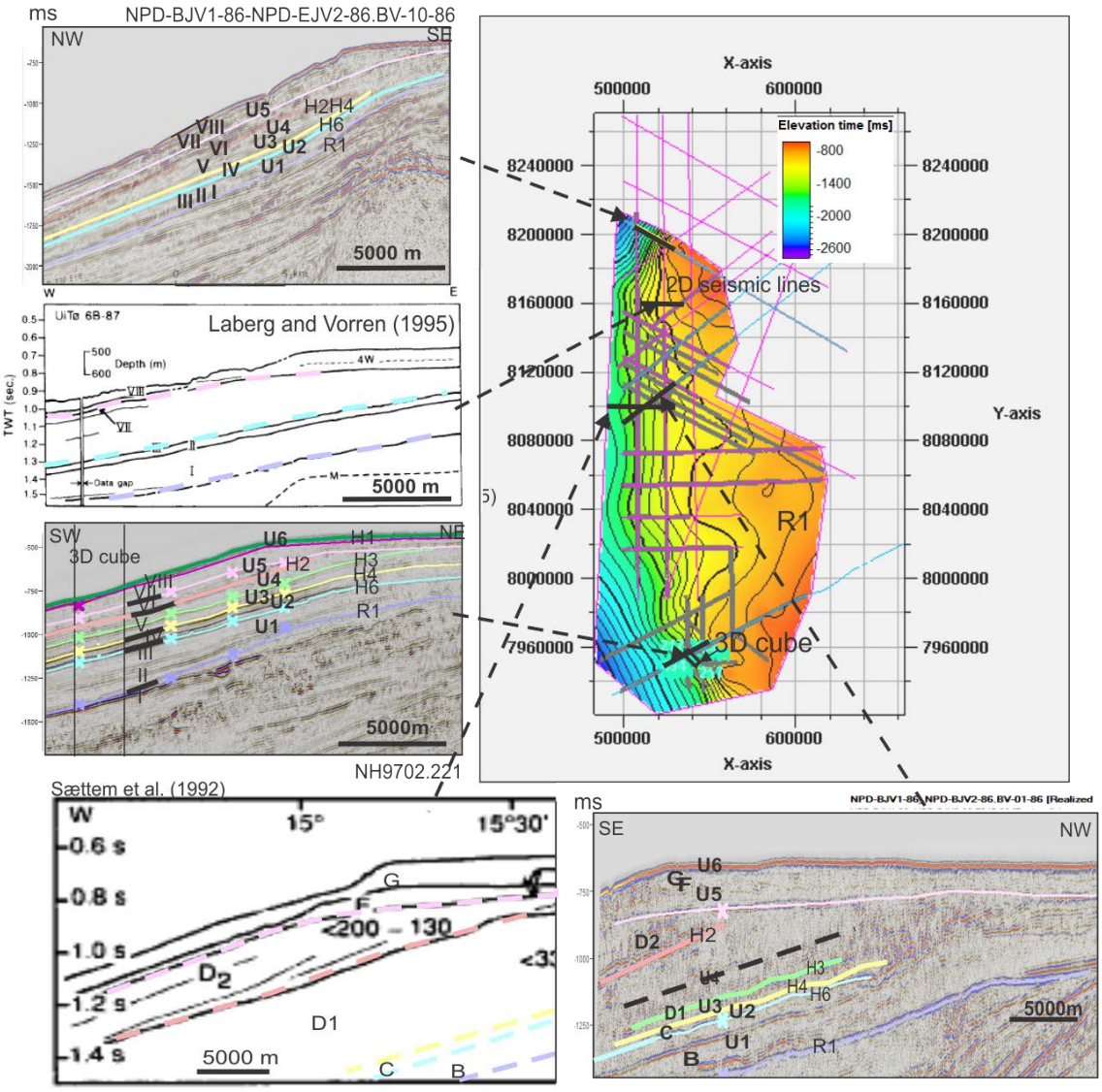

Figure 5.20: Earlier Interpreted subunits within the middle-late Pleistocene succession (Sættem et al. 1992 and laberg and Vorren, 1996) with seismic examples (table 2).

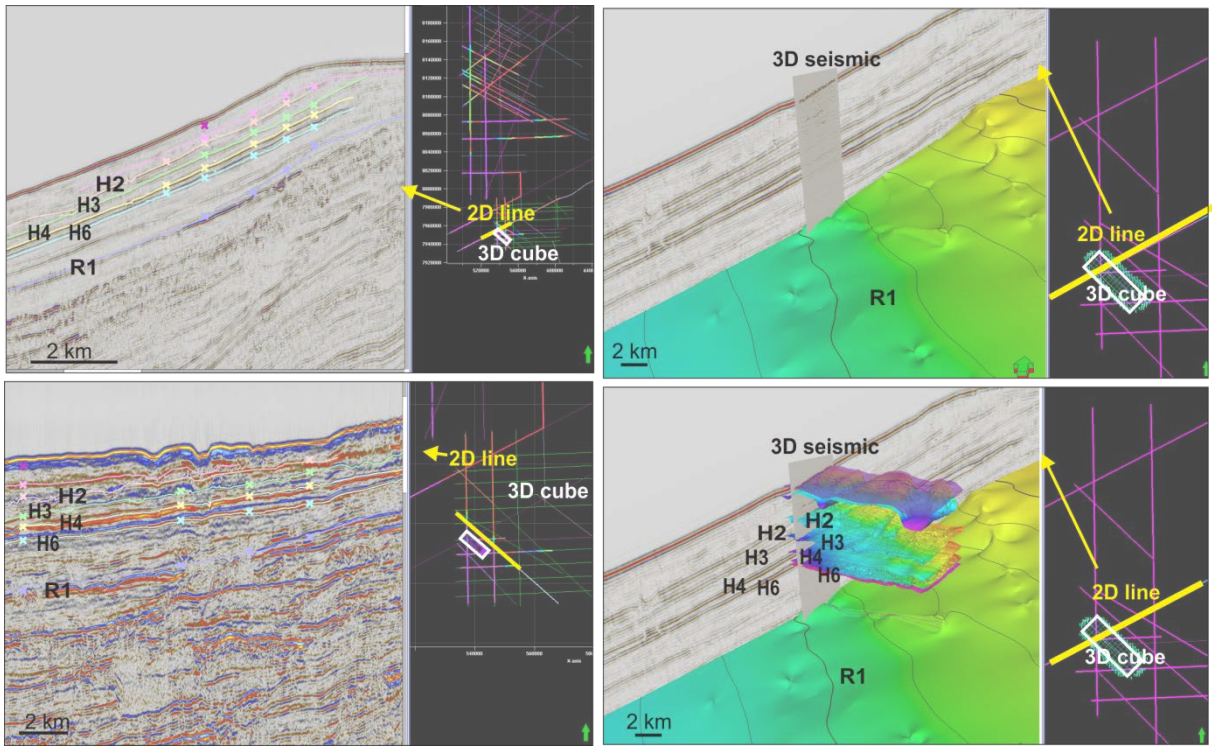

Figure 5.21: 2D seismic lines with the interpreted horizons close to the 3D seismic cube, showing the appearance of the interpreted seismic reflectors in some of the 2D seismic lines. Location of the 3D seismic cube in relation to the seismic lines is given to the right of the figures.

The correlation indicates that 3 horizons in SandWaveNorth_3D, H2, H4 and H6, may be the same horizons as the reflectors of Sættem et al., 1992, who label their horizons unit F and D2, D2 and D1, and D2 and C, respectively (fig. 5.20, bottom to seismic sections). These reflectors can further represent the (VII/VI (H2), VI/V (H3) and IV/III (H6) reflectors of the study of Laberg and Vorren (1995) (fig 5.21, seismic sections to the left in the figure).Unit D1 and C, besides one smaller glacimarine unit between D2 and D1, are glacial deposits, as indicated by core data, and they reveal a thick succession on the outer shelf and upper slope. The glacimarine unit on the interface of these units may represent three parallel and continuous reflectors that we observe in this 3D seismic cube, located on the base of unit U2.

5.2.2 Seismic units

In the following, I will describe all the sedimentary units that I have interpreted in the P-Cable 3D seismic data (Fig. 5.19), proceeding from the top-most to the bottom-most unit. A water velocity of 1500 m/s and a sediment velocity of 2000 m/s are used for conversion from seismic two way travel-time (TWT [ms]) to depth (m) in the seismic section. The acoustic sediment velocity used is from Fiedler and Faleide (1996), where a velocity-depth gradient plot has been made for the Cenozoic sediments. The average velocity of unit GIII was here estimated to be 1970 m/s; and I used an average velocity of 2000 m/s (this should be acceptable since the maximum depth differences between the use of these two velocities equals only 9 meter (from seabed to the base of unit U1).

5.2.2.1 Unit U6

Description of unit U6

The seabed reflector occurs as the uppermost zero-phase (trough amplitude) reflector, located between 790 and 880 ms TWT, - corresponding to a depth of 592 - 660 m.b.s.l. A zero-phase trough reflector represents an increase in acoustic impedance and is the normal polarity reflector of the dataset. Figure 5.22a shows a depth map and an example of the seismic reflector and the interpretation of the seabed and the underlying horizon H1. Two events made it challenging and time-consuming to interpret the seabed. (1) In the area of sand waves, the seabed appears in most places as stacked reflectors (especially where the sand waves are large and have a steep lee side dip). This phenomenon made it difficult to determine and interpret the exact position to move the reflector down to the troughs of the sand waves. (2) Diffraction events occur in the seismic data above the reflector. These phenomena are seen in figure 5.22a (B-B`), which presents the horizon within the area where sand waves are located.

As also seen in the bathymetry data of the seabed, sand waves with crests perpendicular to the contour-lines are located on top of a channelized bed, where the channels are oriented down the slope in a sinuous shape. The seismic example in figure 5.23 shows that the sand wave horizon is present as a wide, stacked seismic reflector above the sand-wave field. The stacked layer also becomes wider with sand wave size. Comparison of the seismic seabed and the bathymetry seabed is discussed in chapter 6 (discussion chapter).

The base of unit 6, presented as horizon H1, is interpreted to be the first prominent reflector appearing beneath the seabed. It shows as a negative reflector (increase in acoustic impedance) on the higher elevated areas between the depressions, and as a positive reflector (decrease in acoustic impedance) in the depressions. The horizon is generally dipping towards SW and is characterized by the three channels appearing as v – shaped, gently sinuous elongated depressions that are oriented

in a SE/NW direction (fig 5. 22a (D)). The depressions are 1000-2000 m wide with the widest part furthest to the SE (down the slope) and up to 50 m deep. The levees of the depressions appear to be highly erosive, though deeper layers are cut off by the horizon where the depressions are located.

The seismic data reveal a deeper horizon (H1) that represents the base of the channels, which are observed on the seabed (SB) (fig.5.22a). This statement is confirmed by matching contour lines of horizon H1 and the seabed SB (fig 5.22b). Unit 6 compromises therefore the channel fill (chaotic and weak reflectors) of the uppermost channelized bed, located between the seabed reflector, SB, and horizon H1 in addition to the draping sand layer where the sand waves are present. The thickness of the unit is between 0 and 53 meters, but is on average only 14 meters. On the elevated heights, however, the thickness of unit U6 is as small as 0 – 10 m. At locations where the seabed reflector (SB) and the reflector of horizon H1 meet, the superimposed sand waves are also lacking. These observations may suggest that the sand waves migrate on the most elevated parts of the channelized horizon H1, and where the channels are located, on top of the channel fill of Horizon H1.

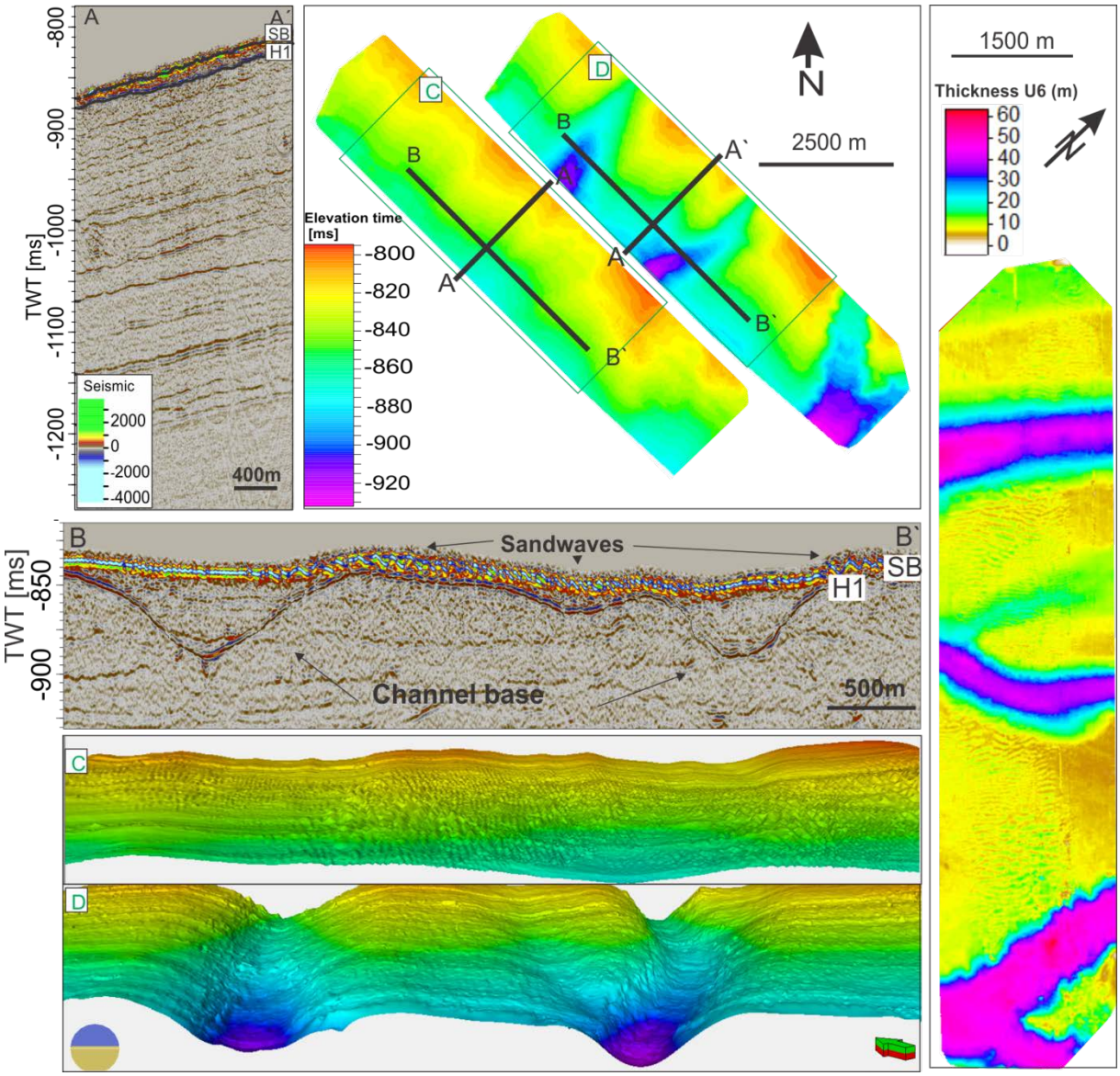

Figure 5.22a (left figure): Cross-line A-A` shows the stratigraphic location of unit U6 between the seabed (SB) and horizon 1 (H1). B-B` indicates the seismic expression of the two boundary horizons. The windows labelled C and D in the figure show 3D-views of the seabed (SB) and Horizon H1, respectively; seen form SW. The locations of A, B, C and D are given in the upper right corner, where both of the horizons are also shown from a map point of view.

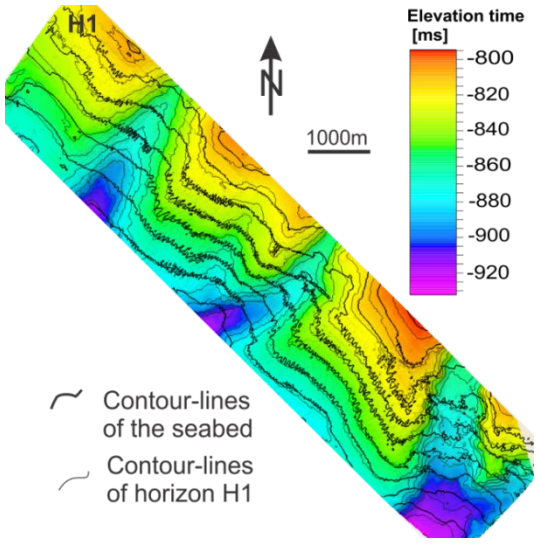

Figure 5.22b (right figure): Contour-lines (thick black lines) of the seabed reflector on top of a time-depth map of Hoeizon H1 (the contour-lines of this horizon is presented with the thin black lines), illustrating the same trend in contours of the two surfaces.

A minimum amplitude map (derived from a window of 1 ms above and underneath the interpreted seabed to account for small miss-picks) of the seabed horizon shows changing amplitude values across the sand waves (fig.5.23). No amplitude variation is seen related to depth and topography of the underlying channelized seabed; the variations in reflection strength seem to be restricted to single sand waves (obviously excluding the seismic artifacts occurring in the inline direction). The amplitudes are varying from crest to through, where higher values are typically on the wave-tops and in the middle of the troughs. Due to this variation of amplitude strength, the nature of the sand waves becomes clearly visible in an amplitude map (see fig.5.23) and a seismic volume render (see fig. 5.24).

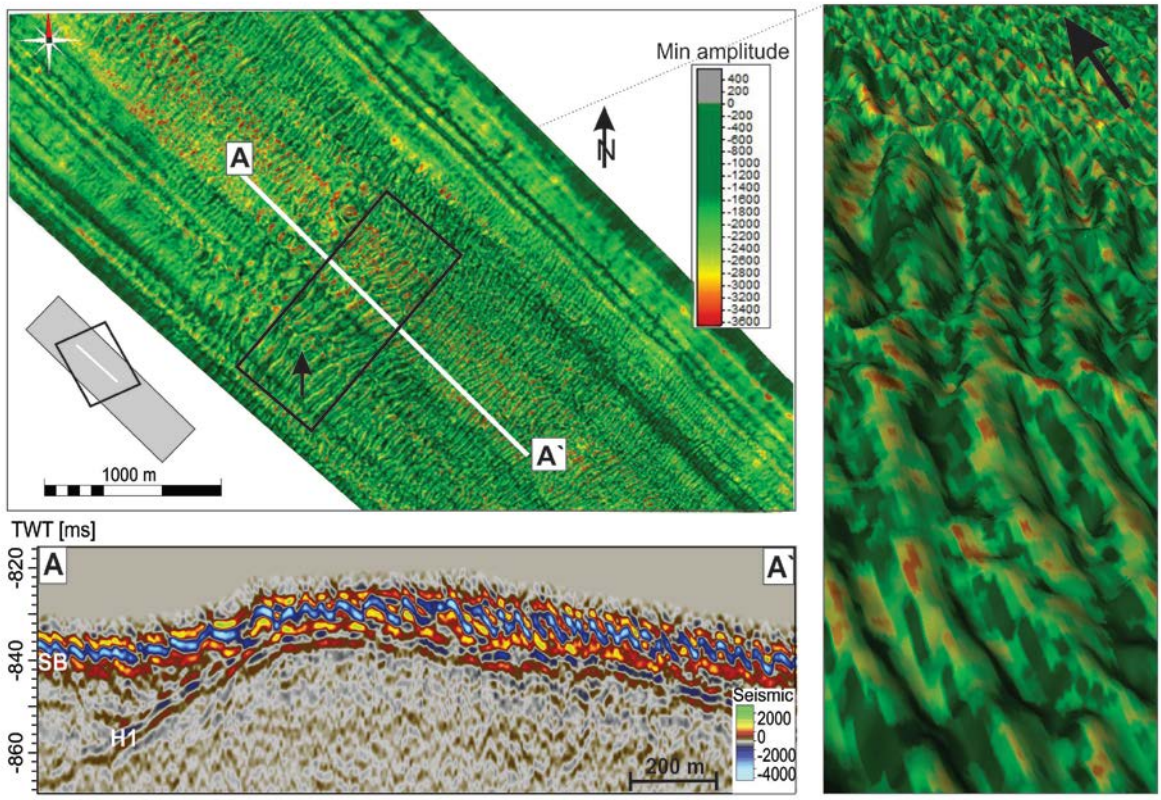

Figure 5.23: Minimum amplitude map and a seismic profile of the seabed showing the distribution of amplitudes across the sand waves. Red and yellow amplitudes represent high values. As seen in the close-up of the 3D window of the amplitude map to the right, high values are present on the gentler stoss-side and in the troughs of the sand waves.

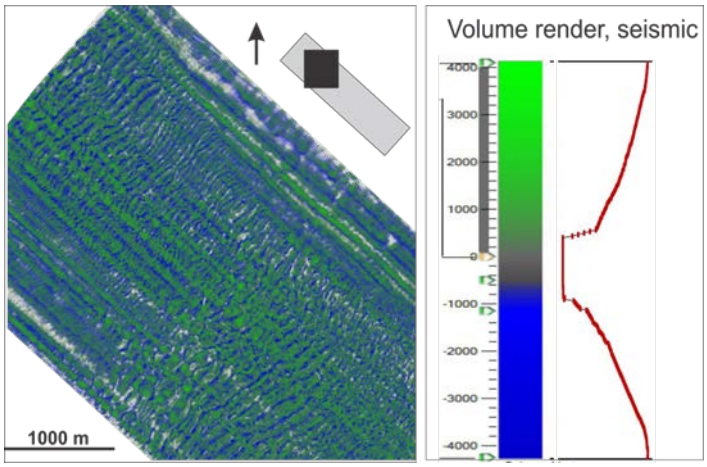

Figure 5.24: Seismic render volume of the seabed – showing only the high amplitudes. The characteristics of the sand waves become clear in such a volume.

Stronger negative acoustic impedance reflectors are observed on mean and max amplitude maps on the elevated highs of the horizon and as thin bands inside or just beneath the middle of the large channels (fig. 5.25). Due to the location, these features highlight the base of the channels. The mean amplitude tends to be around zero on the channel-walls.

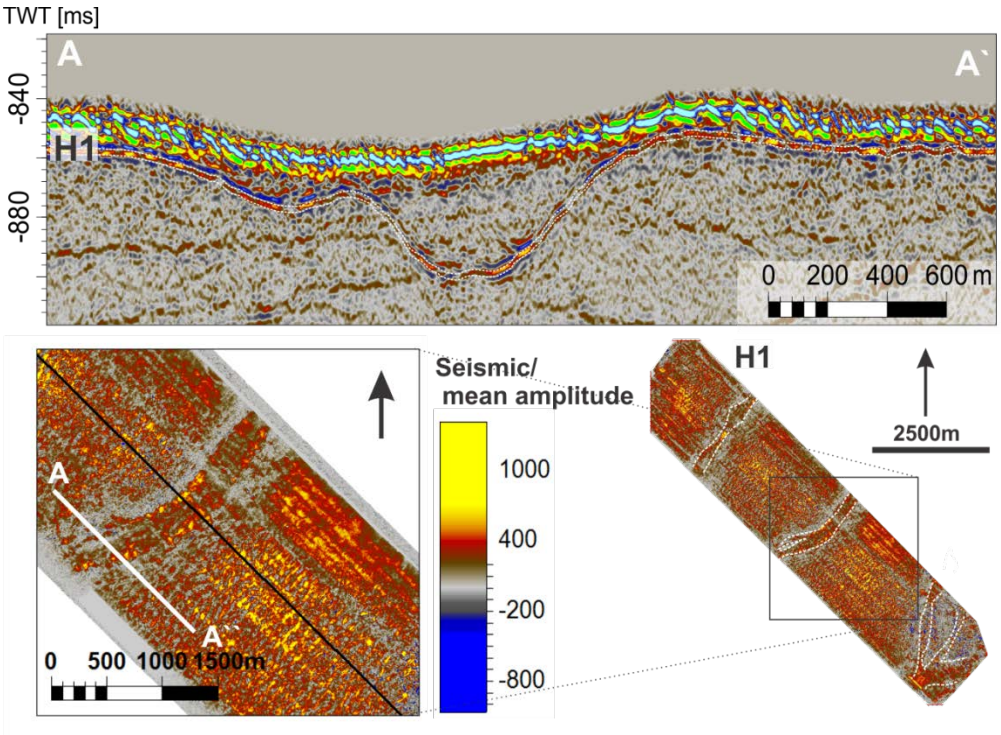

Figure 5.25: A-A`) Seismic inline highlighting amplitude variation of horizon H1. Variation in amplitude across H1 surface (snap-shots in the lower half of the figure) represented by a mean amplitude 1ms above and underneath the interpreted horizon, as indicated by the white stippled lines in the seismic profile. Higher amplitude values are observed inside the depressions and on the elevated areas.

Indications for older sand wave generation or relicts do not appear to exist in U6. The sand waves occurring on the seabed seem to be the only sand waves apparent within the top layers, indicating the present sediment transport.

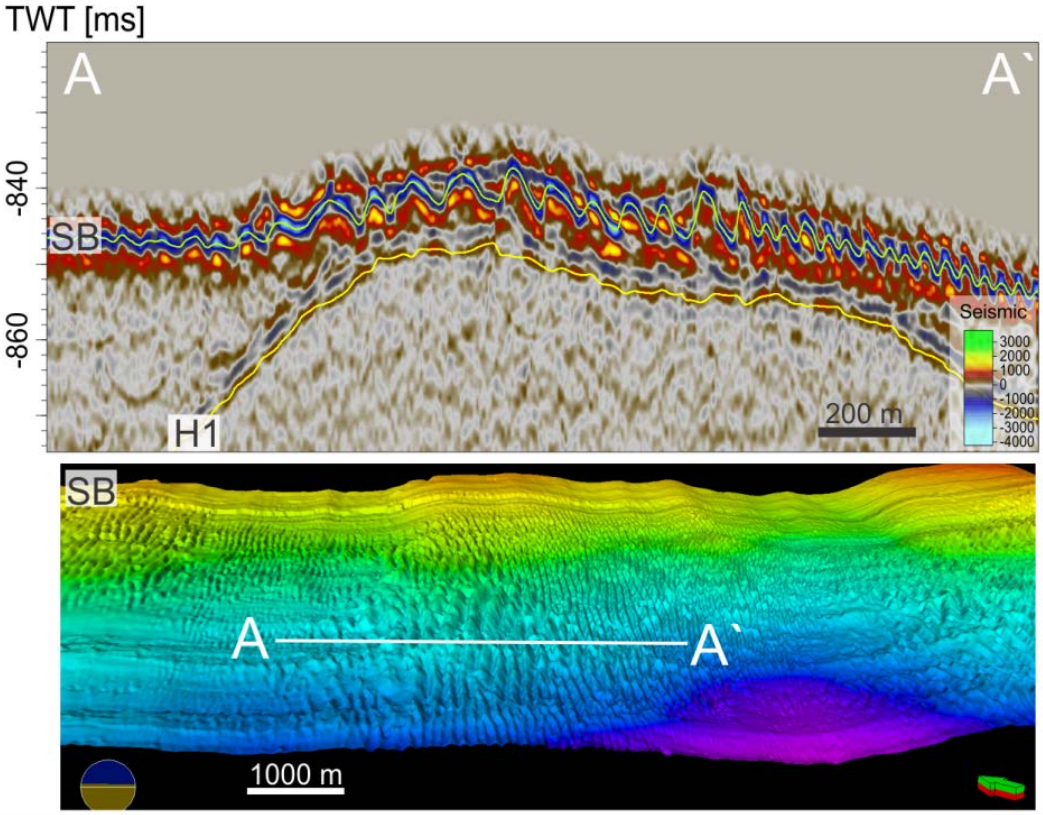

Figure 5.26: Close-up of the middle area of the seismic seabed and an associated seismic profile (A-A`), illustrating the one generation of sand waves apparent in the sand-wave field.

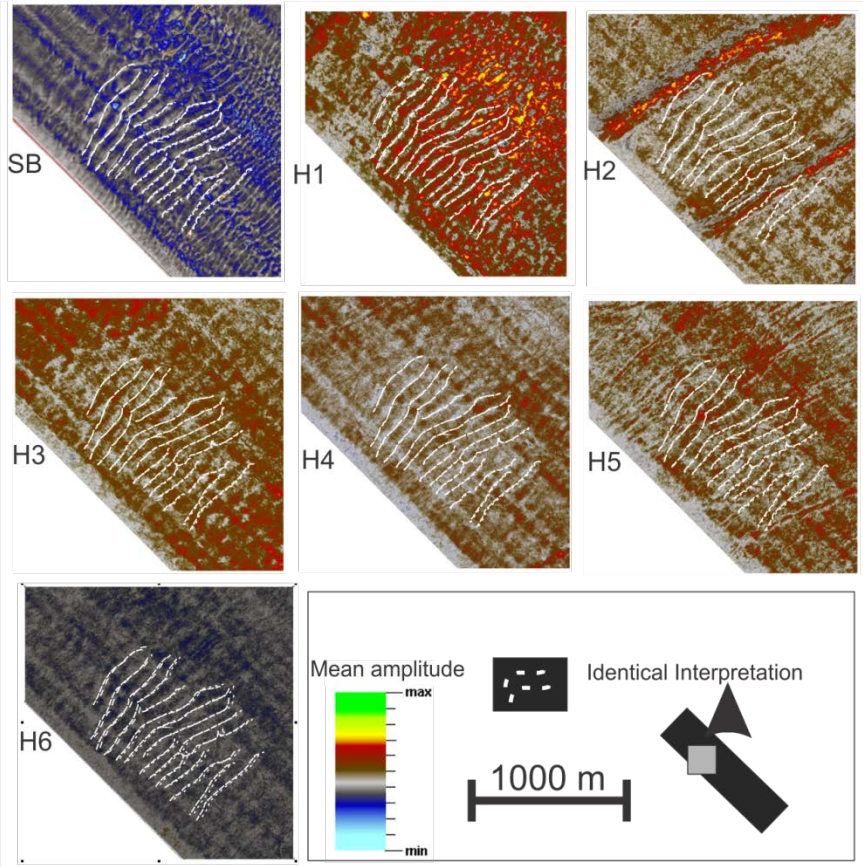

Figure 5.27: Zoom inn of mean amplitude maps of the same area of all interpreted horizons. The figure points out identical interpretations of amplitude patterns, indicating that this is amplitude noise form the seabed rather than indications of subsurface sand waves.

Interpretation of unit U6

Due to the v-shaped form of the channels and the classification scheme of Stow and Mayall (2000), I infer the imaged topographic depressions to be slope canyons. These features are common on continental slopes around the world (Twichell and Roberts, 1982, Sejrup et al., 2005), and are often connected to glacial margins. The major formation mechanism of slope canyons is thought to be density/turbidity currents or underwater landslides (Stow and Mayall, 2000).

The amplitude distribution of the seabed (fig. 5.23) may reflect variations in particle grain sizes across single sand waves. The larger amplitudes in the sand wave troughs can potentially reflect coarser material (King et al., not publ.), or they can reflect the underlying glacial material rather than the sand wave horizon, if the sand-layer becomes thinner than the tuning thickness for detecting seismic reflections in the data (1-2 meters).

Another explanation of varying amplitude may be due to seismic behavior of dipping reflectors. On a dipping ground (above the dip of the radiation wave front) or for anticlinal structures, the reflection traces become fewer than, for example, on horizontal reflectors or synclinal structures. The result after processing but before migration is that the seismic data generally have smaller reflection

strengths above such events (dipping ground or anticlinal features). The energy is spread along diffraction hyperbolas. This phenomenon is called the bow-tie effect and is illustrated in figure 5.28. Migration could resolve this problem. However, the P-Cable data is acquired at almost vertical incidence with a relatively low, uneven fold over an extremely wavy surface. That might have resulted in that the bow-tie effect could not have been completely removed.) The close-to-zero reflectors on canyons-walls are common phenomena in the seismic on surfaces with relative steep dip; the steeper angle of reflection gives a generally weaker reflection signal and at a non-horizontal surface causes the geometric spreading to be higher. This phenomenon could also potentially explain the amplitude variations of Horizon 1 (H1), with lower amplitude reflectors on the channel-walls (fig 5.25).

The negative acoustic impedance zones in the middle of the canyons could also indicate lower velocity or density zones in the canyon-fill than in surrounding sediments. High acoustic impedance is typical of sand-rich deposits whereas low acoustic impedance may denote a mud-rich system. Anomalous seismic amplitude can be associated with lithology changes (Rijks and Jauffred, 1991; Chen and Sidney, 1997).

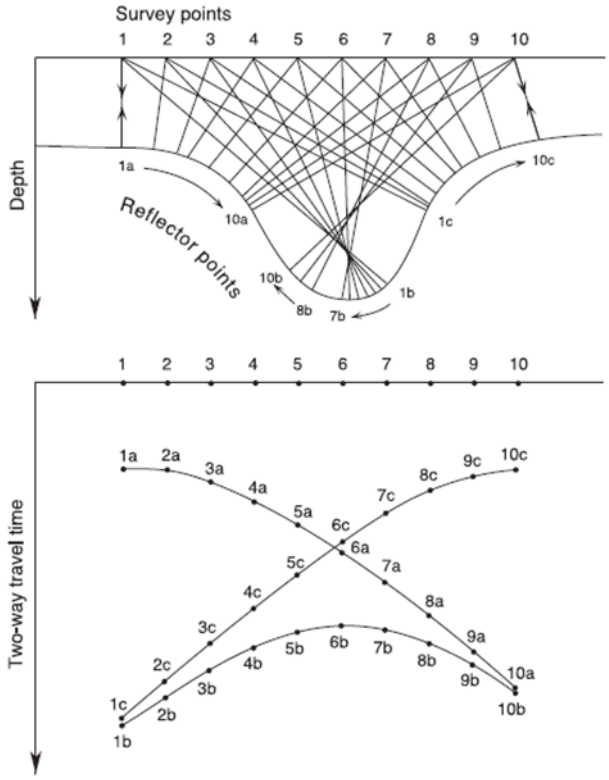

Figure 5.28: Illustrated the principle of the bow-tie effect. On a dipping ground exceeding the radiating wave front, the reflection pattern becomes complex.

Stronger currents on higher elevated areas are associated with coarse grained lag-deposits (fine grained sediments are eroded away) in a study of Tromsøflaket, just east of my study area (Bellec et al., 2008) and in the Troms II area, offshore Northern Norway. This may be the nature of the elevated highs of H1; causing increase in acoustic impedance (fig 5.25).

5.2.2.3 Unit 5

Description of unit U5

Unit U5 is 30 - 214 meters thick and on average 124 meter thick (assuming an acoustic sediment velocity of 2000 m/s), located between horizon H1 and H2 (fig 5.29), two high amplitude erosive but continuous reflectors. Weaker discontinuous reflectors exist between H1 and H2. Fig 5.29 presents a snapshot of the unit with interpretation of reflectors within the unit. Anomalously high amplitude V-shaped features, 20-100 m wide, appear frequently within unit U5 (fig. 5.30). They have a slightly sinuous shape seen from above, and cross the entire area in x-line (NE-SW) direction. The structures also tend to have a stacked occurrence, that means that two or more of these structures are often located on top of each other's with a slightly lateral shift (ex. a-a`, fig. 5.30).

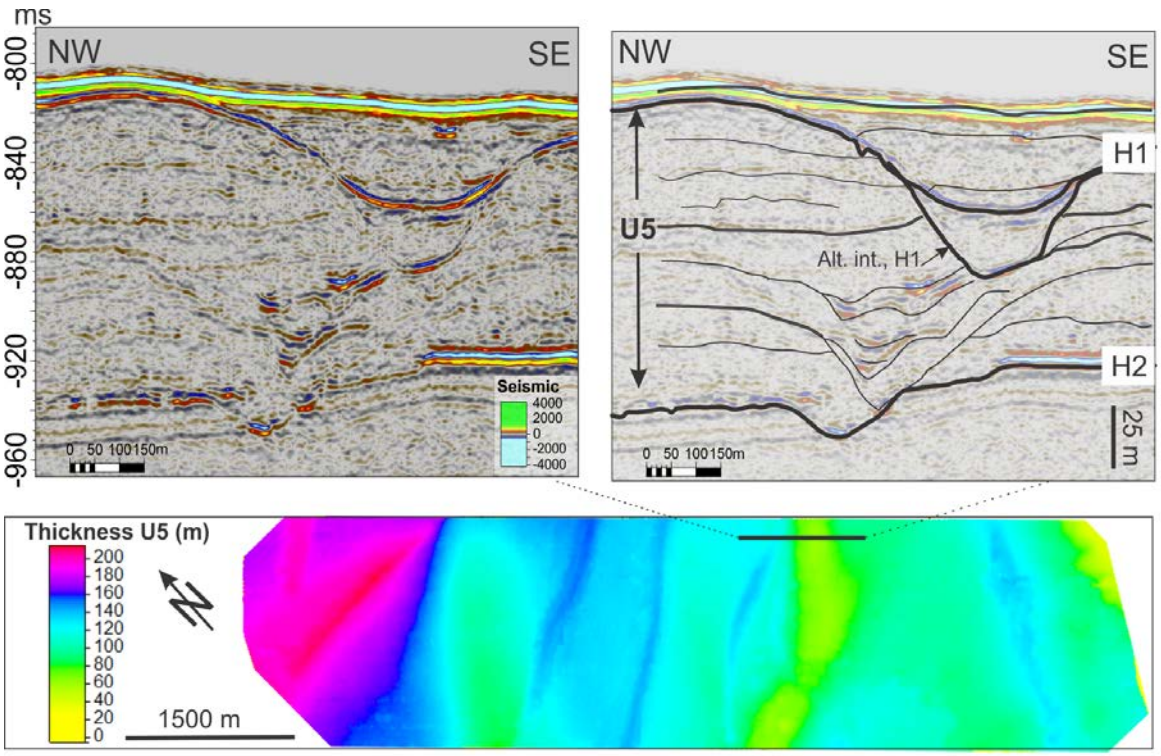

Figure 5.29: A seismic profile without (to the left) and with interpretation of substructures within unit U5, showing indications of several generations of synclinal erosion features cutting through horizontal layered deposits. Location is given in the upper right corner.

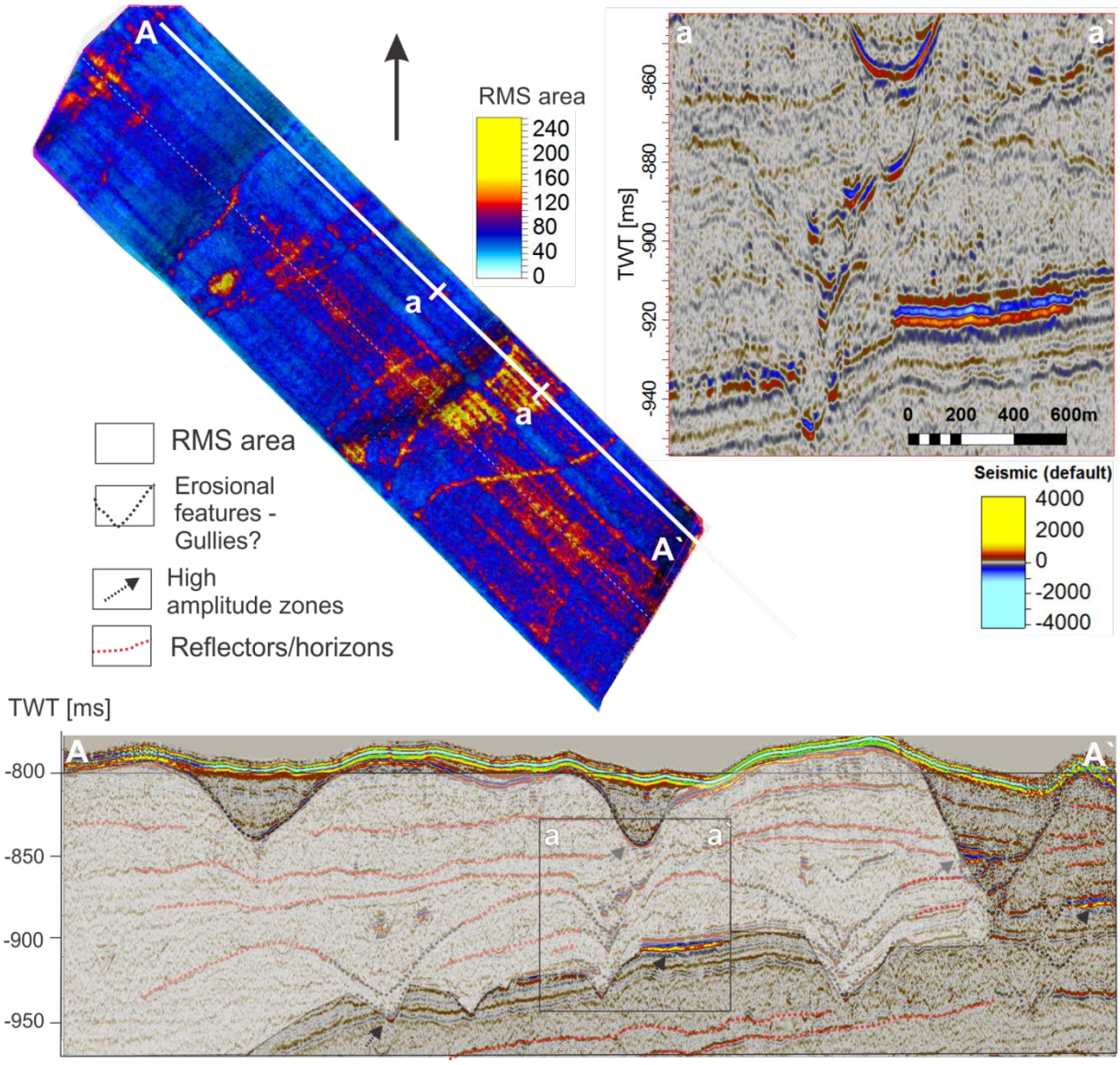

Figure 5.30: Presents a surface to surface RMS map from Horizon H1 – Horizon H2 (Unit U5). The window is, however, down-shifted from H1 by 2ms to exclude the amplitudes of this horizon. (A-a-a`-A) presents seismic examples of the high-amplitude features highlighted in the RMS map. The transparent white area of the seismic section indicates the area of the RMS amplitude map. High amplitudes are present as V-shaped, NE-SW crossing features within the unit.

Two of the weaker reflectors within unit U5, called DBF1 and DBF2, were also mapped, and are presented in figure 5.31 and 5.31. DBF1 highlights two mound-shaped horizons providing erosional evidence (layers are truncating the horizon). The mounded features are about 2000 m wide, and have an elevation change of 140 meters. The internal structure of DBF1 and between DBF2 and DBF1 is chaotic and transparent (fig. 5.31 and 5.32). The only higher amplitude reflections seem to come from the V-Shaped depressions described above, some located between DBF1 and DBF2. Between the two mounds, the reflector penetrates down into a gully of horizon H2. 100 m above this spot a complex pattern of high amplitude gullies are located. As seen in fig.32, the thickness between DBF1 and H2 is decreasing down the slope (SW). DBF2 is a flatter horizon than DFB1, something that seems to be because it has not been influenced by erosion after deposition (fig. 5.32).

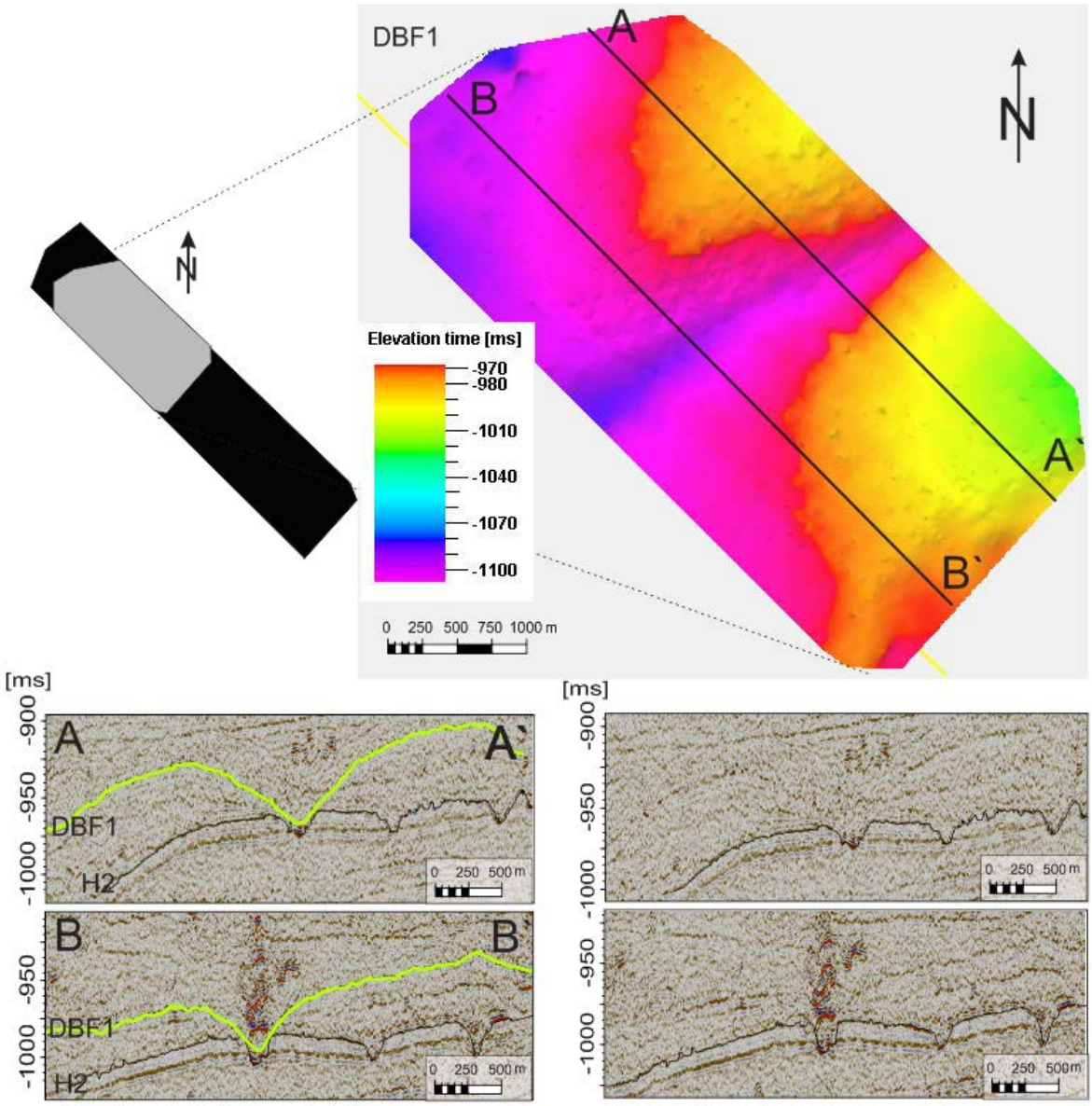

Figure 5.31: Time Depth Map of DBF1 with seismic examples (with (to the left) and without (to the right) interpretation; demonstration how the horizon is narrowing to the South West.

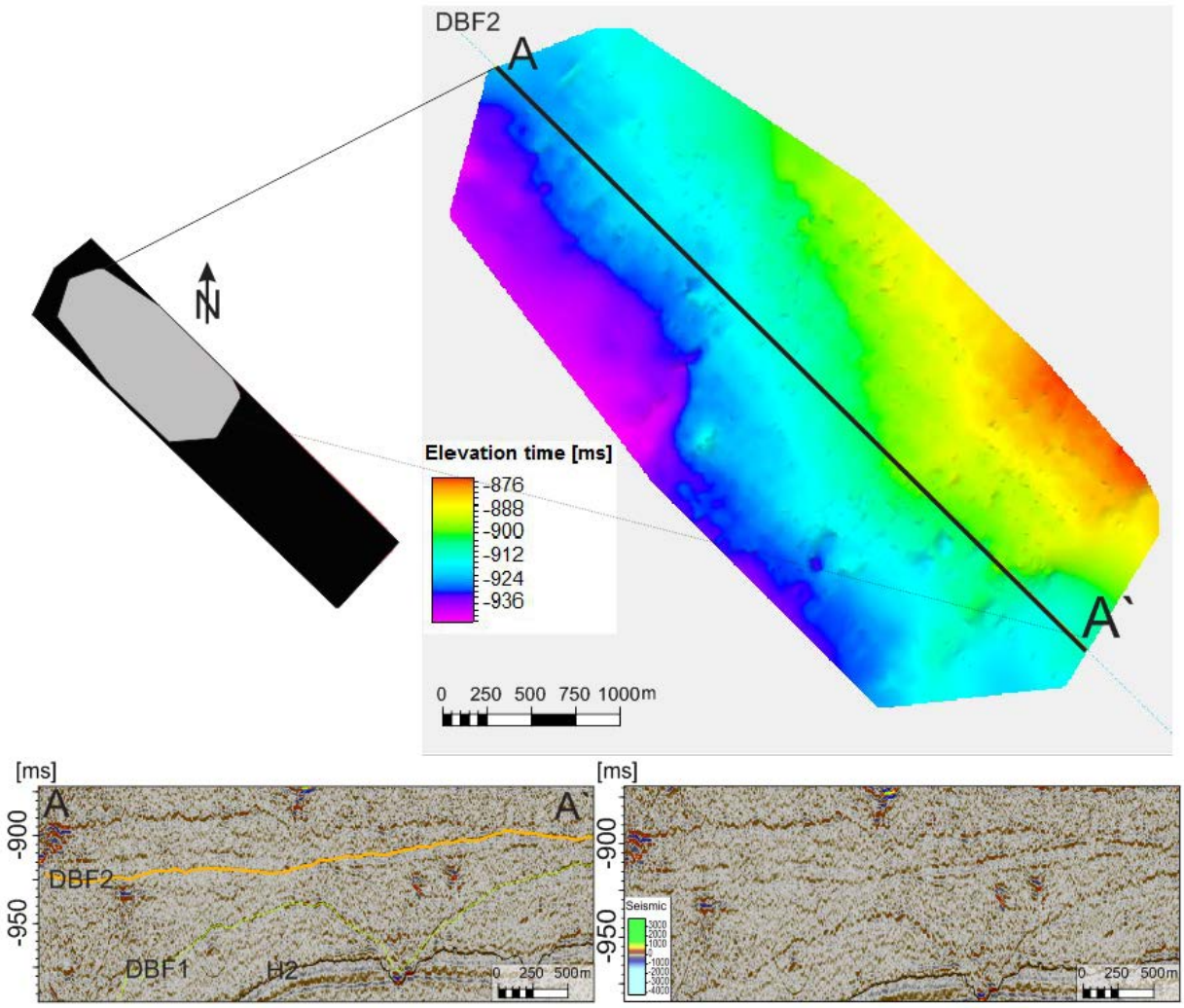

Figure 5.32: Time Depth Map with seismic examples of DBF2; a flatter horizon that seems to be restricted to the interpretation window.

The base of unit U5 is represented by Horizon H2; a medium strong positive reflector, located between 900 and 1040 ms TWT in the seismic, corresponding to ~80 – 225 m below the seabed (fig. 5.33). This horizon is deepening towards NW and is incised with 7 straight, slightly sinuous, NE-SW elongated depressions. In contrast to H1; these depressions are not as deep, 10-20 m, and narrower, 50-150 m. The wideness/depth ratio makes the depressions relatively steep-sided.

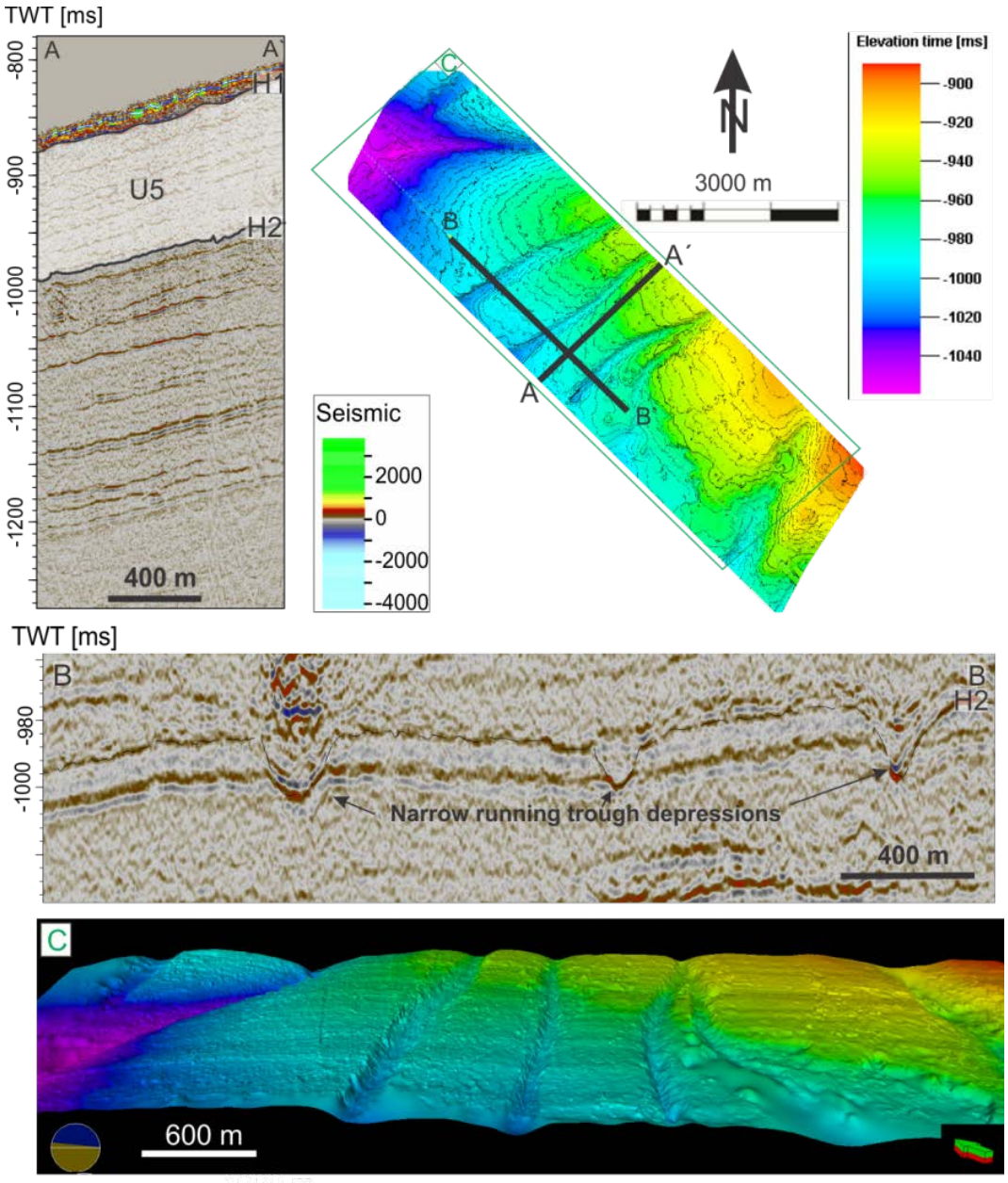

Figure 5.33 A-A`) seismic cross line showing stratigraphic location of unit U5, located between horizon H1 and H2. The H2 surface is shown with an illuminated time-depth map in the upper right corner, while the seismic characteristics of this surface are indicated in the seismic inline profile B-B`, while C shows a 3D window of the surface. Location is indicated in the upper right figure. As seen from the figures, straight and narrow depressions characterize this surface.

High amplitude V-shaped reflectors appear also as thin bands (up to 250 meters) in the depressions crossing NE-SW on horizon H2. A broader band of high amplitude is in addition apparent on this horizon, about 500 – 1200 meters thick, located a little SE of the middle part of the horizon. The high amplitude depression features seem to cut this broader high amplitude band in the SW part of it. The high amplitude anomalies of horizon H2 are highlighted in a maximum amplitude map of horizon H2 (fig 5.34).

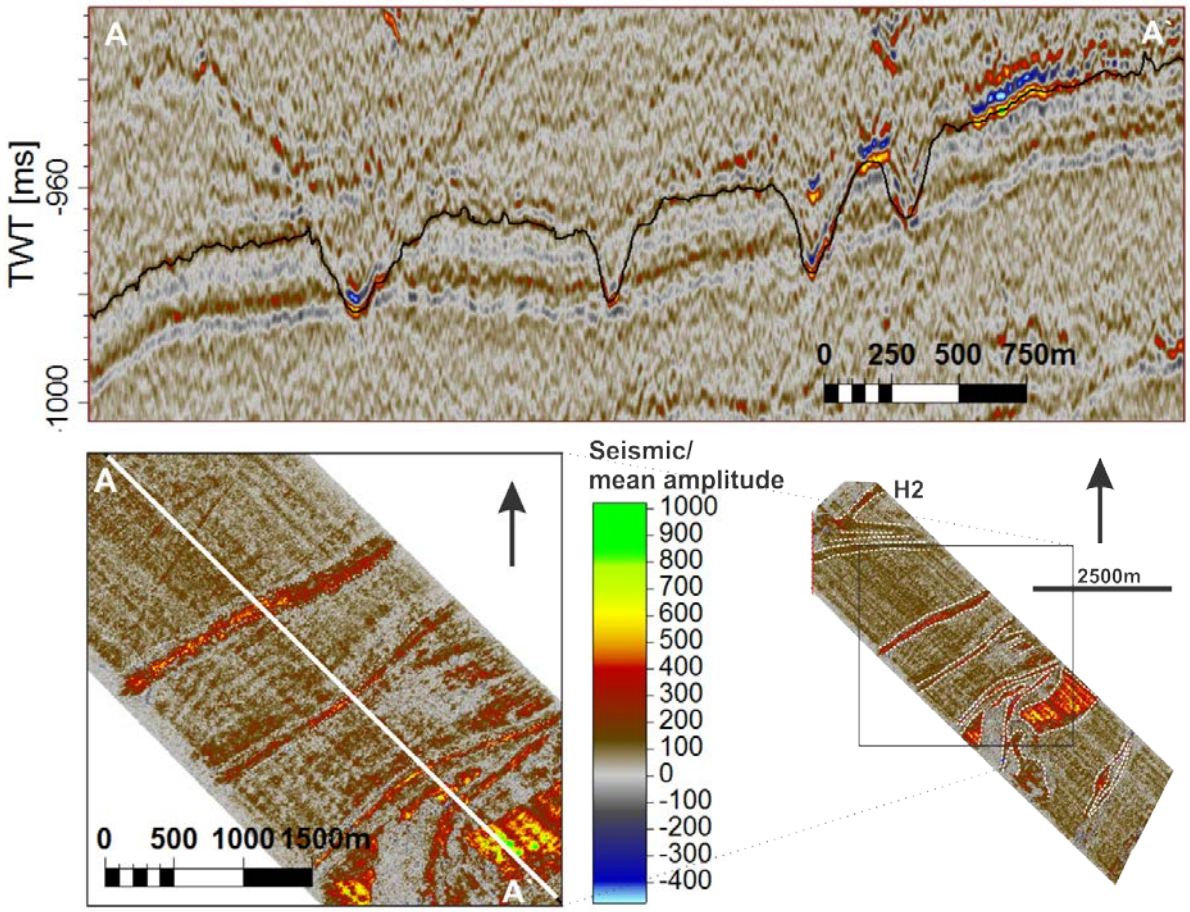

Figure 5.34: A-A`) Seismic inline and amplitude map (lower half of the figure) of horizon H2. As seen, high amplitudes are restricted to the bottom of the depressions in addition to one elevated area in the southern half of the surface.

Interpretation of unit U5

The weak and chaotic, stacked reflectors within this unit fit the characteristics of debris-flow deposits on the upper fan (above 1500 m water depth) (Laberg and Vorren, 1995) (fig 5.29,5.30). However, the NE-SW high amplitude depressions within the unit may be slope-gullies according to the geometry and the classification scheme of Stow and Mayall (2000) and previous interpretation of such features in the area (Vorren et al., 1989). If gullies are apparent within the entire section of H1 – H2 as indicted in figure 5.30, gullying must have happened frequently in between periods with likely larger sedimentation rates and depositional periods of glacial debris flows. At least three generations of erosion (gullying) and deposition (of debris-flows) are indicated to be apparent between H1 and H2. The mounded shape and erosional behavior of DBF1 indicates that this may be one of the other erosional surfaces connected to formation of gullies (fig 5.31).

The high amplitude anomalies restricted to the channel base can indicate presence of channel-fill as fine muddy sediments or well-sorted sand. Finer mud-rich deposits may further be draped on top of the erosive surface of H2 since the overall surface is represented by a positive amplitude reflector (decrease in acoustic impedance). Ice-rafted debris, glacimarine-, and hemipelagic mud deposits are examples of such deposits.

5.2.2.4 Unit U4

Description of unit U4

Unit 4 is located between the smoother high amplitude and continuous reflectors of horizon H2 and H3 and reveals a unit slightly more transparent than the overlying unit (fig.5.19). The unit consists of an 18 – 124 m thick sedimentary succession (fig. 5.35). Unit U4 compromises of mainly chaotic and transparent reflectors appearing with stacked and mounded forms (fig 5.35). One higher amplitude, but discontinuous reflector is located in the middle of this unit, called Intra U4 (fig 5.35: stippled line). Seeded 3D auto-tracking revealed the consistence of this horizon (green area, bottom figure of fig. 5.35); that appear flat, but in patches across the seismic area.

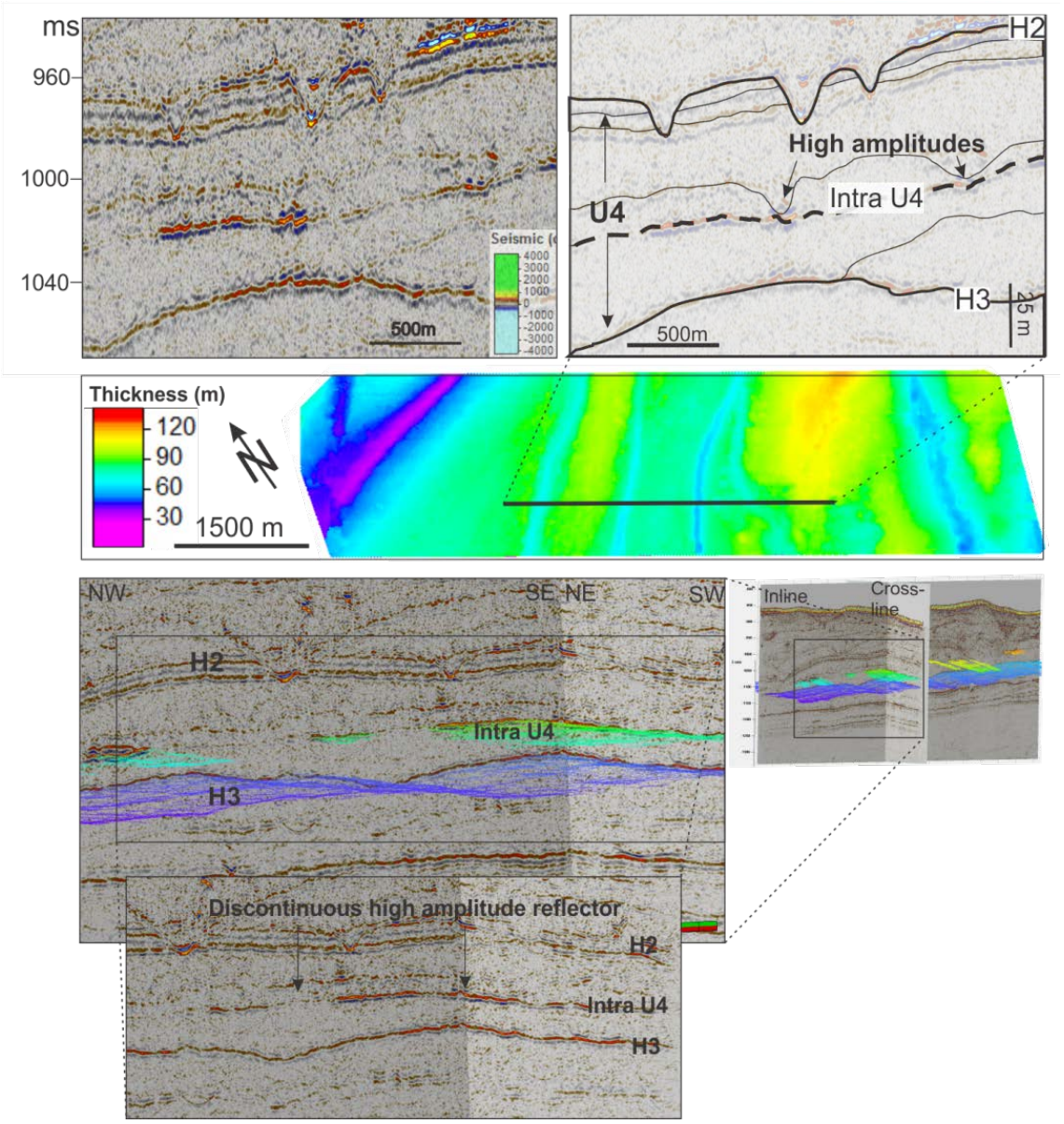

Figure 5.35: Part of a seismic inline (location in the upper right corner) without (left figure) and with interpretation (right figure) of layering within unit U4; boarded by horizon H2 and horizon H3.

The base of this unit is represented by horizon H3, which appears between 960 and 1100 ms TWT in the seismic at the base of U3, equivalent to 140 – 280 m below the seabed (fig. 5.36). The reflector of horizon H3 appears as a strong, pervasive and positive reflector, deepening towards NE. The horizon is incised with slightly defined elongated depressions with approximately the same width and depth as the channelized seabed, 1000-1500 meters wide, and in average 40 meters deep. The depressions become slightly wider towards SW (down the slope).

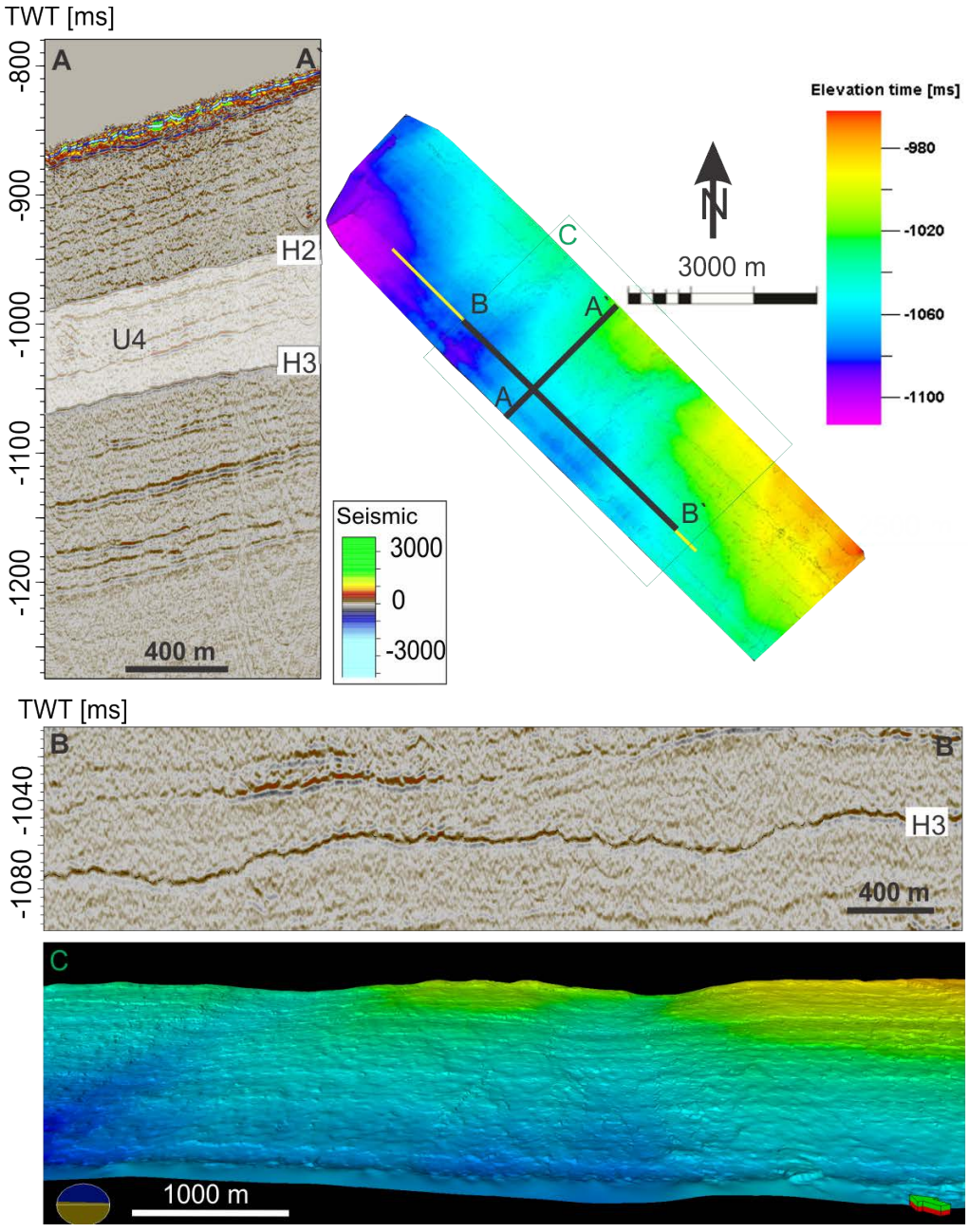

Figure 5.36: (A-A`) Seismic cross line of stratigraphic location of unit U4 that is bounded by horizon H2 and H3. The other figures present the seismic signature (B-B`) and 3D window of illuminated time depth map (C) of Horizon H3. Location of A-A`, B-B`, C and overview of the entire surface within the 3D seismic cube is given in the upper right corner. As seen, the horizon is presented by a high amplitude reflector with two weak, linear and relatively broad topographic depressions.

Slightly higher amplitude values are restricted in bands on the elevated areas between the elongated depressions (fig. 5.37).

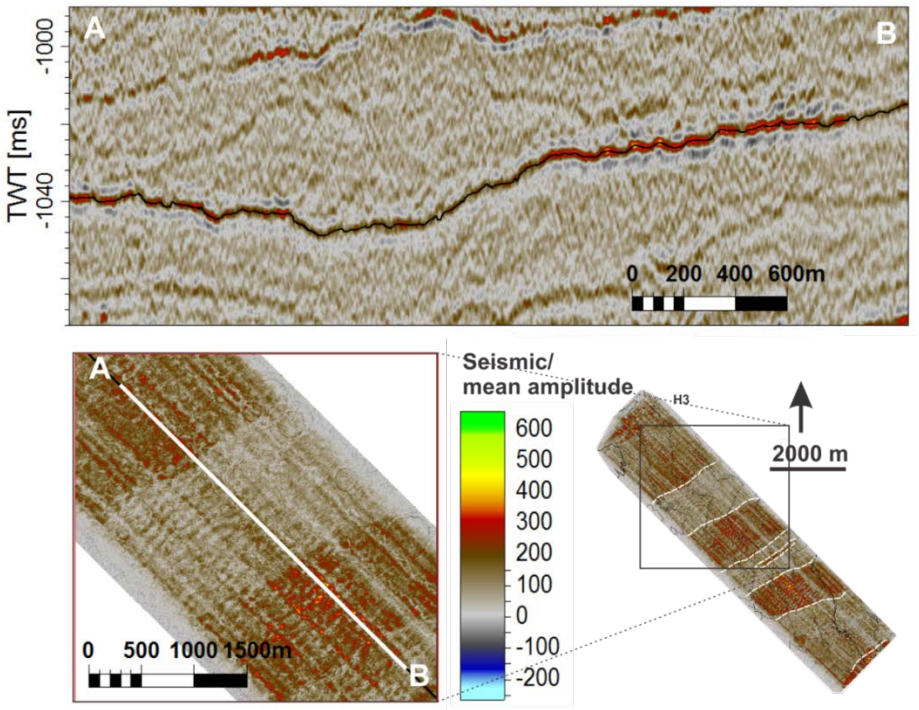

Figure 5.37: Close up of a seismic inline (A-B) and a mean amplitude map (2 ms time window) of H3 (entire amplitude map in the lower right area of the figure, enlarged area in the lower left area of the figure) illustrating that higher amplitudes are restricted to the elevated areas.

Interpretation of unit U4

Due to the transparent appearance with weakly mounded and chaotic reflectors in between, this unit is interpreted to mostly consist of debris-flows. The higher amplitude horizon in the middle of the unit however, may represent a more consistent erosive surface, indicating more starved conditions. As seen from the cross-line in fig. 5.35, IntraU4 is actually a higher and more consistent reflector than H2, and I suggest that this horizon may represent the reflector between D2 and F in Sættem et al., 1992 or the reflector between VI and VII of Laberg and Vorren (1996) (fig 5.20; table 2). The base horizon H3 may be characterized by weakly developed channels. According to the classification of Stow and Mayell (2000), such channels are referred to as fan-delta (ephemeral) channels. The surface may overall be draped with fine sediments since the horizon represents a decrease in acoustic impedance, and softer or finer material have lower acoustic velocities than for example coarser debris-flows. The high amplitudes on elevated areas may for example reflect better preservation of fine material here since down-slope activity is happening more actively within channels.

5.2.2.5 Unit U3

Description of unit U3

Unit U3 reveals the sedimentary unit located between Horizon H3 and the deeper horizon H4. The unit is 36 – 84 meters thick, and has an average thickness of 62 meters (fig. 5.38). The unit appears mostly as transparent with some indications of layering. Gully-like (small, V-shaped) structures with some higher reflection amplitude are observed within unit U3. Two examples of those are illustrated in A and B in fig. 5.38. Towards the top of unit U3, internal layering becomes more similar to the shape of Horizon H3, meaning more mounded shaped (fig 5.38).

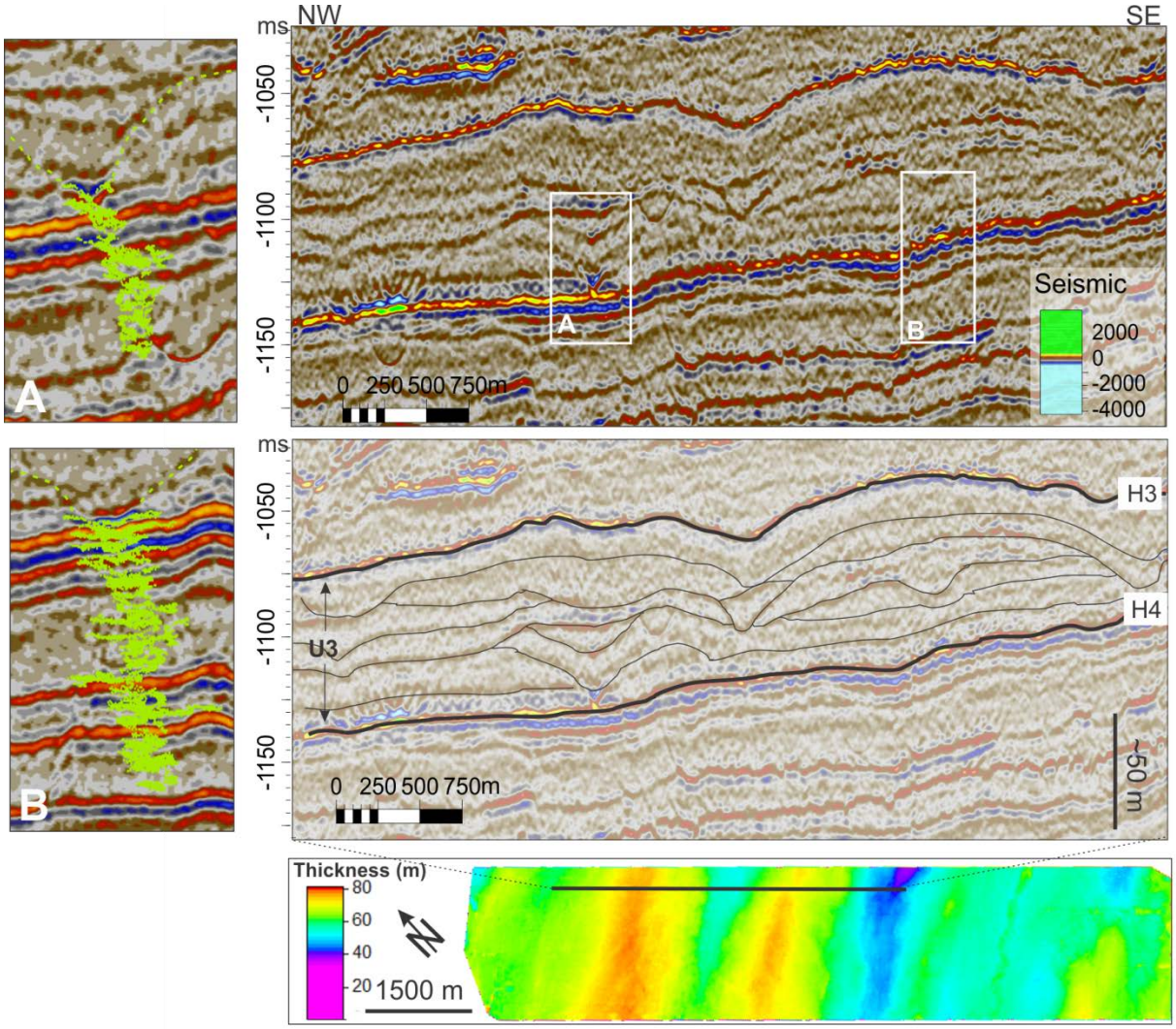

Figure 5.38: Presents an en-larged seismic inline with example of unit U3 (without interpretation in the upper part of the figure, and with in the lower part of the figure) that is located between horizon H3 and H4 (loaction of inline given in the small square to the right). The interpretation of layering within the unit reveals weaker more chaotic internal reflectors with some higher reflectons in between. A and B in the figure reveal two of the V-shaped high amplitude features that characterize the amplitude map of horizon H4 (fig. 5.40) The seismic cube used for this example is treated with TRACE AGC and smoothing by x,y,z = 1 to better highlight the structures inside the unit.

The base of unit U3, horizon H4, is a clear, smooth medium strong positive reflector that continuous through the dataset. The horizon appears between 1020 and 1170 ms TWT, or 200 – 325 m below the seabed. This is a more even surface than overlying surfaces, deepening towards NW. In the SW area, however, the surface show a slightly wavy appearance and horizons underneath it seem to truncate towards the surface here (figure 5.39). One meandering feature of lower elevation is also located in the southeastern part of the horizon.

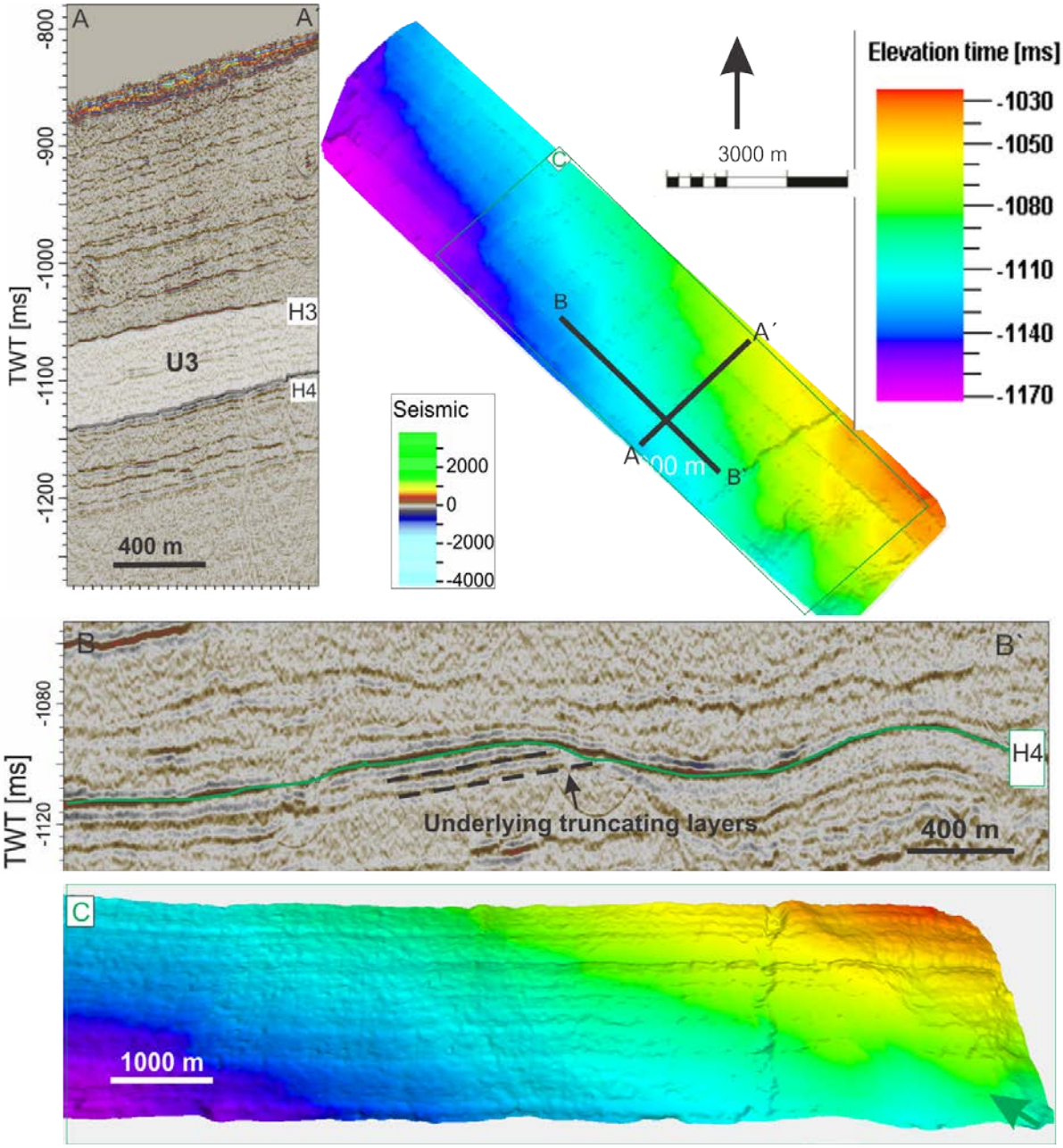

Figure 5.39: A-A`) seismic cross line with stratigraphic location of unit U3. The depth map of the base horizon, horizon H4, is shown in the upper right corner. A seismic example of the horizon is given in B-B`, while a 3D window of a close-up of the surface is illustrated in C.

An amplitude map of Horizon H4 reveals the presence of 3 high-amplitude, linear features that occur parallel to each, about 2-3 km apart from each other's (fig. 5.40). These high amplitude features are oriented NE-SW, and are ~5 - 20 m wide. The features do not appear with change in topography on horizon H4, but they seem to have the same dimensions as the gullies interpreted in horizon H2. Even though they don't reveal topographic changes on horizon H4, it is possible to observe that a weak, overlying and channelized horizon is present and penetrates down into H4 where the high amplitudes occur (fig. 5.40). The meandering feature has also slightly higher amplitude than the general horizon and appears in blue on the amplitude map (fig. 5.40).

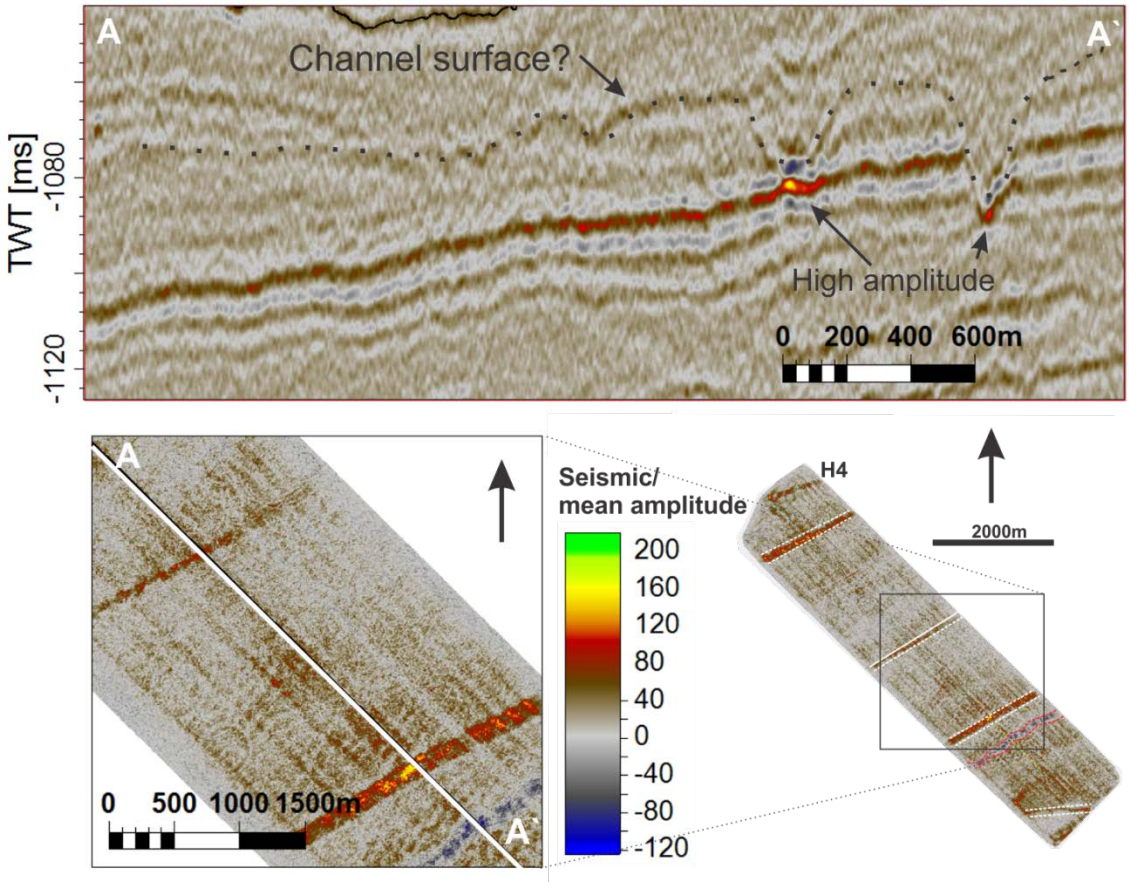

Figure 5.40: A-A`) close-up of a seismic inline (location in lower left corner) and amplitude map (2ms, lower part of figure) of horizon H4. The illustration shows typical variation in amplitude along the horizon. The figure indicates that the thin bands of higher amplitude along the horizon may be due to a seismic erosion horizon further up in the seismic that penetrates down into H4 in areas where the high amplitudes are present.

Interpretation of unit U3

The chaotic to mounded weak reflectors within unit U3 are also interpreted to be debris-flows. However, high amplitude V-shaped depressions within the unit may also reveal indications of erosive gullies within the unit that may have occurred in between deposition of debris-flow. The high amplitudes of horizon H4 also indicate that these may come from an overlying channelized surface rather than horizon H4 itself which does not have any change in topography where the high-amplitudes are located (fig.5.38; 5.40).

5.2.2.6 Unit U2

Description of unit U2

Unit U2, located between horizon H4 and H6, consists of a relatively thin succession deepening towards NW (fig.5.19). The unit occurs in the time window of 1030 and 1240 ms TWT, or the same as ~200 – 378 m below seabed, and has a quite uniform thickness, varying from 41 – 78 meters, but on average 65 meters (fig.5.41). The thinnest section is located in a small area in the SE corner, were the unit might show a more erosional behavior. This unit differs from the other units by consisting of 6 (including horizon H4 and H6) continuous and sub-parallel medium – low amplitude reflections appearing ~10 – ~40 meters apart. The reflectors become clearer towards the top. The three bottom horizons are quite clear and continuous as well. Part of the upper unit is truncated in the south by horizon H4 and a possible fault plane (fig. 5.41).

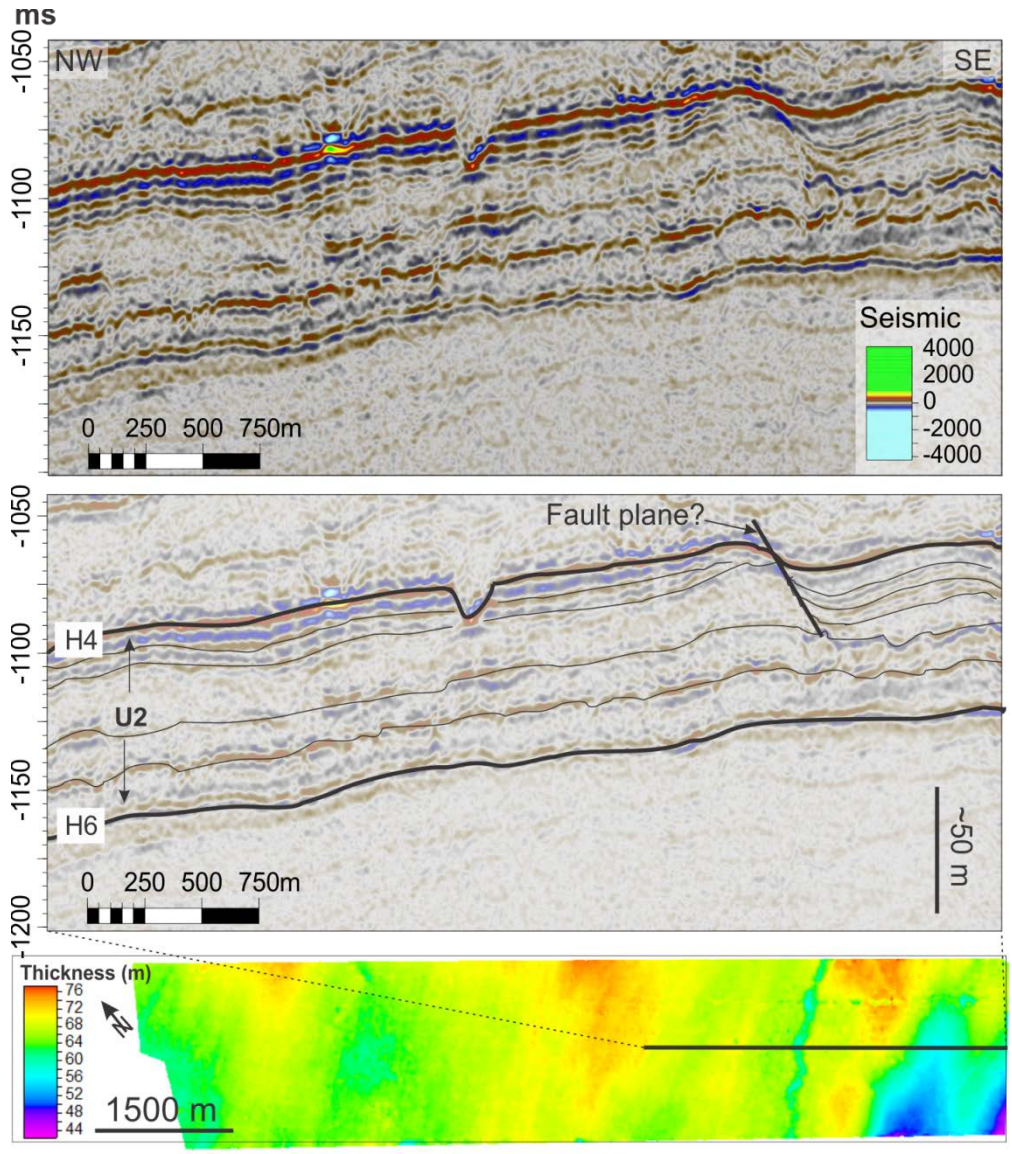

Figure 5.41: Part of a seismic inline without (upper figure) and with (lower figure) interpretation of layering within unit U2. Parallel layers seem to be interrupted by a fault plane in the southeastern area.

However, there are some structural differences among the reflectors within this unit. While horizon H5 appears as a horizon with a complex network of narrow elongated depressions, 20 – 30 m wide and 1-4 m deep, directed down-slope (NW-SW) in a sinuous shape, horizon H6 appears as a more flat smooth and structure-less surface (fig 5.42).

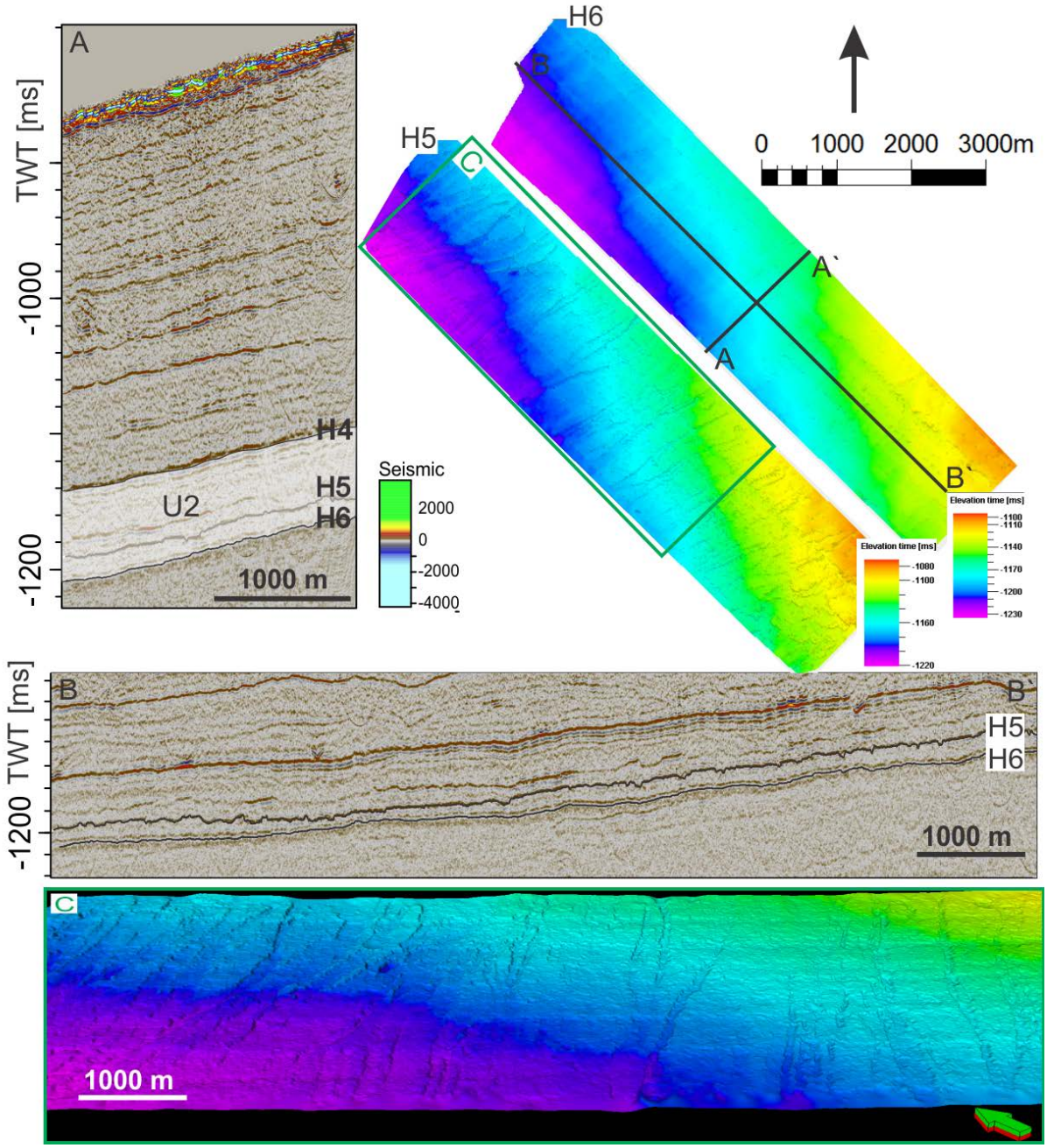

Figure 5.42: A-A`) seismic cross line with stratigraphic location of unit U2. Depth map of horizon H5 and base of horizon H6 is shown in the upper right corner. Seismic inline B-B` is an example of horizons H5 and H6, while a 3D window of a close-up of the surface of horizon H5 is illustrated in C. As seen from the seismic example of H5 and the 3D window, H5 is characterized by a network of narrow and shallow depressions oriented down the slope.

The sinuous shaped network of narrow depressions described above occurs also on a mean amplitude map (fig. 5.43), indicating that there are a change in amplitude restricted to these features. The features become clear enough to interpret (fig. 5.43). As seen in figure 5.43, the features appear very dense, and are mostly oriented NE-SW.

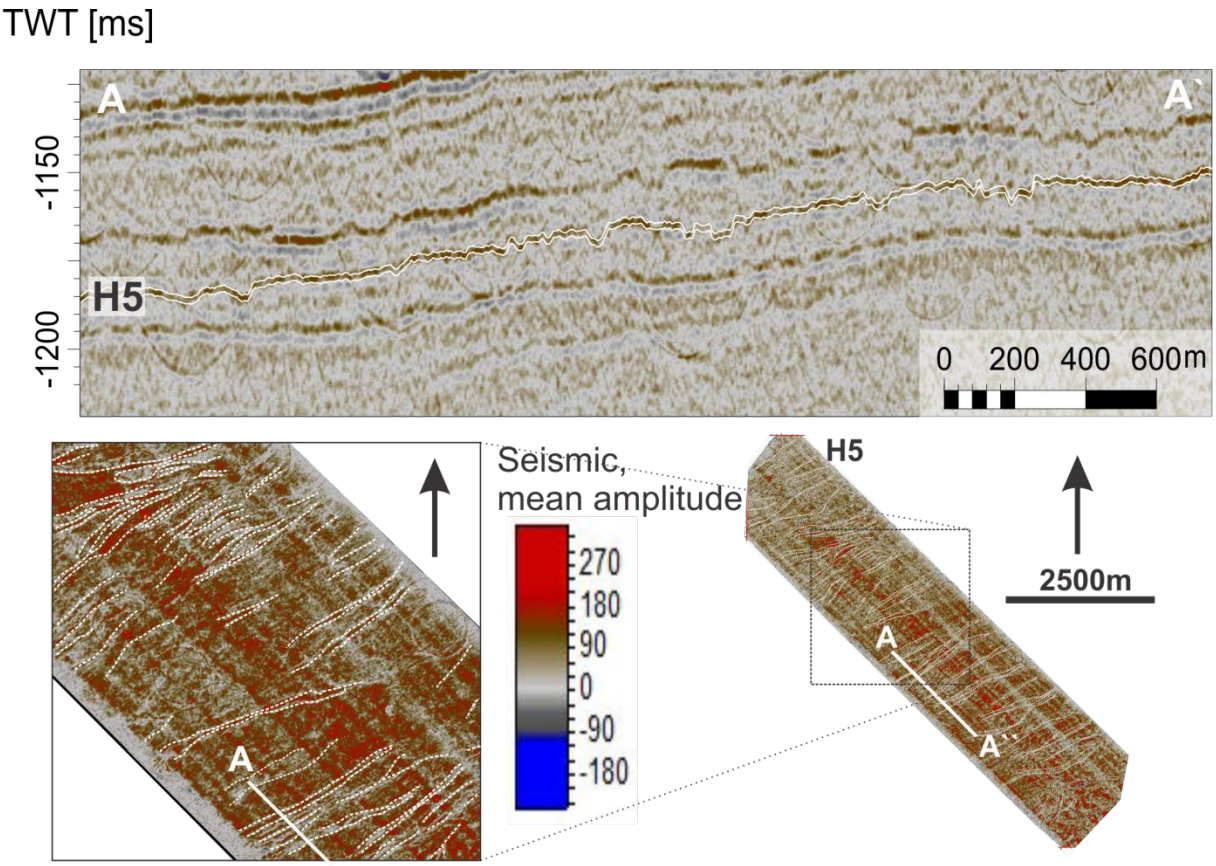

Figure 5.43: A-A`) Close up of another inline of horizon H5 and adjunct mean amplitude map (2ms, lower half of figure), highlighting that the changes in amplitude along the horizon are connected to the narrow depression structures.

Interpretation of unit U2

Due to the relatively dense, consistent and parallel appearance of the reflectors within unit U2, I speculate that this unit may be glaci-marine sediments rather than debris-flows. The nature of horizon H5 is also interesting; the network of narrow elongated depressions might originate from slumping, glaci-tectonic or sediment streams in finer, better sorted material than debris-flows.

5.2.2.7 Unit U1

Description of unit U1

Unit U1 is the lowermost stratigraphic unit that has been interpreted during this work, located between horizon H6 and R1 (fig. 5.19). The unit varies in thickness from ~180 – 300 meter in the study area and has an average thickness of 246 meters. Unit 1 appears as the most transparent zone of the dataset. Discontinuous and weak reflectors that partly show a stacked behavior are sporadic observed within the unit (fig. 5.44).

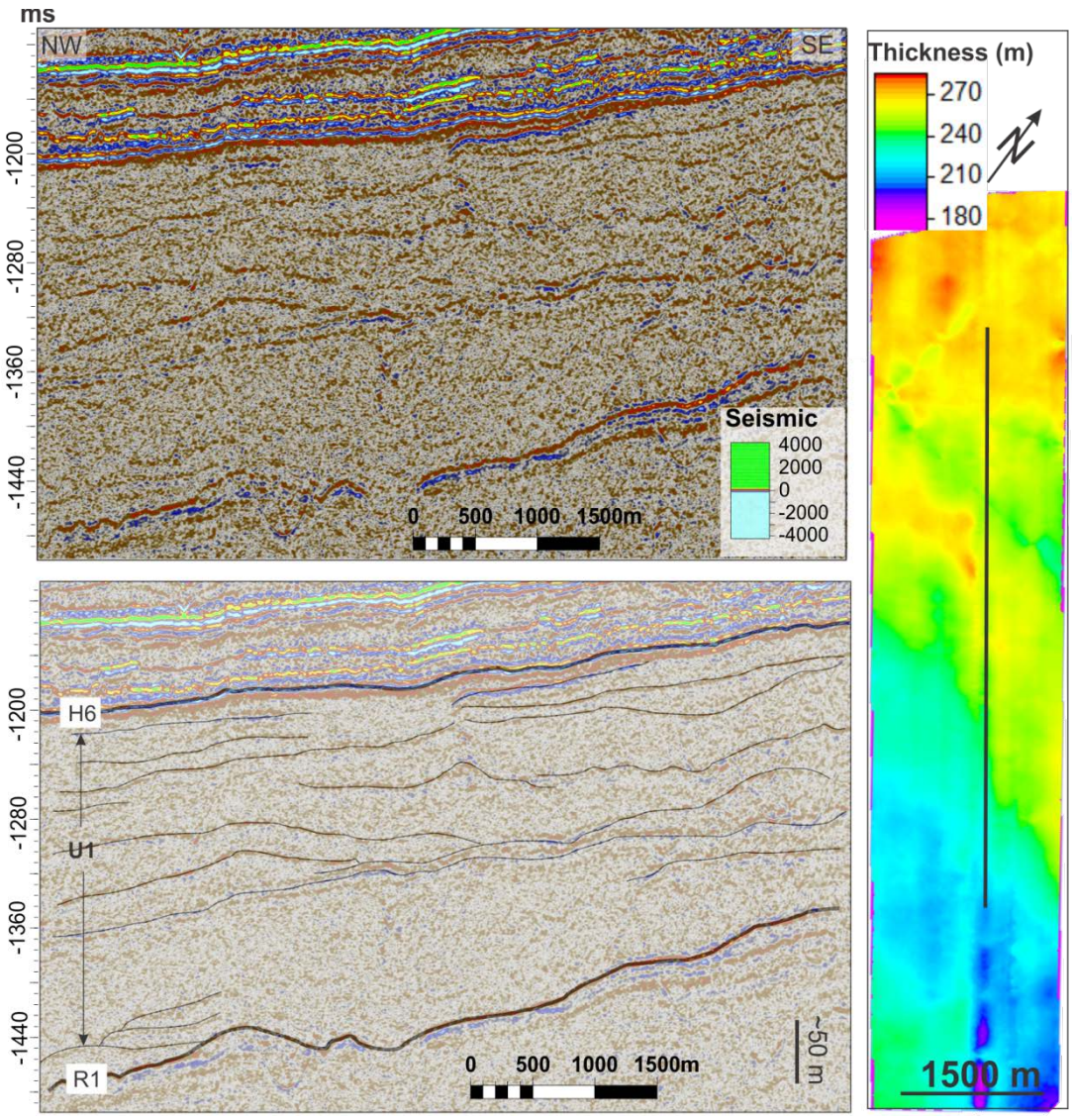

Figure 5.44: Part of a seismic inline without (upper figure) and with (lower figure) interpretation of layering within unit U1. The unit is in general transparent with some weaker reflections in between.

Interpretation of unit U1

This unit also shows quite different behavior than the typical units of U5-U3, though no high amplitudes are apparent within the unit. It appears as a pure, thick succession of debris-flows. Due to the depth of this unit, the reflection strength is very low and possible structures may not appear due to this. However, according to the 2D lines close to the cube, the unit between horizon H6 and R1 reflector appear also as quite transparent, indicating that the seismic unit is similar to the way it appear in the 3D seismic (fig. 5.22)

Chapter 6 - Integration and Comparison of bathymetric and P-Cable 3D seismic data

Migration velocities of sand waves based on displacements of crest-lines between the 2008 and 2011 surveys do certainly have uncertainties, which are related to positioning errors of the two surveys of the multibeam acquisition systems. Nonetheless, migration velocities between 0-10 $\frac{\text{meters}}{3\text{ years}}$ have been calculated for the three year period between the surveys, taking into account that positioning errors may represent up to 10 of these meters. A comparison between the seabed outside the sand-wave field shows lateral displacements from 0 to ~10m, as indicated in figure 6.1. However, such displacement seems to be anomalously high (fig. 6.1) and for most places the two bathymetry maps seem to coincide very well. Since a general displacement to the NW of the sand wave crests from the 2008 to the 2011 dataset are consistent with the direction of NAC and the asymmetry of the sand waves indicate that some migration in order of 0-3.3 m/year have happened during this three year time between the surveys.

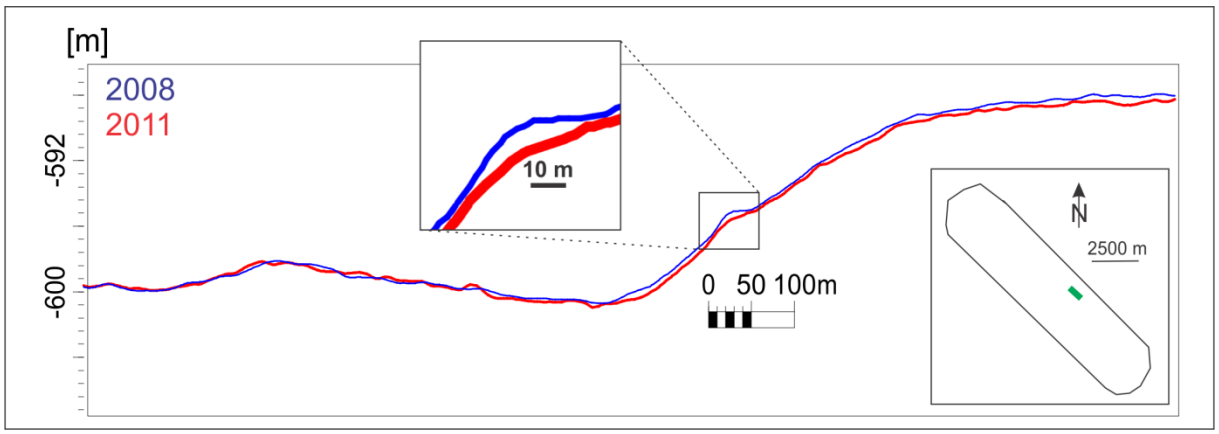

Figure 6.1: Shows a comparison of the general seabed of the two bathymetry data sets. The generally seem to merge, but in some places a lateral displacement of up to ~10 meters was found.

Comparison of the seismic seabed reflector and the interpretation of it with the bathymetry surface were performed by counting sand waves across cross-sections on the same locations. The correlation shows a good match between both data sets; the same number of sand waves appeared in ¾ cases in the bathymetry and corresponding seismic data. Even small sand waves with wave-height smaller than 2 meters (according to the bathymetry data) were visible in the seismic (fig. 6.2). This should be a testament to the high resolution of the seismic data.

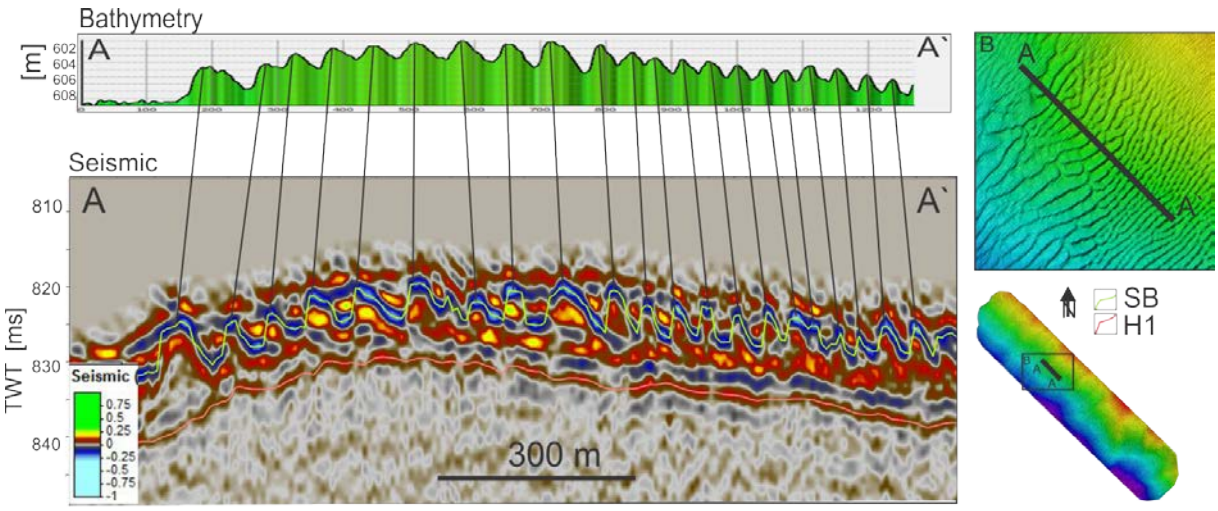

Figure 6.2: Comparing bathymetry and seismic confirms good resolution of the seismic.

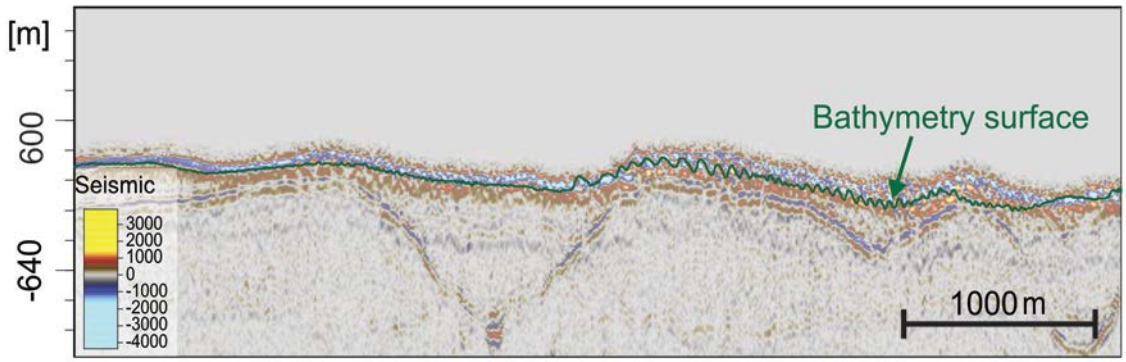

Figure 6.3: Seismic cross-section in the inline direction with bathymetry surface on top, showing a lateral shift of the two data-sets.

Even though most of the sand waves that are visible in the bathymetry are visible in the seismic as well, the geometry of the sand waves appears slightly disturbed in the seismic due to the stacked behaviour of the seabed reflections and the diffraction events caused by the undulating seabed. Analysis of the same seismic and bathymetry profiles supports this statement. An example of sand wave-geometry difference between datasets is the dip angle of the lee-and stoss sides. The dip of the lee- and stoss-side of sand waves on the seismic seabed is distinctively higher than on the bathymetry data, even though the sand waves seem to be of similar height (fig 6.4, right fig.). The seismic data show a maximum lee-side dip of 28*compared to the 16* maximum dip of the lee-sides within the bathymetry data (fig. 6.4, left fig.).

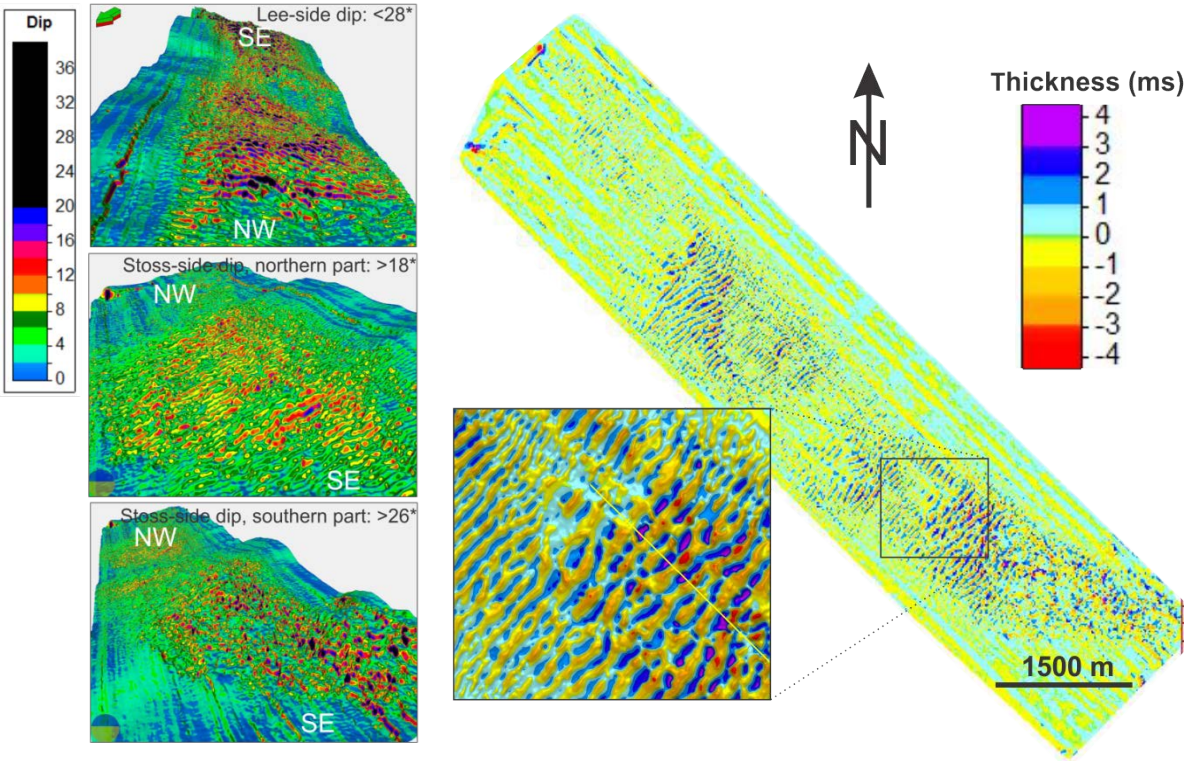

Figure 6.4: Dip-map of the seismic seabed presented in 3D windows seen from SE and NW, showing the seismic expression of difference in lee- and stoss-side dip of the sand waves.

Chapter 7 - Discussion

7.1 Governing controls on sand wave formation on the continental slope of the Barents Sea, area N2

7.1.1 Ocean Current regimes in the study cause formation and migration of sand waves

Ongoing ocean modeling studies indicate that the water-mass transition zone (indicated in figure 5.1) migrates up and down in a meandering pattern by several tens of meters during a single day, caused by internal waves (Skardhamar, Institute of Marine Research, pers.com.). Even though there are examples of sand wave formation on shelf margins suggested to be caused by internal waves e.g. (Karl, 1986, Harvey, 1966), the high-latitude study area is also macro-tidal (tidal range exceeds 4 meters), and observations (fig. 5.1) indicate that Atlantic Surface Water Currents enter the seabed where the sand waves are located. From the available current-data in the area it seems also to be correct to assume that the pathways for the North Atlantic Current (NAC) and the Norwegian Coastal Current (NCC) influence the location of the sand waves on the seabed (fig. 5.1). These observations together give rise to a large variety of possible mechanisms behind the formation of sand waves, and the IMR (Institute of Marine Research) is currently analyzing current meter data to model the current regime of the area in a dense grid (160x160 m) to answer of these questions related to the dominant current mechanism behind the formation of sand waves.

The maximum current speed above the seabed was 0.4 m/s to the North and South during two months of recording of current meter-data 20 meters above the seabed (Skagseth, Institute of Marine Research, pers.com.). However, bottom current modeling results show a maximum current speed of 1.2 m/s during the year (Skardhamar, pers.com.), which is 300% times higher as the observed speed. Formation and migration of sand waves requires a bottom-current velocity of at least 0.4-0.9 m/s (Stow et al., 2006). The observed and modelled current velocities fall therefore well within the range for sand wave formation and migration. It indicates a presently active migration of sand waves in the study area.

To compare, modeling results done by IMR indicate a maximum current speed of 0.7-0.8 m/s in the water mass above the sand-wave fields in the Hola Trough, outside Vesterålen (Bøe et al., 2009a). Depending on tidal stage and season, the currents in this area are observed to vary in strength and direction across the area; were maximum velocities flowing both NW and SE seems to vary from 0.5 – 0.8 m/s. These two sand-wave fields are comparable for various reasons, They are both located along the Norwegian continental shelf, and local topography and interaction of several current systems is suggested to create the complex depositional pattern in the Hola Trough, outside Vesterålen; the

sand waves vary from being symmetric to asymmetric, and sand waves with different migration directions are indicated across the study area.

Modeling of sand-wave migration is important while linking migration rates of sand waves to current velocities. Since that has not been done during this work (not possible due to lack of data), what has been possible to do is to link potential calculated migration rates, sand wave dimensions and current regime in the study area to others findings of sand-wave migration (Besio et al., 2004, Knaapen, 2005, Morelissen et al., 2003, Aliotta and Perillo, 1987). However, since sediment waves occur in a variety of dimensions (1s – 10s of meter in wave-height, 10s-100s of meters in waveleght), grain-sizes (mud waves – gravel waves) and may form due to a variety of current systems (e.g surface currents, tides, internal waves, turbidites, thermohaline currents and slumping), - all being factors that surely will affect the migration rates, I have met some challenges when trying to do this.

Migration rates of sand waves with average wavelengths and wave-heights of 500 and 5 meters, respectively, are likely to be in an order of magnitude of tens of m/year following table 3 (Morelissen et al., 2003). According to the dimensions of the sand waves in my study area (average wave-length and wave-height of ~ 70-80 m and 1-2 m, respectively), one should assume an even higher migration rate while considering the bed-form size as a separate factor of migration rate. Similar migration rates of sand waves as studied in my area are suggested for tidal sandbanks (with wavelengths and heights in average 5000 and 10 meters, respectively).

Table 3. Characteristics of offshore sand bed forms(Morelissen et al., 2003)

Bed form	Related flow	*L*[*m*]	*A*[*m*]	*T*	*c*
Ripples	instant flow	~1	~0.01	h	~1 m/day
Mega-ripples	storm surges?	~10	~0.1	days	~100 m/year
Sand waves	tide	~500	~5	years	~10 m/year
Long bed waves	unknown	~1500	~5	unknown	unknown
Tidal sandbanks	tide	~5000	~10	century	~1 m/year

L denotes the wavelength, *A* is the amplitude, *T* is the times scale and *c* is the order of magnitude of the migration rate.

In the Southern Bight of the North Sea and the English Channel, sand waves with an average wave-height and -length of 1.5 meters and 200 meters, respectively, show migration rates of 0 – 10 meters/year (Knaapen, 2005). In the North Sea migration rates have been observed from 1988-1989 to be 1.5 and 1.8 m/year on sand waves varying in wave-height from 2-10 m, and wave-length from

120 – 500 meters. Modeling results however, showed a migration rate along the same transects of 18 m/year (Besio et al., 2004).

Controversy, anomalously high migration rates, on average 33 m/year are observed for sand waves with wave-heights up to 6 meters and wave-lengths between 80 and 200 meters in the entrance of Bahia Blanca (Aliotta and Perillo, 1987). The calculation was done from repeated bathymetric surveys. The near bottom average current strength recorded here was as high as 1.2 and 1.05m/s (Aliotta and Perillo, 1987).

Even though the maximum current speed in the area is high, the migration rate of an average sized sand wave in my study area (1-2 m/year) seems to be relatively low. The maximum current velocities detected for the two month time period of recording indicated 0.4 m/s – barely enough for transporting sand grains across stoss-sides of the sand waves and deposit them on the lee-sides. Based on this observation I suggest that migration of sand waves in the study area does not happens continuously throughout the year, but episodically and might depend on season and tidal stage, - factors that can control the depth of the transition zone of the water-mass boundaries and intensification of the NAC and NCC.

7.1.2 Factors controlling the geometric properties of the sand waves

Crest-shape

Factors controling the shape of the crest of sand waves:

- Belderson et al. (1982) associate sand ribbons with peak current speeds of 0.75 – 1 m/s. In the Gulf of Cadiz, west of the Strait of Gibraltar, deep water (700-775 m.b.s.l) sediment waves occur in a variety of directions and crest shapes in an area, where the lower Mediterranean outflow (MOW) mixes with the North Atlantic Currents (Habgood et al., 2003). The change in topography across the area indicates a decrease in current speed of MOW of more than 1 m/s (O`Niel Baringer and Price, 1999) where ribbons and scores are present, to less than 0.5 m/s above more straight crested sand waves.

- The shape of crest-lines in a sand-wave field is suggested to be related to the abundance of transportable sand (Kenyon and Stride, 1968). Habgood et al. (2003) associate barchan-like sand waves with areas where sand and muddy sand waves are apparent, while longer wave lengths, gentler flanked gradients and more straight crested crest-lines are associated with pure muddy waves. The modeling results of Blondeux (2009) of sand waves in the North Sea support these observations; a finer mean grain size would create longer sediment wave-lengths. This theory however will not be discussed further in this chapter due to lack of grain-size data.
- The tidal current ellipse may also affect the shape crest lines and migration paths of sand waves (Kenyon and Stride, 1968). Kenyon and Stride (1968) indicate a more elliptical tidal ellipse above straight – slightly sinuous crested sand waves, while barchans-shaped sand waves occur where the tidal ellipse are more circular. The study was done of sand waves occurring almost 300 nautical miles apart, from the North Sea to the south western margin of the English Channel.
- Furthermore, variation in sinuosity of crest-lines can also just be related to local variation in advance of the sand waves as indicated by Gomez (2010).
- What is more, the Barchan-shaped sand waves in the southern part of my study area may also be due to limited amount of sand in this area since the residual currents seem to be oriented in a NW direction. Barchanoid waves are observed to occur in other areas where the sediment supply is sparse and where sand waves often sit on a rather coarse (gravel or sand) substrate (e.g. Kenyon et al., 2002; Wynn et al., 2002a).

It is likely that changes in sand wave-migration of smaller and larger-sized sand waves cause sinuosity of the sand waves in the N2 field (fig. 5.3). As indicated in the result chapter (fig 5.5, 5.10), single sand waves tend to increase in size towards the middle of the sand-wave field – and since sand wave size is a function of migration velocity one should assume slower migration in the middle part, and larger migration velocity on the margins of the field, this was also observed (fig 5.16). Local variations of sand wave size due to topography should create similar effect.

Since the Barchan-shaped sand waves do not indicate higher migration velocities from the migration map and profile-analyses, I cannot conclude that these sand waves are located under a higher current velocity regime. However, these sand waves show the largest wave-heights and steepness – indicating that they among the most active bedforms in the study area. Their more symmetric behavior and various indications of current velocity directions according to asymmetry with sand waves migrating towards SE as well indicate a more complex current regime in this area. This may cause sand waves migrating in different directions with more complex crest-shapes, as these barchans-shaped sand waves. If this is true, one may speculate what causes a more complex current regime restricted to this area. The largest channel across the sand-wave field and thereby highest obstacle for current flow is located beneath this area (fig. 5.2), and may cause localized turbulent water flow across this area. It is also indicated that the direction of the NAC is strongly influenced by the broad-scale topography of the continental shelf (Gjevik, 2000).

One may also consider grain-size distributions as a cause of the barchans-shaped sand waves in the south of the field, but due to lack of data this would be pure speculation. The area where the barchans-shaped sand waves are located, defines the SE tip of the sand-wave field. The residual current that is oriented to the NW in the area and the sand that is restricted to the sand-wave fields along the continental slope here (indicated by backscatter data (King et al., not publ.)) may indicate a lack of well sorted sand in this area. However, due to the height and steepness of the sand waves, I doubt that this is the main reason for the difference in shape of the sand waves.

The sand waves in the Hola Trough show straighter crest-lines than the typical sand waves on the slope of SW Barents Sea (Bøe et al., 2009b). I speculate that this difference in shape can be related to a difference in the maximum current speed, 0.7-0.8 m/s in Hola Trough vs. 1.2 m/s in the N2 field of these two sand-wave fields.

Sand wave-size, dip and asymmetry

A common observation for most sand-wave fields is that the sand waves with the largest wavelengths are generally also observed to have the largest wave height, e.g. Gomez et al. (2010) and Habgood et al. (2003).

The results of this study show that within the most uniform part of the sand-wave field, the wavelength/wave height ratio seems to be very similar. The wave height is observed to increase approximately linear with wave length most places (ex. fig. 5.5, 5.7 and 5.12, bathymetry chapter). There is also a good correlation between sand wave size and asymmetry: the larger the sand waves are, the larger is the asymmetry and the lee-slope dip. Figure 7.1 shows the statistical data of Figure 5.11 with trend lines and the linear relation between wave-height and wave-length for shallow water sand waves derived by Flemming (1988). The relationship in my data and that found for shallow-water sand waves appear quite similar suggesting that wave-height and wave-length ratio is not so different in shallow and deep water.

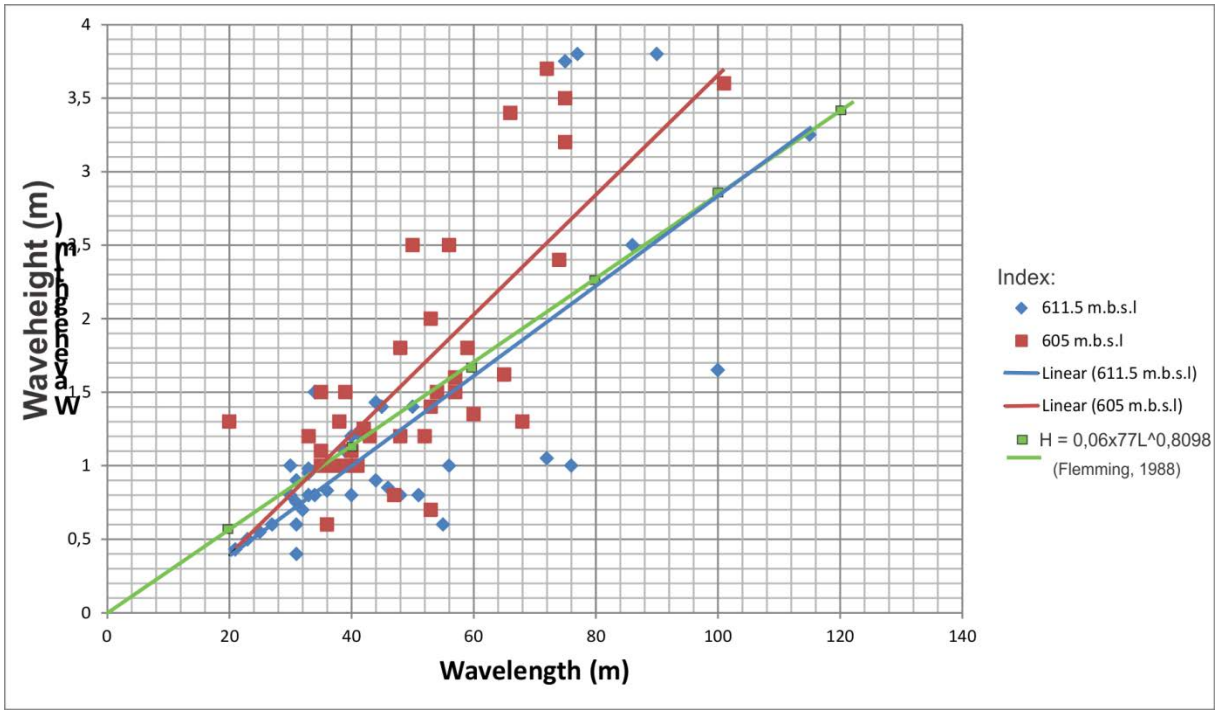

Figure 7.1: the same plot as in figure 5.10 of wave-height versus wave-length of sand waves in a selected area of the sand-wave field; but with trend-lines of the two sets of sand wave-sizes of different water-depth together with the general equation of Flemming (1988).

Knaapen (2005) is one of many researches who made observations that height of sand waves in the North Sea correlates with depth, such that height is uniform at, in his example, 21 meters water-depth. This observation, however, is not found in my study area. The wave height/wavelength plot of figure 7.1 show wave-height and wave-length data for two distinct water depths; 605 m (red) and

611.5 m (blue). The height of the sand waves varies significantly for these two water-depths. The relative variations of water depth within the sand-wave field due to the dipping ground are also small compared to the actual water-depth, ~ 60m/600m. The general sand wave geometry does not seem to be controlled by actual water depth, but rather by the local bathymetry (as also indicated in figure 5.10). The shape and size of the sand waves seem to be restricted to elevation differences; larger sized asymmetric sand waves are located on topographic highs in the area, between the channels on the seabed, while the smallest sand waves are more symmetric and are typically located in the depressions of the channels (ex. fig. 5.7, bathymetry chap.). No particular association of sand wave geometry with water-depth is observed for the similar sized deep-water (200-260 m.b.s.l.) sand-wave fields in the Hola Trough, outside Vesterålen (Bøe et al., 2009a). The sand-wave fields in Hola Trough are separated by glacial ridges, here, the sand content is poor and boulders and gravels dominate the seabed. In contrast, sand waves in my study area form on the elevated ridges as well, and present a continuous sand-wave field across a highly elevated area.

The relation between sand wave geometry and bathymetry is in my study considered to be due to three different reasons:

- Smaller sand waves are typically located in the channels; which are active transport routes for down-slope sediment transport. Mass-wasting events during the last 10 000 years may have interrupted sand wave formation within the channels, and the sand waves in the troughs may be of younger age. Appreciable amounts of sediments have been deposited in the channels since the start of the Holocene Deglaciation – up to 50 meter in the troughs.
- The amount of sand available in the area could limit the growth of sand waves. A thicker succession of sand has the potential to create larger sand waves, a suggestion that would indicate that a larger amount of sand must be apparent on the topographic highs compared to the troughs. This is unlikely however, as the seismic results of the interpreted sand-layer indicate the opposite. On the elevated highs the reflector beneath the seabed horizon is located practically along the base of the sand waves; high backscatter values in the troughs also indicate that the gravelly base is close in those areas.
- The current regime above elevated areas is stronger than above channels. Increased current velocities on elevated areas are consistent with existing knowledge about flow behaviour. Currents will accelerate because of limiting flow area towards higher elevated areas, while they will decelerate again when flowing across deeper areas. Increased current strength will enhance formation of sand waves, leading to more rapid formation of large sand waves. The asymmetry and dip of sand waves could also indicate current strength and direction. Larger asymmetry and lee-slope dip, as observed on the elevated areas in the study area, should in

theory indicate larger bed-form activity and thereby relatively larger current velocities within parts of the study area.

Even though migration rate results indicate significantly higher migration rates of smaller sand waves within the lower elevated areas and towards the margin of the sand-wave field, the current strength may actually be lower above the troughs. Gomez (2010) provide evidence that the migration rate of sand dunes studied in Bahía Blanca estuary decreases as the bed-form height increases and flume experiments by Castello (1981) indicate the same results; smaller sand waves migrate faster than larger sand waves. Larger bedforms requires more sand to move during migration (more energy); and the migration of larger sand waves will therefore take longer time compared to smaller waves.

7.1.3 Internal structure or buried sand waves in the N2 field?

Many examples of high-resolution seismic data reveal evidence for both internal structures within sediment waves and buried sediment waves, especially found in deep water (Faugères et al., 1999, Masson, 2001, Normark et al., 2002, Masson et al., 2002, Migeon et al., 2000, von Lom-Keil et al., 2002). Feugeres et al. (1999) indicated buried sediment waves overlain by debris-flows in Plio-Pleistocene sediments from single channel airgun seismic and sparker seismic lines. These sediment waves appear very clear in the seismic, and even layering within the single sand waves is apparent. However, the studied sand waves of that work and most of the others work mentioned above, reveal sediment waves of 10-100 m in amplitude and wavelengths of 0.5-10 km; something that makes them approximately an order of magnitude larger than the sand waves in my study area . Nurmak et al. (2002) identified buried sediment waves of similar-sized sand waves as this work's study area, denoting wave-heights and wave-lengths from 1 and 100 meters, respectively. They used deep tow boomer and high-resolution air-gun seismic to identify the buried sand waves.

Identifying internal structure and buried sand wave horizons in the sub-surface of the study area should therefore be possible in the high-resolution 3D seismic used in this study. However, I high-pass filtered the data and evaluated attribute maps like variance in the shallow seismic section, but could not identify internal structures of the sand waves. Also, sand wave appear to be absent on any of the deeper horizons that I have mapped. The up to 5 ms (3-4 m) thick seabed reflector, however, can potentially disguise internal structures of the sand waves. Also, it may not create a reflector even though they are apparent because these potential layers likely have similar lithology. An interesting observation is that all sediment waves with internal structures mentioned in the examples above (Faugères et al., 1999, Masson, 2001, Normark et al., 2002, Masson et al., 2002, Migeon et al., 2000, von Lom-Keil et al., 2002) are suggested to be caused by turbidity currents; currents that ideally create more layered lithology and thus would more likely create internal reflectors.

Gravity cores and grab samples across the area also reveal a sand-layer of a maximum thickness of 7 meters (close to the maximum wave-height of the sand waves) in the area , and TOPAS data across the field also confirms the maximum thickness of 7 meter (NGU, in prep.). I have also looked at available Chirp seismic data and compared it with the seismic data during this thesis. The Chirp data shows similar observations as the seismic data imaging the seabed and the channelized base beneath it. Some weaker reflections occur inside the channel fill between SB and H1 (ex. fig. 7.2). It is difficult to identify details of the sand waves from the Chirp data as this data is strongly affected by diffraction hyperbolas caused by the undulating seabed. These hyperbolas cannot be removed on Chirp data by migration, because Chirp data is generally stored as the amplitude envelope of the seismic response.

In addition, coarse sediments as gravel are observed in the troughs of the sand waves on video photography (King et al., not publ.). This indicates that the base of the sand layer at these places is on the same level as the sand wave troughs. Together these observations suggest that only one generation of large sand waves might be evident in the study area.

However, this hypothesis does not imply that sand-wave migration has happened in the study area only for a short period of time. By assuming an average migration of 1.6 m/year (the middle value of the migration rate), it will take over 6000 years for all sand waves to move from the start to the end of the sand-wave field.

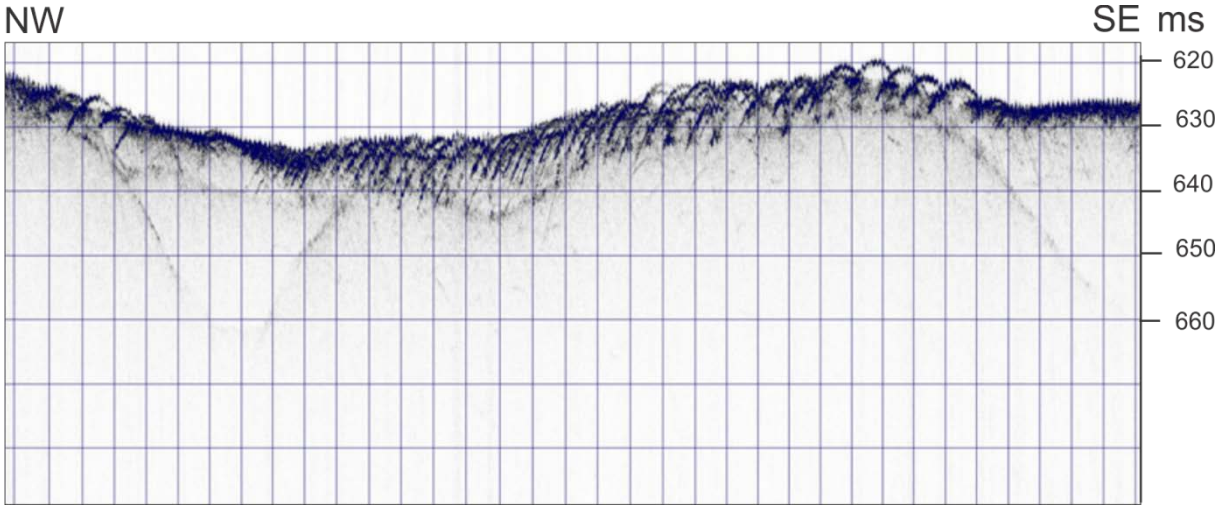

Figure 7.2: Example of a Chirp line in a NW-SE direction across the sand wave area, where the seabed, a weak horizon inside the left channel as well as the base horizon H1 are apparent. The straight line just beneath the top of the hyperbolic events that represent the sand waves may represent the base of the sand waves.

7.1.3 Volume estimate of sand in the sand-wave field

Three different approaches have been employed to locate and interpret the boundary between the sand layer and underlying glacial deposits in the study area. The thickness map of these three horizons and the seabed together with a polygon that defined the sand-wave field was used for the volume calculation in Petrel. The resulting volumes should give a rough estimate of the minimum and maximum volume of sand in the sand-wave field. By using the average thickness of the sand thickness maps, I have also calculated how much sand migrates across this average area yearly.

From the seismic data:

- **Alt. 1:** The first method is based on the assumption that the first reflector that appears under the seabed represents this boundary. This means that I followed H1 on the elevated highs and the first weak reflector that appears in the channel fill of U6 where the channels are located (fig. 7.3: pink line in A and nr.1 thickness map). This reflector appears some places very deep, down to 28 meters below the seafloor, and the average thickness of the interpreted unit is 9.74 m, and would thus not be as representative.
- **Alt. 2:** This method was done by assuming that the base of the high amplitudes occurring under the seabed reflector represents the transition from chaotic higher amplitude reflectors of sand, to more transparent chaotic reflectors of glacial material (fig 7.3: green line in A and nr. 2 thickness map). The max thickness in this case turned out to be 13 meters, and the average thickness 6 meters.

From bathymetry data:

- **Alt. 3:** Volume of a thickness map of a smoothed seabed, shifted down to the approx. base of the sand waves and the actual seabed. This should give a minimum sand volume estimate. The maximum thickness for this alternative is ~6 meters (fig 7.4).

The interpretations of alt. 1, 2 and 3, are presented in figure 7.3: alt. 1: pink area; alt. 2, green area; fig. 7.4: alt. 3 and fig. 7.5: alt. 1, pink line; alt. 2, green line. On the topographic highs between the channels the sand waves are assumed to migrate on the top of horizon H1. Results show that the upper elevated boundary of the sand-wave field fits well in certain locations where the thickness of the mobile layer is close to or equal to zero (fig. 5.22a), suggesting that the lack of sand causes the sand waves to abruptly end at those locations.

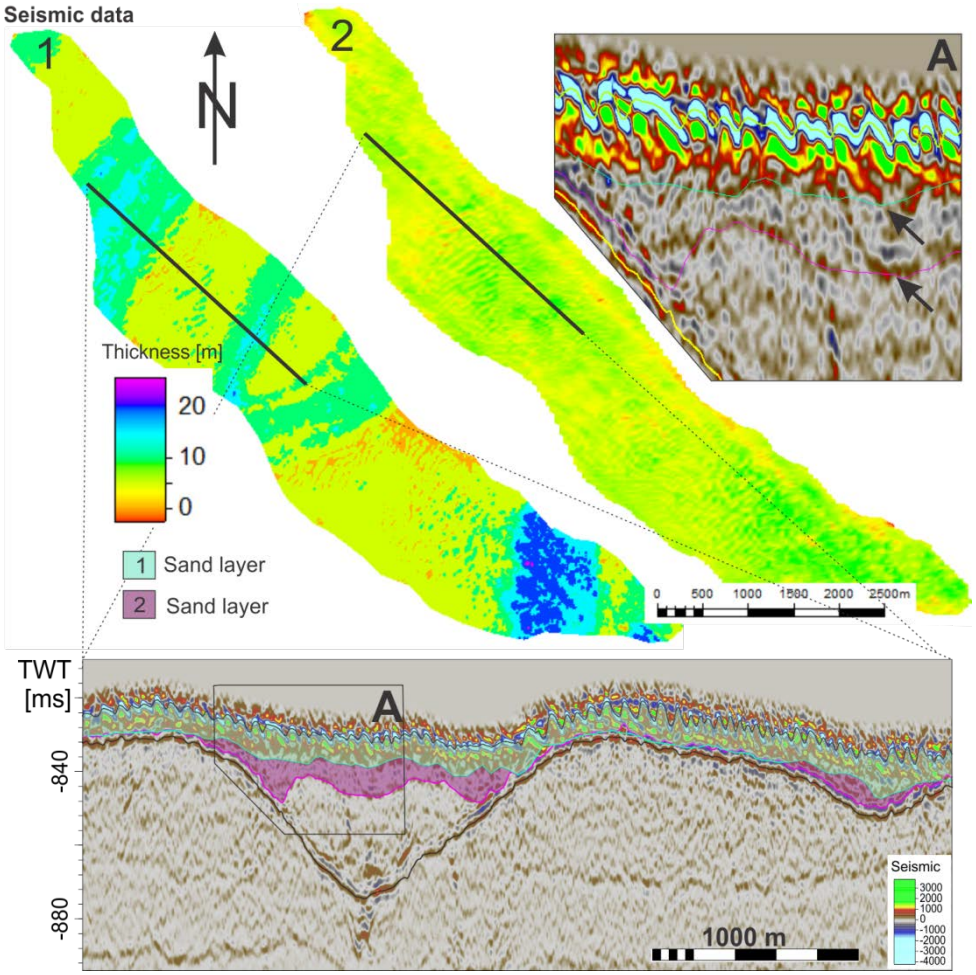

Figure 7.3: The interpreted thicknesses of the mobile layer of sand moving across the sand-wave field from the seismic data.

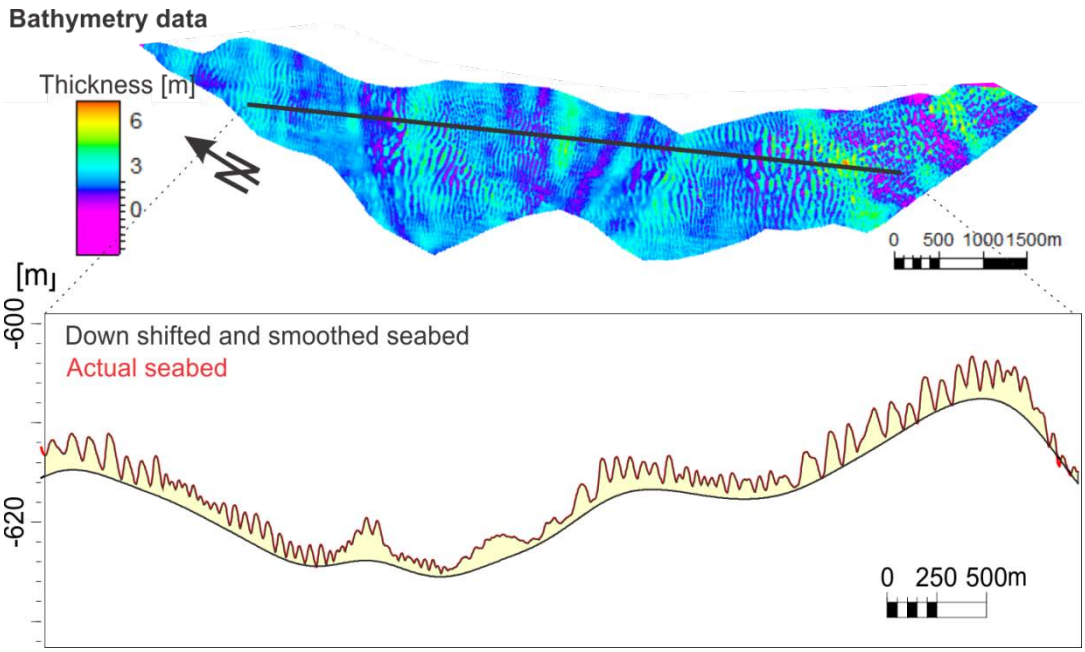

Figure 7.4: The indicated thickness of sand in the bathymetric data where a down shifted smoothed seabed has been used as a base of the sand layer.

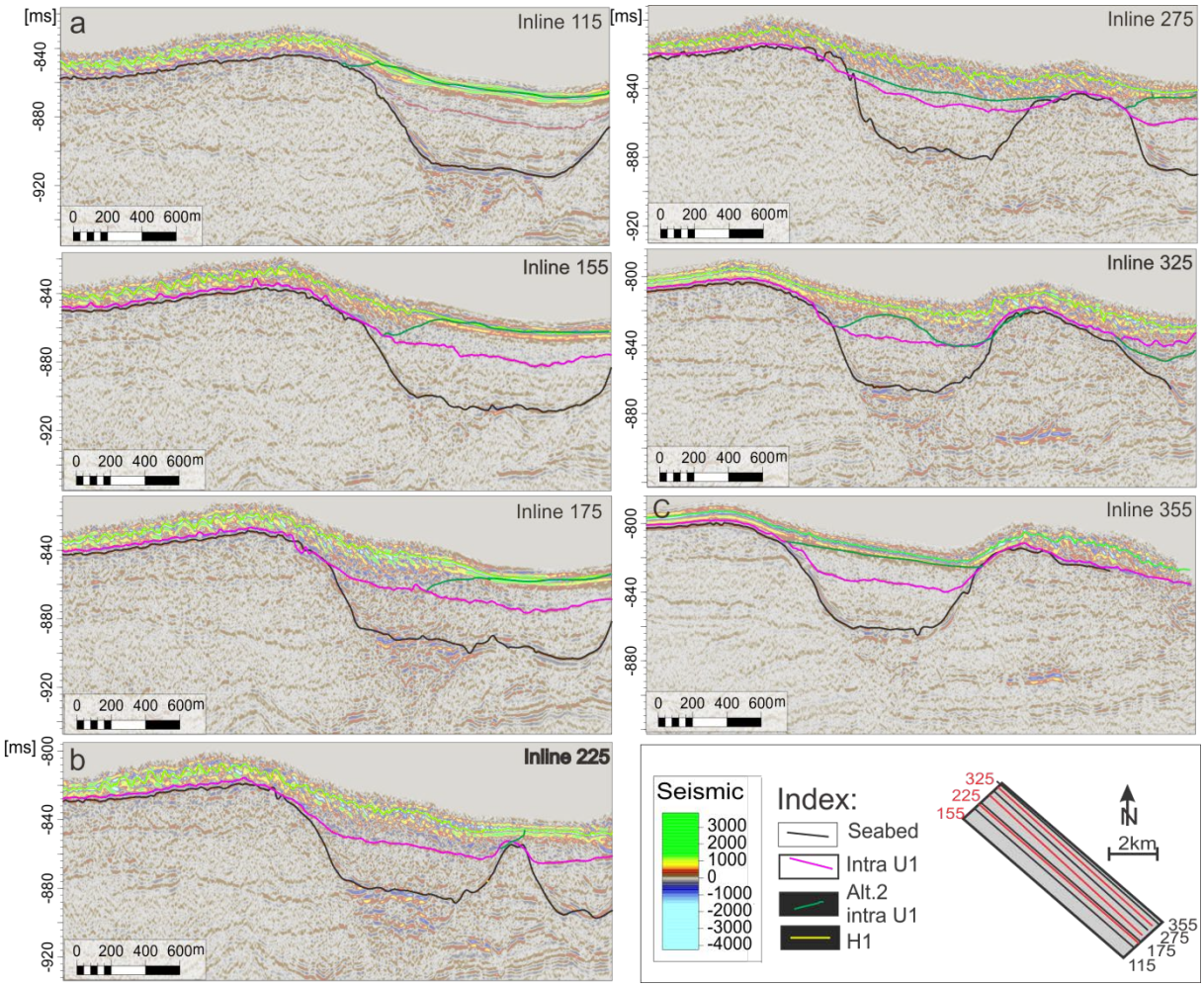

Figure 7.5: Seismic cross-sections between the seabed and horizon H1, showing the seismic expression beneath the sand waves. The figure highlights the high amplitude reflectors underneath the location of sand waves, suggesting an alternative base of the “mobile sand layer” (Alt 2. Intra U1).

Results of volume calculation

- **Alt.1 (fig 7.3 nr.1):** A maximum volume of sand of $V_1 = 118 \times 10^6 m^3$
- **Alt. 2 (fig 7.3 nr.2):** Or an alternative maximum volume of sand of $V_2 = 73 \times 10^6 m^3$
- **Alt.3 (fig 7.4):** Minimum volume of sand of $V_3 = 22.3 \times 10^6 m^3$

The average thicknesses of (1), (2) and (3), are 9.74 m, 6 m and 2.2 m, respectively. These values together with the average wideness of the sand-wave field; 576 m (calculated in Petrel form a polygon around the sand-wave field) and the assumed average migration rate 1.6 m/year;

The amount of sand that is migrating through a cross-section of the sand-wave field yearly has been estimated to be

- Alt. 1: $9.74m \times 576m \times \frac{1.6m}{yr} * 1yr = 8663\ m^3$
- Alt. 2: $6m \times 576m \times \frac{1.6m}{yr} * 1yr = 5529\ m^3$
- Alt. 3: $2.2m \times 576m \times \frac{1.6m}{yr} * 1yr = 2027\ m^3$

7.1.4 Origin of sand

The sand – gravel sand material on the seabed of the Norwegian continental slope has been assumed to originate from the Weichselian glaciation (Bøe et al., 2009b). The last glacial maximum (LGM) had its maximum cover (all the way to the shelf edge) of the Barents Sea ~20 ka ago. The ice-caps location on the shelf edge allowed a large amount of coarse material to be able to deposit on the continental slope at that time. A chosen number of studies indicate (Rokoengen and Dekko, 1993, Fjalstad and Møller, 1994, Møller, 2000), that the sea level immediately after the last glaciation in the Hola area may have been 50 m to more than 100 m below the present sea level. This fact, together with observed winnowing of shelf sediments down to at least 500 meters during post-glacial times (Kenyon, 1986, Vorren et al., 1988) can indicate that sand material was redistributed and sorted by oceanic currents and winnowing from the onset of the last deglaciation, which also caused sand waves to develop when the sand content on the seabed was abundant enough. Sand waves may have started to develop during the Holocene transgression that started around 8000 ca.l yr. bp. Slubowska-Woldengen (2008), however, documented evidence of Atlantic Water flowing along the continental shelf edge during the entire deglaciation and it is possible that the sand waves started to develop earlier. The exact timing of the initiation of the sand waves is difficult to determine, but they likely began to form as soon as there was a coexistence of sand and active currents on the Norwegian continental slope.

7.2 Glacial evolution during Middle – Late Pleistocene

7.2.1 Deposits and bedforms in the study area

The studied sedimentary unit of GIII is compromised of sediments deposited during glacial-interglacial cycles of Late Pleistocene time e.g. Vorren et al. (1991, Faleide et al. (1996), Laberg and Vorren (1996) and Ryseth et al. (2003).

Not until the beginning of that time, ice-sheets started to cover the entire Barents Sea and expanded to its maximum size (Knies et al., 2009, Larsen et al., 2006). Due to these proximal conditions of the ice-sheet on the slope, unit GIII also marks the beginning of the Trough Mouth Fans and extensively debris-flow activity (Vorren and Laberg, 1997). Damuth (1979) was probable one of the first that indicated that most of the glacigenic sediments deposited during this time on the slope consists of gravity controlled debris-flows and turbidites. Over-steepened slope and excess pore-fluid pressure due to high sedimentation rates likely created instability on the slope and deposition of such mass-flow deposits during the maximum glaciations (Vorren et al., 1989, Vorren et al., 2011). The dimensions of the debris-flows vary; 2-40 km wide, 5 – 60 km thick and up to 200 km long are dimensions reported by the study of Vorren and Laberg (1997). However, the relative amount of debris-flows within the unit is varying along the slope. East of the Bear Island Trough, large ice-streams have led to intense erosion on the shelf, and as a consequence, large amount of debris-flows have been deposited west of it, in the Bear Island Trough Mouth Fan. Bathymetry data also indicate this (Laberg and Vorren, 1995), though an extra build-out of the slope is present in front of the Bear Island Trough (Laberg and Vorren, 1995). The location of these plaeo-ice streams is suggested to have largely controlled the deposition of debris-flows (Laberg and Vorren 1995, 1996, 2000; Laberg and Landvik, 2012; Andreassen et al, 2004). During interglacial periods, or starved conditions due to position of ice-streams, erosion by gullying, IRD and hemipelagic deposits have likely dominated the depositional environment on the slope. An example of such starved slope location during the last glacial maximum is Tromsøflaket, where slowly-moving ice is indicated to have flowed across the area at that time, thus created conditions on the slope with lower sediment input (Andreassen et al., 2008).

Mackensen and Hald (1988) suggest that gullies formed by cold dense water in interglacial times. Shelf foraminifera show evidence for this theory in the Arctic Ocean (Mackensen and Hald, 1988). Vorren (1989) confirms this theory by indicating that gullies on the slope north of the study area were formed during the present interglacial since they are not filled with sediments. Bugge (1983) on the other hand, suggest formation of gullies in glacial periods by the erosional behavior of debris-

flow activity, while Laberg and Vorren (1996) indicate that the gullies within unit IIIV north of the Bear Island Trough are not likely related to debris flows since the gullies are restricted to the northernmost part where debris flows are not observed. Laberg and Vorren (1995, 1996, and 2000) and Andreassen et al., (2007) suggest that gullies may have formed during glaciations, but in slope areas not influenced by high sediment input form ice-streams due to starved conditions.

Seismic expressions

The top of debris flows are often presented in the seismic as mounded weak reflectors on the lower shelf (below 1500 water-depth) and more straight, but chaotic stacked reflectors on the upper slope (above 1500 meters water-depth)(Laberg and Vorren, 1995). The debris flows themselves, are often transparent in acoustic character in parts of the seismic data. As a consequence of their erosive behavior, the base of the deposits is rarely apparent in the seismic. The clear, smooth and high continuous reflectors in the seismic within this unit are often recorded to be erosive reflectors from interglacial times; but could locally also potentially represent reflectors of glacial times in places were grounded slower ice where located on the overlaying shelf in the area rather than fast flowing ice-streams.

The interpreted gullies of horizon H2 and within unit U6, and perhaps horizon H4 may have been originated in shallower water depths than H1, H3 and H5-H6, based on the observation that the channels become wider and deeper towards greater depths. But this phenomenon (wider channels towards deeper depths) is also a typical signature of gullies formed by turbidity currents. Pedrosa et al. 2011) however indicated that gullies of similar age, on NW Barents Sea Continental Slope may have been formed due to cold and dense melt-water plumes during the deglaciations.

Finer material in depressions on the shelf of the South Western Barents Sea is often interpreted to be the cause of winnowing e.g (Vorren et al., 1989, Andreassen et al., 2007, Bjarnadóttir et al., 2012). Winnowing of shelf sediments have been found down to at least 500 meters (considering present sea level) during Late Weichselian time within the Bear Island Trough (Vorren et al., 1988, Sættem et al., 1991), and evidence for shallower sea level than present during that time makes the theory also likely (Bondevik et al., 1999). High amplitude anomalies in depressions during this time and possible other times of similar geological settings is therefore speculated to be fine material that are partly reworked and redistributed by bottom currents on the shelf and upper slope and trapped in the canyons or gullies, where the environment is more protected from currents. Gravity and turbulence could lead to deposition further down the slope through these gullies.

7.2.2 Glacial and interglacial deposits during Late Pleistocene

Reconstruction of the Late Pleistocene Western Barents Sea environment showed three ice-extents, at ~110 ka, at ~60 ka and the last glacial maximum at 19-15 ka (Vorren et al., 2011, Svendsen et al., 2004).

Unit G, F and D2 by Sættem (1992) work, and unit VIII, VII, VI by Laberg and Vorren (1996) work suggests to be corresponding to U5 (fig 5.20, table 2). From borehole data acquired on the slope at 465 meter below sea level, Sættem (1992) shows that these units mostly consist of muddy diamicton interbedded with a layer of stratified glacimarine and marine mud (unit E).

Within the 3D seismic data of this work (fig. 5.29) the base of the horizon seem to represent the start of a slope setting influenced by three episodes. Here, the slope was covered by debris flows in between 4 episodes of active gully formation with possible deposition of finer material (fig. 7.6; 5.29, 7.10). The 3 episodes of interpreted debris-flow activity may represent the glacial maximum periods of 110 ka, 60 ka and 19-15 ka. In between the inferred maximum glaciations, channels may have formed due to melt-water plumes during deglacial periods. This is also suggested for similar aged gullies within the Kveithola Trough Mouth Fan, NW Barents Sea (Pedrosa et al., 2011).

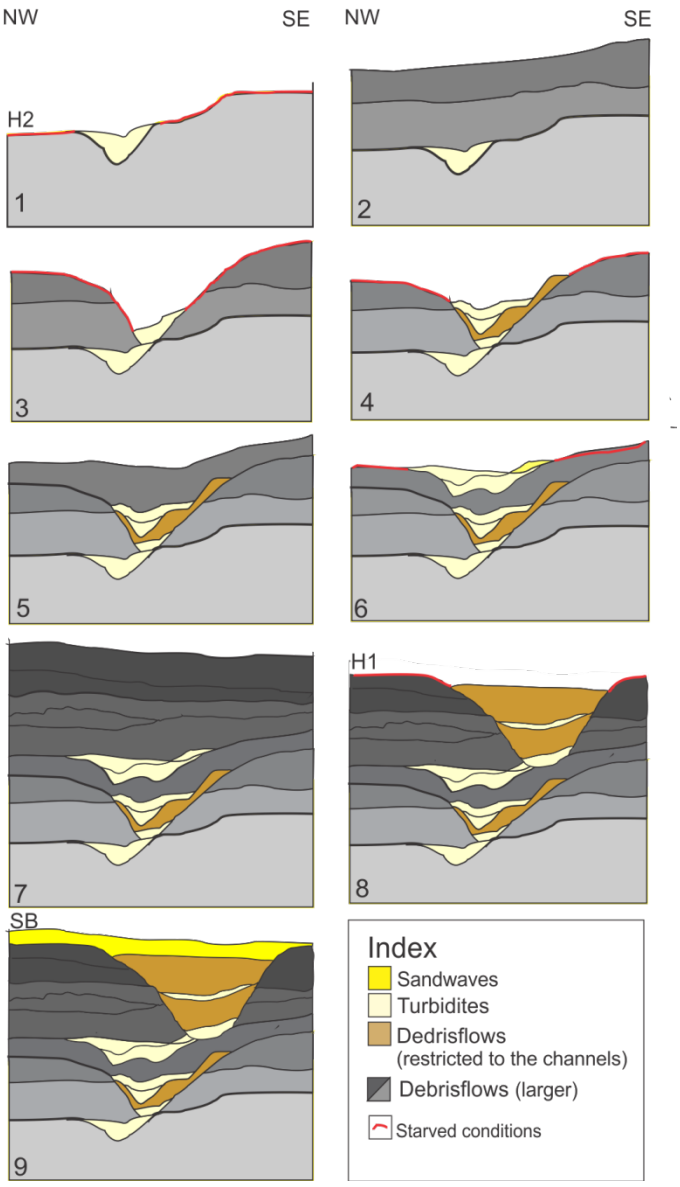

Figure 7.10: Reconstruction of depositional stages from 128 000 years ago to present.

Fast-flowing ice streams occupied the cross-shelf troughs during the Late Weichselian glaciation (28-15 ~4C ka) and caused large-scale erosion. Mega-scale glacial lineations on the sea floor indicate ice-flow directions (Andreassen et al., 2007). Changes in flow pattern rather than glacial advances lead to the different depositional settings on the slope e.g. (Eyles et al., 1983). Final retreat occurred 13,290 yrs BP when the southern Barents Sea was finally deglaciated (Vorren and Kristoffersen, 1986). A thin blanket of glacimarine sediments (<10 m) have been deposited in the glacial troughs since then (Vorren et al., 1988). For the North Western Barents Slope (Sættem et al., 1992, Laberg and Vorren, 1996) and within all the studied 2D seismic lines, unit U6 (SB-H1) is so close to the seabed reflector that it is almost not visible in the seismic However, this unit represents the channel fill that occur on the seabed and a top layer of fine material that drapes it. Within the 3D seismic data, the two horizons that define the unit become very close or meet between channels and at the margins of the sand waves on the seabed. The channel fill is therefore suggested to be deposited after the start of the deglaciation (17 ka) (Winsborrow et al., 2010). The exact start of the redistribution and deposition of sand along the slope (low-stand) and therefore also sand wave formation remains speculative.

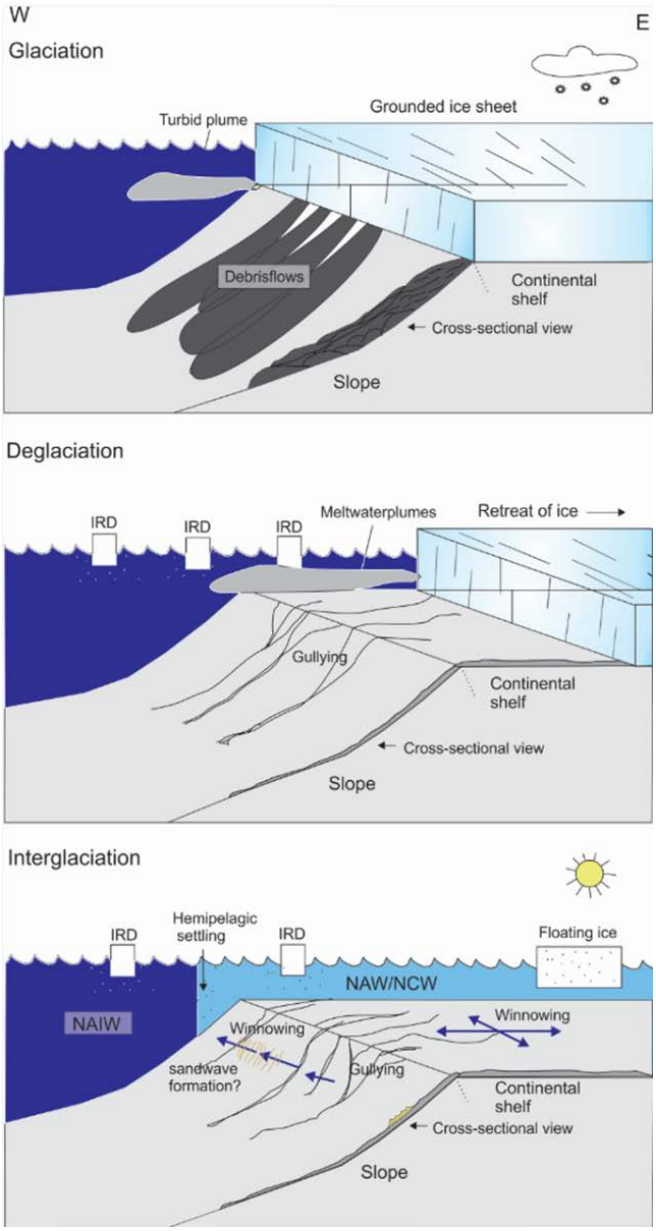

Figure 7.11: The cartoon-style figure sums up the main sedimentary processes on the SW Barents Sea, upper continental slope during the third stage of glacial evolution of the northern hemisphere (Knies et al., 2009) interpreted to be present within the studied 3D seismic. The model is a modification of Vorren (1989) model combined with Lucchi (2002) model.

Chapter 8 – Conclusions

- Multibeam bathymetry and P-Cable high-resolution 3D seismic data have been used to describe the areal distribution, 2D architecture, migration-rate and sediment flux along a sand-wave field on the upper continental slope of SW Barents Sea.
- The sand waves migrate on top of a channelized seabed in water depths of 570 – 660 meters.
- The sand waves are locally larger on topographic highs, where the wave height varies between 3 to 6.6 meters and the wavelength between 100 – 140 meters. In the topographic lows and on the margins of the sand-wave field, the sand waves are typically smaller, showing wave heights smaller than 3 meters and wavelengths smaller than 100 meters. The variation of sand wave size in relation to topography is suggested to be due to higher current strength on the elevated areas compared to the troughs.
- Migration rates of the sand waves have been calculated based on displacement of crest lines over a three year period. Migration rates are up to 3.3 m/year in a NW direction in the northern area of the sand-wave field, and up to 2.5 m/year in the opposite direction, to the SE in the southern flank of the sand-wave field.
- The sediment flux across the area due to migration of sand waves is calculated to be 2000 – 8700 m^3/year.
- The high-resolution 3D seismic data also provided new insights on the depositional environment on the upper continental slope of the SW Barents Sea during the middle to late Pleistocene. The shallow subsurface revealed a depositional environment governed by debris flows in between formations of gullies.
- The main sedimentary processes that seem to have contributed to shaping the continental margin of SW Barents Sea over the last ~ 1Ma are debris flows during glaciations (IRD and) meltwater plumes and channel formation during deglaciations.
- Winnowing and associated sand-wave migration is, however, the current governing sedimentary process in the study area (fig 7.11).

.

References

ALF RYSETH, JAN HARALD, AUGUSTSON, MIKE CHARNOCK, OLE HAUGERUD, STIG-MORTEN, KNUTSEN, P. S. M., JAN GUNNAR OPSAL & SUNDSBØ, G. 2003. Cenozoic stratigraphy and evolution of the Sørvestsnaget

Basin, southwestern Barents Sea. *NORWEGIAN JOURNAL OF GEOLOGY,* v. 83**,** 107-130.

ALIOTTA, S. & PERILLO, G. M. E. 1987. A sand wave field in the entrance to Bahia Blanca Estuary, Argentina. *Marine Geology,* 76**,** 1-14.

ALLEN, J. R. L. 1965. Sedimentation to the Lee of Small Underwater Sand Waves: An Experimental Study. *The Journal of Geology,* 73**,** 95-116.

ALLEN, J. R. L. 1980. Sand waves: A model of origin and internal structure. *Sedimentary Geology,* 26**,** 281-328.

ANDREASSEN, K., LABERG, J. S. & VORREN, T. O. 2008. Seafloor geomorphology of the SW Barents Sea and its glaci-dynamic implications. *Geomorphology,* 97**,** 157-177.

ANDREASSEN, K., NILSSEN, L. C. & KUILMAN, B. R. L. 2004. Three-dimensional seismic data from the Barents Sea margin reveal evidence of past ice streams and their dynamics. *Geological Society of America*.

ANDREASSEN, K., ØDEGAARD, C. M. & RAFAELSEN, B. 2007. Imprints of former ice streams, imaged and interpreted using industry three-dimensional seismic data from the south-western Barents Sea. *Geological Society, London, Special Publications,* 277**,** 151-169.

B. RAFAELSEN, K. A., L. W. KUILMAN, E. LEBESBYE, K. HOGSTAD AND M. MIDTBØ 2002. Geomorphology of buried glacigenic horizons in the Barents Sea from three-dimensional seismic data. *Geological Society, London, Special Publications, 2007, 277:253-267,* .

BARINGER, M. O. N. & PRICE, J. F. 1999. A review of the physical oceanography of the Mediterranean outflow. *Marine Geology,* 155**,** 63-82.

BELDERSON, R. H., JOHNSON, M. A. & KENYON, N. H. 1982. Bedforms. *Stride, A. H. (Ed.). Offshore tidal sands — processes and deposits. London: Chapman and Hall,* p. 27-57.

BELLEC, V., WILSON, M., BØE, R., RISE, L., THORSNES, T., BUHL-MORTENSEN, L. & BUHL-MORTENSEN, P. 2008. Bottom currents interpreted from iceberg ploughmarks revealed by multibeam data at Tromsøflaket, Barents Sea. *Marine Geology,* 249**,** 257-270.

BESIO, G., BLONDEAUX, P., BROCCHINI, M. & VITTORI, G. 2004. On the modeling of sand wave migration. *J. Geophys. Res.,* 109**,** C04018.

BESIO, G., P., B., M., B., A.J.M.H., H., D., I., M.A.F., K., A.A., N., P.C., R. & G., V. 2008. The morphodynamics of tidal sand waves: A model overview. *Costal Eng. ,* 55.

BJARNADÓTTIR, L. R., RÜTHER, D. C., WINSBORROW, M. C. M. & ANDREASSEN, K. 2012. Grounding-line dynamics during the last deglaciation of Kveithola, W Barents Sea, as revealed by seabed geomorphology and shallow seismic stratigraphy. *Boreas***,** n/a-n/a.

BONDEVIK, S., BIRKS, H. H., GULLIKSEN, S. & MANGERUD, J. 1999. Late Weichselian Marine 14C Reservoir Ages at the Western Coast of Norway. *Quaternary Research,* 52**,** 104-114.

BUGGE, T. 1983. Submarineslides on the Norwegiancontinental margin, with special emphasis on the Storegga area

Continental Shelf Inst., 110, p.152.

BUHL-MORTENSEN, L., HODNESDAL, H. & THORSNES, T. 2010. Til bunns i Barentshavet. *Book*.

BUTT, F. A., ELVERHØI, A., SOLHEIM, A. & FORSBERG, C. F. 2000. Deciphering Late Cenozoic development of the western Svalbard Margin from ODP Site 986 results. *Marine Geology,* 169**,** 373-390.

BØE, R., BELLEC, V. K., DOLAN, M. F. J., BUHL-MORTENSEN, P., BUHL-MORTENSEN, L., SLAGSTAD, D. & RISE, L. 2009a. Giant sandwaves in the Hola glacial trough off Vesterålen, North Norway. *Marine Geology,* 267**,** 36-54.

BØE, R., BELLEC, V. K., DOLAN, M. F. J., BUHL-MORTENSEN, P., BUHL MORTENSEN, L., SLAGSTAD, D. & RISE, L. 2009b. Giant sandwaves in the Hola glacial trough off Vesterålen, North Norway. *Marine Geology* 267**,** 36-54.

CACCHIONE, D. A. & DRAKE, D. E. 1986. Nepheloid layers and internal waves over continental shelves and slopes. *Geo-Marine Letters,* 6**,** 147-152.

CASTON, V. N. D. 1972. LINAER SAND BANKS IN THE SOUTHERN NORTH SEA. *Sedimentology,* 18**,** 63-78.

CLOET, R. L. 1963. *Hydrographic analysis of the sandbanks in the approaches to Lowestoft Harbour,* London.

DAMUTH, J. E. 1980. Use of high-frequency (3.5–12 kHz) echograms in the study of near-bottom sedimentation processes in the deep-sea: A review. *Marine Geology,* 38**,** 51-75.

DERYABIN, A. 2012. Relationship between glacial erosion and fluid flow inferred from 3D seismic data : SW Barents Sea *Master thesis*.

DINGLE, R. V. 1965. Sand waves in the North Sea mapped by continuous reflection profiling. *Marine Geology,* 3**,** 391-400.

EIDVIN, T., JANSEN, E., RUNDBERG, Y., BREKKE, H. & GROGAN, P. 2000. The upper Cainozoic of the Norwegian continental shelf correlated with the deep sea record of the Norwegian Sea and the North Atlantic. *Marine and Petroleum Geology,* 17**,** 579-600.

EYLES, N., EYLES, C. H. & MIALL, A. D. 1983. Lithofacies types and vertical profile models; an alternative approach to the description and environmental interpretation of glacial diamict and diamictite sequences. *Sedimentology,* 30**,** 393-410.

FALEIDE, J. I., SOLHEIM, A., FIEDLER, A., HJELSTUEN, B. O., ANDERSEN, E. S. & VANNESTE, K. 1996. Late Cenozoic evolution of the western Barents Sea-Svalbard continental margin. *Global and Planetary Change,* 12**,** 53-74.

FAUGÈRES, J.-C., STOW, D. A. V., IMBERT, P. & VIANA, A. 1999. Seismic features diagnostic of contourite drifts. *Marine Geology,* 162**,** 1-38.

FIELD, M. E., NELSON, C. H., CACCHIONE, D. A. & DRAKE, D. E. 1981. Sand waves on an epicontinental shelf: Northern Bering Sea. *Marine Geology,* 42**,** 233-258.

FJALSTAD, A. & MØLLER, J. J. 1994. Submerged and tilted coastal features off Troms, Northern Norway: a comment. *Nor. Geol. Tidsskrift,* 74**,** 241–244.

FLOOD, R. D. & SHOR, A. N. 1988. Mud waves in the Argentine Basin and their relationship to regional bottom circulation patterns. *Deep Sea Research Part A. Oceanographic Research Papers,* 35**,** 943-971.

GIBSON, W. M. 1951. Sandwaves in San Francisco Bay. *Coast Geod. Surv. J.,* 51 pp. 54–58.

GÓMEZ, E. A., CUADRADO, D. G. & PIERINI, J. O. 2010. Sand transport on an estuarine submarine dune field. *Geomorphology,* 121**,** 257-265.

HABGOOD, E. L., KENYON, N. H., MASSON, D. G., AKHMETZHANOV, A., WEAVER, P. P. E., GARDNER, J. & MULDER, T. 2003. Deep-water sediment wave fields, bottom current sand channels and and gravity flow channel-lobe systems: Gulf of Cadiz, NE Atlantic. *Sedimentology,* 50.

HARVEY, J. G. 1966. Large sand waves in the Irish Sea. *Marine Geology,* 4**,** 49-55.

HOUBOLT, J. J. H. C. 1968. Recent sediments in the southern bight of the North Sea. *Geol. Mijnbouw,* 47**,** 245-273.

HULSCHER, S. J. M. H. 1996. Tidal-induced large-scale regular bed form patterns in a three-dimensional shallow water model. *Journal of Geophysical Research. Pt. C: Oceans,* 101**,** 20,727-20,744.

HULSCHER, S. J. M. H. & A BRINK VAN DEN, G. M. 2001. Comparison between predicted and observed sand waves and sand banks in the North Sea. *Journal of Geophysical Research. Pt. C: Oceans,* 106.

JARRETT, J. 1976. Tidal prism-inlet area relationships. *Book*.

KARL, H. A. C., D. A.CARLSON, P. R. 1986. Internal-wave currents as a mechanism to account for large sand waves in navarinsky canyon head, Bearing Sea. *U.S. Geological Survey*.

KENYON, N. H. 1970. Sand ribbons of European tidal seas. *Marine Geology,* 9**,** 25-39.

KENYON, N. H. 1986. Evidence from bedforms for a strong poleward current along the upper continental slope of northwest Europe. *Marine Geology,* 72**,** 187-198.

KENYON, N. H., AKHMETZHANOV, A. M. & TWICHELL, D. C. 2002. Sand wave fields beneath the Loop Current, Gulf of Mexico: reworking of fan sands. *Marine Geology,* 192**,** 297-307.

KENYON, N. H. & STRIDE, A. E. 1968. The Crest Length and Sinuosity of Some Marine Sand Waves: NOTES. *Journal of Sedimentary Petrology,* 38**,** 255-259.

KING, E. L., BØE, R., BELLEC, V. K., RISE, L. & DOLAN, M. not publ. Contour current driven sandwaves on the upper slope of the continental margin offshore northern Norway - setting and morphometrics. *Report*.

KNAAPEN, M. A. F. 2005. Sandwave migration predictor based on shape information. *J. Geophys. Res.,* 110**,** F04S11.

KNIES, J., MATTHIESSEN, J., VOGT, C., LABERG, J. S., HJELSTUEN, B. O., SMELROR, M., LARSEN, E., ANDREASSEN, K., EIDVIN, T. & VORREN, T. O. 2009. The Plio-Pleistocene glaciation of the Barents Sea–Svalbard region: a new model based on revised chronostratigraphy. *Quaternary Science Reviews,* 28**,** 812-829.

LABERG, J. S. & VORREN, T. O. 1995. Late Weichselian submarine debris flow deposits on the Bear Island Trough Mouth Fan. *Marine Geology,* 127**,** 45-72.

LABERG, J. S. & VORREN, T. O. 1996. The Middle and Late Pleistocence evolution and the Bear Island Trough Mouth Fan. *Global and Planetary Change,* 12**,** 309-330.

LARSEN, E., KJÆR, K. H., DEMIDOV, I. N., FUNDER, S., GRØSFJELD, K., HOUMARK-NIELSEN, M., JENSEN, M., LINGE, H. & LYSA, A. 2006. Late Pleistocene glacial and lake history of northwestern Russia. *Boreas,* 35**,** 394-424.

LUCCHI, R. G., REBESCO, M., CAMERLENGHI, A., BUSETTI, M., TOMADIN, L., VILLA, G., PERSICO, D., MORIGI, C., BONCI, M. C. & GIORGETTI, G. 2002. Mid-late Pleistocene glacimarine sedimentary processes of a high-latitude, deep-sea sediment drift (Antarctic Peninsula Pacific margin). *Marine Geology,* 189**,** 343-370.

MACKENSEN, A. & HALD, M. 1988. Cassidulina teretis Tappan and C. laevigata d'Orbigny: their modern and late Quaternary distribution in northern seas. *Journal of Foraminiferal Research,* 18**,** 16-24.

MASSON, D. G. 2001. Sedimentary processes shaping the eastern slope of the Faeroe–Shetland Channel. *Continental Shelf Research,* 21**,** 825-857.

MASSON, D. G., HOWE, J. A. & STOKER, M. S. 2002. Bottom-current sediment waves, sediment drifts and contourites in the northern Rockall Trough. *Marine Geology,* 192**,** 215-237.

MCCAVE, I. N. 1971. Sand waves in the North Sea off the coast of Holland. *Marine Geology,* 10**,** 199-225.

MIGEON, S., SAVOYE, B. & FAUGERES, J. C. 2000. Quaternary development of migrating sediment waves in the Var deep-sea fan: distribution, growth pattern, and implication for levee evolution. *Sedimentary Geology,* 133**,** 265-293.

MORELISSEN, R., HULSCHER, S. J. M. H., KNAAPEN, M. A. F., NÉMETH, A. A. & BIJKER, R. 2003. Mathematical modelling of sand wave migration and the interaction with pipelines. *Coastal Engineering,* 48**,** 197-209.

MØLLER, J. J. 2000. Submerged littoral sediments, beach ridges and wave-cut platforms off Troms, North Norway: Revisiting old questions. *Norsk Geologisk Tidsskrift,* 80**,** 203-212.

NEMETH, A. A. 2003. *Modelling offshore sand waves.*

NÉMETH, A. A., HULSCHER, S. J. M. H. & DE VRIEND, H. J. 2002. Modelling sand wave migration in shallow shelf seas. *Continental Shelf Research,* 22**,** 2795-2806.

NORMARK, W. R., PIPER, D. J. W., POSAMENTIER, H., PIRMEZ, C. & MIGEON, S. 2002. Variability in form and growth of sediment waves on turbidite channel levees. *Marine Geology,* 192**,** 23-58.

PEDROSA, M. T., CAMERLENGHI, A., DE MOL, B., URGELES, R., REBESCO, M. & LUCCHI, R. G. 2011. Seabed morphology and shallow sedimentary structure of the Storfjorden and Kveithola trough-mouth fans (North West Barents Sea). *Marine Geology,* 286**,** 65-81.

PETERSEN, C. J., BÜNZ, S., HUSTOFT, S., MIENERT, J. & KLAESCHEN, D. 2010. High-resolution P-Cable 3D seismic imaging of gas chimney structures in gas hydrated sediments of an Arctic sediment drift. *Marine and Petroleum Geology,* 27**,** 1981-1994.

PINET, P. 2009. *Invitation to Oceanography*, Jones & Bartlett Learning.

REEDER, D. B., MA, B. B. & YANG, Y. J. 2011. Very large subaqueous sand dunes on the upper continental slope in the South China Sea generated by episodic, shoaling deep-water internal solitary waves. *Marine Geology,* 279**,** 12-18.

RISE, L., OTTESEN, D., BERG, K. & LUNDIN, E. 2005. Large-scale development of the mid-Norwegian margin during the last 3 million years. *Marine and Petroleum Geology,* 22**,** 33-44.

ROKOENGEN, K. & DEKKO, T. 1993. Submerged and tilted coastal features off Troms, northern Norway. *Nor. Geol. Tidsskrift,* 73**,** 198–208.

RUMOHR, J., BLAUME, F., ERLENKEUSER, H., FOHRMANN, H., HOLLENDER, F. J., MIENERT, J. & SCHÄFER-NETH, C. 2001. Records and Processes of Near-Bottom Sediment Transport along the Norwegian-Greenland Sea Margins during Holocene and Late Weichselian (Termination I) Times

books.google.com.

SEJRUP, H. P., HJELSTUEN, B. O., TORBJØRN DAHLGREN, K. I., HAFLIDASON, H., KUIJPERS, A., NYGÅRD, A., PRAEG, D., STOKER, M. S. & VORREN, T. O. 2005. Pleistocene glacial history of the NW European continental margin. *Marine and Petroleum Geology,* 22**,** 1111-1129.

SKAGSETH, Ø. pers.com. *Institute of Marine Research*.

SKARDHAMAR, J. pers.com. *Institute of marine research*.

ŚLUBOWSKA-WOLDENGEN, M., RASMUSSEN, T. L., KOÇ, N., KLITGAARD-KRISTENSEN, D., NILSEN, F. & SOLHEIM, A. 2007. Advection of Atlantic Water to the western and northern Svalbard shelf since 17,500 cal yr BP. *Quaternary Science Reviews,* 26**,** 463-478.

STERILINI, F., HULSCHER, S. J. M. H. & HANES, D. M. 2009. Simulating and understanding sand wave variation: A case study of the Golden Gate sand waves. *Journal of Geophysical Research,* 114.

STOW, D. A. V., HUNTER, S., WILKINSON, D. & HERNÁNDEZ-MOLINA, F. J. 2008. Chapter 9 The Nature of Contourite Deposition. *In:* REBESCO, M. & CAMERLENGHI, A. (eds.) *Developments in Sedimentology.* Elsevier.

STOW, D. A. V. & MAYALL, M. 2000. Deep-water sedimentary systems: New models for the 21st century. *Marine and Petroleum Geology,* 17**,** 125-135.

STRIDE & STRIDE 1982. Offshore tidal Sands Processes and Depositis. *Chapman and Hall***,** 8.

SVENDSEN, J. I., GATAULLIN, V., MANGERUD, J. & POLYAK, L. 2004. The glacial History of the Barents and Kara Sea Region. *In:* EHLERS, J. & GIBBARD, P. L. (eds.) *Developments in Quaternary Sciences.* Elsevier.

SÆTTEM, J., BUGGE, T., FANAVOLL, S., GOLL, R. M., MØRK, A., MØRK, M. B. E., SMELROR, M. & VERDENIUS, J. G. 1994. Cenozoic margin development and erosion of the Barents Sea: Core evidence from southwest of Bjørnøya. *Marine Geology,* 118**,** 257-281.

SÆTTEM, J., POOLE, D. A. R., ELLINGSEN, L. & SEJRUP, H. P. 1992. Glacial geology of outer Bjørnøyrenna, southwestern Barents Sea. *Marine Geology,* 103**,** 15-51.

SÆTTEM, J., POOLE, D. A. R., SEJRUP, H. P. & ELLINGSEN, K. L. 1991. Glacial geology of outer Bjørnøyrenna, western Barents Sea : preliminary results. *Norsk geologisk tidsskrift*

TWICHELL, D. C. & ROBERTS, D. G. 1982. Morphology, distribution, and development of submarine canyons on the United States Atlantic continental slope between Hudson arid Baltimore Canyons. *Geology,* 10**,** 408-412.

VAN DIJK, T. A. G. P., LINDENBERGH, R. C. & EGBERTS, P. J. P. 2008. Separating bathymetric data representing multiscale rhythmic bed forms: A geostatistical and spectral method compared. *J. Geophys. Res.,* 113**,** F04017.

VAN LANDEGHEM, K. J. J., BAAS, J. H., MITCHELL, N. C., WILCOCKSON, D. & WHEELER, A. J. 2012. Reversed sediment wave migration in the Irish Sea, NW Europe: A reappraisal of the validity of geometry-based predictive modelling and assumptions. *Marine Geology,* 295–298**,** 95-112.

VAN OYEN, T. & BLONDEAUX, P. 2009. Grain sorting effects on the formation of tidal sand waves. *Journal of Fluid Mechanics,* 629**,** 311-342.

VANVEEN, J. 1938. Die unterseeische Sandwüste in der Nordsee Geol. Meere Binnengewässer.

VON LOM-KEIL, H., SPIEß, V. & HOPFAUF, V. 2002. Fine-grained sediment waves on the western flank of the Zapiola Drift, Argentine Basin: evidence for variations in Late Quaternary bottom flow activity. *Marine Geology,* 192**,** 239-258.

VORREN, T. O. 2003. Subaquatic landsystems: continental margins. *London, Arnold Publishers***,** 289–312.

VORREN, T. O., HALD, M. & LEBESBYE, E. 1988. Late Cenozoic Environments in the Barents Sea. *Paleoceanography,* 3**,** 601-612.

VORREN, T. O. & LABERG, J. S. 1997. Trough mouth fans — palaeoclimate and ice-sheet monitors. *Quaternary Science Reviews,* 16**,** 865-881.

VORREN, T. O., LANDVIK, J. Y., ANDREASSEN, K. & LABERG, J. S. 2011. Chapter 27 - Glacial History of the Barents Sea Region. *In:* JÜRGEN EHLERS, P. L. G. & PHILIP, D. H. (eds.) *Developments in Quaternary Sciences.* Elsevier.

VORREN, T. O., LEBESBYE, E., ANDREASSEN, K. & LARSEN, K. B. 1989. Glacigenic sediments on a passive continental margin as exemplified by the Barents Sea. *Marine Geology,* 85**,** 251-272.

VORREN, T. O., RICHARDSEN, G., KNUTSEN, S.-M. & HENRIKSEN, E. 1991. Cenozoic erosion and sedimentation in the western Barents Sea. *Marine and Petroleum Geology,* 8**,** 317-340.

VORREN, T. O., STRASS, I. F. & LIND-HANSEN, O. W. 1978. Late Quaternary sediments and stratigraphy on the continental shelf off Troms and west Finnmark, northern Norway. *Quaternary Research,* 10**,** 340-365.

WINSBORROW, M. C. M., ANDREASSEN, K., CORNER, G. D. & LABERG, J. S. 2010. Deglaciation of a marine-based ice sheet: Late Weichselian palaeo-ice dynamics and retreat in the southern Barents Sea reconstructed from onshore and offshore glacial geomorphology. *Quaternary Science Reviews,* 29**,** 424-442.

WYNN, R. B., MASSON, D. G. & BETT, B. J. 2002. Hydrodynamic significance of variable ripple morphology across deep-water barchan dunes in the Faroe–Shetland Channel. *Marine Geology,* 192**,** 309-319.

YOON, S. H., CHOUGH, S. K., THIEDE, J. & WERNER, F. 1991. Late Pleistocene sedimentation on the Norwegian continental slope between 67° and 71°N. *Marine Geology,* 99**,** 187-207.


UNIVERSITY
OF TROMSØ